Modeling of wind turbine noise sources and propagation in the atmosphere

Yuan Tian

▶ To cite this version:

HAL Id: tel-01335869

https://theses.hal.science/tel-01335869v2

Submitted on 25 Aug 2016

THESE DE DOCTORAT
DE
L'Université Paris-Saclay
PRÉPARÉE À
ENSTA ParisTech

ECOLE DOCTORALE N°579
Sciences mécaniques et énergétiques, matériaux et géosciences (SMEMaG)

Spécialité de doctorat : Acoustique

Par

Mme Yuan Tian

Modeling of wind turbine noise sources and propagation in the atmosphere

Thèse présentée et soutenue à Palaiseau, le 15 février 2016 :

Composition du Jury :

Mr François Coulouvrat	Directeur de recherche, CNRS	Président
Mr Michel Roger	Professeur, Ecole Centrale de Lyon	Rapporteur
Mr Wen Zhong Shen	Professeur, Technical University of Denmark	Rapporteur
Mme Irène Laure	Ingénieur, EDF Energies Nouvelles	Examinatrice
Mr Olivier Cadot	Professeur, ENSTA ParisTech	Directeur de thèse
Mr Benjamin Cotté	Maître de conférence, ENSTA ParisTech	Co-directeur de thèse

Acknowledgments

Abstract: The purpose of this work is to model wind turbine noise sources and propagation in the atmosphere in order to better understand the characteristics of wind turbine noise at long range and to help wind turbine manufacturers and wind farm developers meet the noise regulations. By coupling physically-based aeroacoustic source and propagation models, we are able to predict wind turbine noise spectra, directivity and amplitude modulation in various atmospheric conditions.

Broadband noise generated aerodynamically, namely turbulent inflow noise, trailing edge noise and separation/stall noise, is generally dominant for a modern wind turbine. Amiet's analytical model is chosen to predict turbulent inflow noise and trailing edge noise, considering several improvements to the original theory: 1, an empirical leading edge thickness correction is introduced in the turbulent inflow noise calculation; 2, a wall pressure fluctuation spectrum model proposed recently for adverse pressure gradient flow is used in the trailing edge noise predictions. The two models are validated against several wind tunnel experiments from the literature using fixed airfoils.

Amiet's model is then applied on a full-size wind turbine to predict the noise emission level in the near field. Doppler effect and blade rotation are taken into account. Cases with constant wind profiles and no turbulence are used first, then wind shear and atmospheric turbulence effects obtained from Monin-Obukhov similarity theory are included. Good agreements against field measurements are found when both turbulent inflow noise and trailing edge noise are considered. Classical features of wind turbine noise, such as directivity and amplitude modulation, are recovered by the calculations. Comparisons with a semi-empirical model show that separation noise might be significant in some circumstances.

Next, Amiet's theory is coupled with propagation models to estimate noise immission level in the far-field. An analytical model for the propagation over an impedance ground in homogeneous conditions is studied first. The ground effect is shown to modify the shape of the noise spectra, and to enhance the amplitude modulation in some third octave bands. A method to couple the source model to a parabolic equation code is also proposed and validated to take into account atmospheric refraction effects. Depending on the propagation direction, noise levels vary because the ground effect is influenced by wind shear and a shadow zone is present upwind. Finally, the point source assumption is reviewed considering both the analytical and numerical propagation models.

Résumé: L'objectif de ce travail est de modéliser les sources et la propagation atmosphérique du bruit généré par les éoliennes afin de mieux comprendre les caractéristiques de ce bruit à grande distance et d'aider les fabricants d'éoliennes et les développeurs de parc à respecter la réglementation. En couplant des modèles physiques de source aéroacoustique et de propagation, nous sommes capables de prédire les spectres de bruit, ainsi que la directivité et les modulations d'amplitude associées, pour différentes conditions atmosphériques.

Le bruit aérodynamique large bande, à savoir le bruit d'impact de turbulence, le bruit de bord de fuite et le bruit de décrochage, est généralement dominant pour les éoliennes modernes. Le modèle analytique d'Amiet est choisi pour prédire le bruit d'impact de turbulence et le bruit de bord de fuite, en considérant plusieurs améliorations par rapport à la thèorie initial : 1, une correction empirique pour l'épaisseur du bord d'attaque est introduite dans le calcul du bruit d'impact de turbulence ; 2, un modèle spectral des fluctuations de pression pariétale proposé récemment pour un écoulement avec gradient de pression défavorable est utilisé dans le calcul du bruit de bord de fuite. Ces modèles sont validés par comparaison avec des mesures de la littérature en soufflerie avec des profils fixes.

Le modèle d'Amiet est ensuite appliqué à une éolienne complète pour prédire le bruit émis en champ proche. L'effet de la rotation des pales et l'effet Doppler sont pris en compte. On utilise d'abord des profils de vent constant sans turbulence, puis l'effet du cisaillement du vent et de la turbulence atmosphérique sont inclus à l'aide de la théorie de la similitude de Monin-Obukhov. De bons accords sont obtenus avec des mesures sur site éolien lorsque l'on considère à la fois les bruits de bord de fuite et d'impact de turbulence. On retrouve à l'aide du modèle les caractéristiques classiques du bruit des éoliennes, comme la directivité et les modulations d'amplitude. Des comparaisons avec un modèle semi-empirique montrent que le bruit de décrochage peut être significatif dans certains conditions.

L'étape suivante consiste à coupler la thèorie d'Amiet avec des modèles de propagation pour estimer le bruit à un récepteur en champ lointain. On étudie dans un premier temps un modèle analytique de propagation en conditions homogènes au-dessus d'un sol d'impédance finie. On montre que l'effet de sol modifie la forme des spectres de bruit, et augmente les modulations d'amplitude dans certains tiers d'octave. Dans un second temps, une méthode pour coupler le modèle de source à un code d'équation parabolique est proposée et validée pour prendre en compte les effets de réfraction atmosphérique. En fonction de la direction de propagation, les niveaux de bruit varient car l'effet de sol est influencé par les gradients de vent et car une zone d'ombre est présente dans la direction opposée au vent. On discute pour finir l'approximation de source ponctuelle à l'aide des modèles de propagation analytique et numérique.

Contents

List of Figures

List of Tables

List of Symbols

Symbol	Unit	Description
a, a'	–	axial and tangential induction factor in BEM theory
b	m	Half chord
b_c	–	Non-dimensional coefficient for Corcos model
c	m	Chord
c_0	m/s	Sound speed
e	m	Airfoil maximum thickness
f	Hz	Acoustic frequency
k	m^{-1}	Acoustic wave number
l	Pa	Surface lift force fluctuation
l_y	m	Span-wise turbulence correlation length
p	Pa	Pressure fluctuation
p_c	Pa	3D complex pressure
$q_c = p_c\sqrt{r}$		2D complex pressure
u_*	m/s	Friction velocity
u', v', w'	m/s	Turbulence velocity fluctuation
w, w_0	m/s	Incoming turbulence gust and its amplitude
z_0	m	Surface roughness
C_l, C_d, C_f	–	Lift, drag, skin friction coefficient
C_n, C_t	–	Axial and tangential force coefficient
C_p	$J/Kg \cdot K$	Specific heat of dry air
E^*	–	Fresnel integral
H	W/m^2	Heat flux
K_c	m^{-1}	Convective wave number
$\bar{K}_c$	–	Normalized convective wave number
$K\ (K_x, K_y)$	m^{-1}	Turbulence wave number
K_e	m^{-1}	Wave number corresponding to the turbulence integral length scale
$\bar{K}_x, \bar{K}_y$	–	Normalized turbulence wave number
L	m	Span
L_{outer}	m	Turbulence outer length scale
ΔL	dB	Relative sound pressure level
$\mathscr{L}$	–	Airfoil transfer function
M	–	Mach number
P	–	Amplitude of pressure fluctuation
Q	–	Spherical wave reflection coefficient

R	m	Horizontal distance from observer to the wind turbine
R_s	m	Modified distance between retarded source and observer
R_d	m	Length of direct path of sound wave
R_r	m	Length of reflected path of sound wave
R_p	$-$	Plane wave reflection coefficient
$\vec{R}(R_1, R_2, R_3)$	m	Source-observer vector in current time
$\vec{R}_t$	m	Source-observer vector in retarded time
R_T	$-$	Ratio of outer to inner time scale of boundary layer
S_0	m	Modified distance between observer and the origin
S_{ll}	dB/Hz	Power spectrum density of surface lift force
S_{pp}	dB/Hz	Power spectrum density of far field sound pressure level
T_*	K	Temperature scale
U	m/s	Free stream velocity / Wind speed
U_c	m/s	Convective velocity
U_e	m/s	External velocity of boundary layer
Z		Normalized ground impedance
β	rad	Wind Turbine blade position (wing angle)
$\beta_0 = \sqrt{1 - M^2}$	$-$	Compressibility factor
β_c	$-$	Clauser parameter for wall pressure fluctuation model
δ_*	m	Boundary layer displacement thickness
δ	m	Boundary layer thickness
θ	rad	Sound wave reflection angle
θ^*	m	Boundary layer momentum thickness
ω	rad/s	Acoustic angular frequency
$\tilde{\omega} = \omega\delta^*/U_e$	$-$	Reduced frequency
ω_e	rad/s	Emission frequency
κ	$-$	Von Kármán constant
$\bar{\kappa} = \bar{\mu} - \bar{K}_y^2/\beta_0^2$	$-$	Non-dimensional parameter in Amiet's model
$\bar{\mu} = \bar{K}_x M/\beta_0^2$	$-$	Non-dimensional parameter in Amiet's model
μ	Ns/m^2	Air dynamic viscosity
ν	m^2/s	Air kinematic viscosity
ρ_0	kg/m^3	Air density
σ_e	$kPa \cdot s \cdot m^{-2}$	effective flow resistivity
σ_u	m/s	Root-mean-square of turbulent velocity fluctuation

τ_w	Pa/m^2	Wall shear stress
ϕ	$-$	Velocity potential field
ϕ_{pp}	dB/Hz	Spectral of wall pressure fluctuation
ϕ_{ww}	dB/Hz	2 dimensional turbulence spectrum
$\chi = U_c/U$	$-$	Convective velocity coefficient
Δ	$-$	ratio between boundary layer thickness and displacement thickness
Λ	m	Turbulence integral length scale
Π	$-$	Wake strength parameter for wall pressure fluctuation model
Φ	$-$	Non-dimensional velocity potential field
Φ_0	$-$	Wave number spectrum of incident gust amplitude
(x, y, z), (y_1, y_2, y_3)	$-$	Source coordinate
$(\bar{x}, \bar{y}, \bar{z})$	$-$	Normalized source coordinate
(y_1', y_2', y_3')	$-$	Source coordinate at current time
(x_1, x_2, x_3)	$-$	Receiver coordinate
AM		Amplitude modulation
AoA		Angle of attack
APG		Adverse pressure gradient
BEM		Blade element momentum theory
FPG		Favoriate pressure gradient
MOST		Monin-Obukhov similarity thoery
OASPL		Overall sound pressure level
SPL		Sound pressure level
SWL		Sound power level
TEN		Trailing edge noise
TIN		Turbulent inflow noise
ZPG		Zero pressure gradient

Introduction

Contents

1.1 Wind turbine noise in general

1.1.1 Wind energy and wind farm development

Wind energy can be extracted from airflow by a wind turbine, and then converted into electrical power with satisfying efficiency. The number of wind farms, given the fact that it is a clean and renewable energy, grows very fast in many countries, in order to reduce the reliance on traditional energy sources. The size of wind turbine also grows, from less than 1 MW capacity in 1985, to 7.5 MW nowadays. At the end of 2014, the accumulated total installed wind power capacity was 128.8 GW in the EU, with approximately 120 GW onshore [20]. And the European Wind Energy Association estimates that by end of 2020, the total installed capacity will increases by 64% to 192.5 GW in Europe [21]. France has a total installed capacity of over 9285 MW at the end of 2014, and wind energy accounts for 3.4% of the total electricity production [22].

1.1.2 Wind turbine noise regulations

The noise generated by a wind turbine or a wind farm has been complained frequently by the people living in the neighborhood. There are regulations regarding the emission levels, corresponding to the sound power level (SWL) radiated by the wind turbine, and the immission levels, corresponding to the sound pressure level (SPL) at a neighbors' houses. There is an international standard for emission level measurements called IEC 61400-11, that uses a microphone on a rigid platform. On the other hands, there is no international standard for immission level measurements. In France, the noise limitation depends on the background noise level. The wind farm is not allowed to increase the ambient noise more than $5\,dB$ at daytime, and $3\,dB$ at night, measured by $L_A eq$, the equivalent sound level [23, 24]. In some other countries, absolute limits or combination of absolute and relative limits are applied [25]. For example, in Denmark, the limits are typically $42\,dBA$ at $6\,m/s$ reference wind speed, and $44\,dBA$ at $8\,m/s$ reference wind speed; in UK, the sound pressure level from a wind farm cannot exceed $43\,dBA$ or $5\,dBA$ above the background noise level at night. These regulations imply that an accurate noise prediction model as well as a correct background noise measurement are essential for the approval of new wind farm projects, especially near populated areas.

1.1.3 Wind turbine noise mechanisms

Wind turbines generate mainly two types of noise: aerodynamic noise and mechanical noise. The later comes from the turbine's internal gears rotating against each other [26], and it is more noticeable for small size wind turbines. Advanced techniques help to confine the mechanical noise inside the nacelle or tower [5, 26], thus for a modern large scale wind turbines, the noise is mostly generated due to aerodynamic interaction between the airflow and the turbine blades.

Aerodynamics noise can be categorized into two types: airfoil self noise, and turbulent inflow noise [1, 7, 3]. Self noise is caused by interaction of the turbulence produced in the airfoil boundary layer and wake with the airfoil itself, while turbulent inflow noise is caused by the atmospheric turbulence encountering the airfoil leading edge. Airfoil self noise consists of several mechanisms: trailing edge noise, separation noise, trailing edge bluntness noise and tip vortex noise, as seen in Figure 1.1. Trailing edge noise is due to the turbulence inside the boundary layer that is scattered at the trailing edge. Separation noise is generated when the angle of attack is large, and the flow separates near trailing edge of the suction side. The separation region then moves upstream while there are vortex appearing and growing, and then finally shedding off. If the stall angle is reached, the flow separation is violent and deep stall noise is generated [1]. A blunt trailing edge causes vortex shedding, which causes a narrowband radiation called trailing edge bluntness noise. Tip vortex noise has a similar mechanism, it is caused by the vortex shedding near the tip of a blade. For a modern megawatt-sized wind turbine,

total noise is usually dominated by trailing edge noise [3]. Oerlemans *et al.* [2] have shown using microphone array measurements that for an observer close to the turbine on the ground, most of the noise is produced by the outer part of the blades during the downward part of the revolution, as seen in Figure 1.2. Turbulent inflow noise might become dominant depending on atmospheric turbulence conditions.
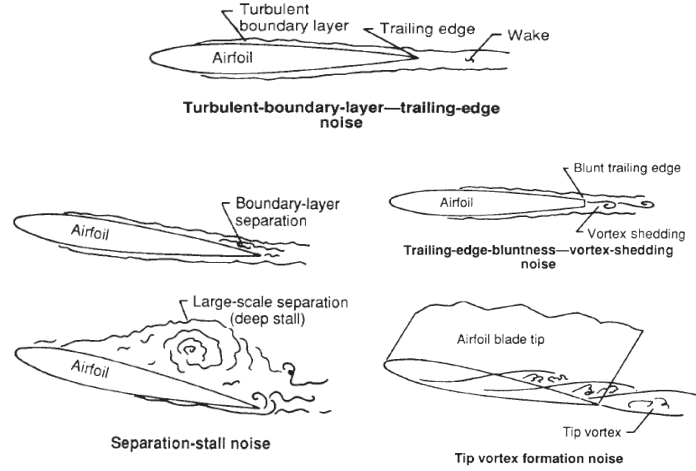
Figure 1.1: Airfoil self noise: trailing edge noise, separation noise, trailing edge bluntness noise, tip vortex noise [1].

Figure 1.2: Noise source distribution in the rotor plane of a modern large wind turbine, measured about one rotor diameter upwind from the turbine. Taken from [2].

1.1.4 Spectrum, directivity and amplitude modulation

Wind turbine noise spectrum is broadband, as can be seen in the measurements shown in Figure 1.3 for a 2.3 MW wind turbine. When plotted in dBA, the peak of the spectrum is around 500 Hz. Moller and Pedersen have estimated the sound power level spectrum emitted by larger wind turbines based on a large set of measurements [4]. Figure 1.4 shows that the spectrum level increases with increasing wind turbine size, especially at low frequency. Wind turbine noise is also directional, see Figure 1.5. The directivity feature of a wind turbine is caused by the dipole nature of the wind turbine noise source. Measurements and predictions show that the sound pressure level (SPL) of wind turbine noise is stronger in the wind direction than in the crosswind wind direction.

The most annoying feature of wind turbine noise is believed to be the amplitude modulation (AM) [3, 6]. It is a phenomenon related to the blade rotation, and caused by the Doppler effect and the fact that the relative source and observer locations are varying during the rotation. Predictions of this AM show that in the crosswind direction, the AM strength reaches maximum, up to few dBs; while the minimum is reached in the wind direction [27]. This phenomenon becomes weaker if the observer is further from the wind turbine. However, in a recent report by Renewable UK [6], there are measurements showing that even at long distance, strong AM can be recorded in the downwind direction. In the same report, they define the former amplitude modulation as 'normal amplitude modulation', the later as 'enhanced amplitude modulation', and suggest that there might be two different mechanisms that cause these two different types of amplitude modulation. A measured time history of sound pressure level seen in Figure 1.6 shows the phenomenon of enhanced amplitude modulation for an upwind receiver. For normal amplitude modulation, the mechanism is directivity and Doppler effect; for enhanced amplitude modulation, there are many assumptions raised by different researchers. A common point of view is that it is caused by the strong wind shear and the change of AoA at leading edge of the blades during rotation. However, up to date, there is no complete and convincing theory to explain this type of amplitude modulation.

1.1.5 Low frequency component, infrasound, annoyance of wind turbine noise and health effects

Wind turbine noise contains low frequency and infrasound components, as already seen in Figure 1.4. There are often arguments about the fact low frequency noise and infrasound may cause health effect in terms of 'wind turbine syndrome'. Moller and Pedersen [4] compared the indoor SPL and the hearing threshold at low frequencies, see Figure 1.7. We observe that low frequency components of wind turbine noise can be heard down to 40 Hz in some configurations. A
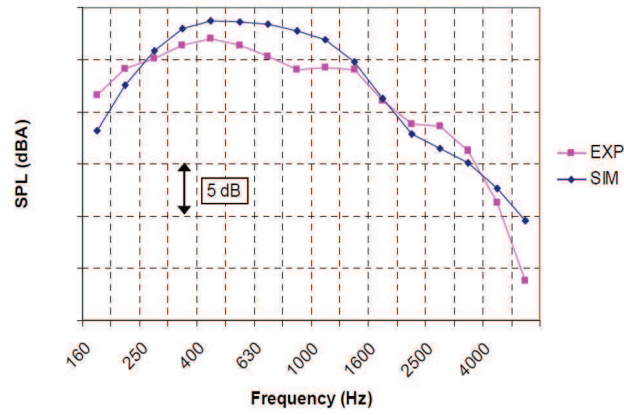
Figure 1.3: Measured and predicted SPL for a 2.3 MW wind turbine at 240 m. Taken from [3].
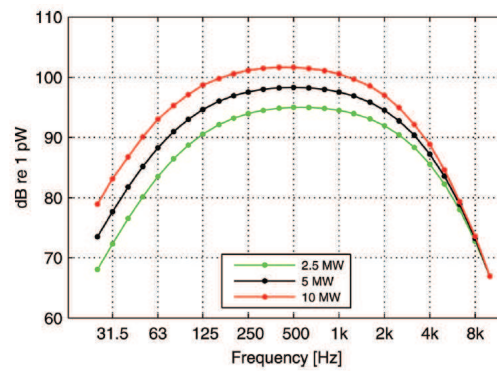
Figure 1.4: Estimated A-weighted sound power level spectrum. Taken from [4].
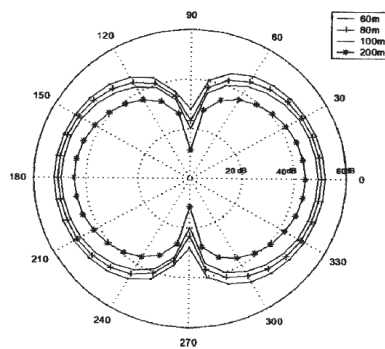
Figure 1.5: Predicted wind turbine noise directivity. Wind is coming from left to right. Taken from [5].
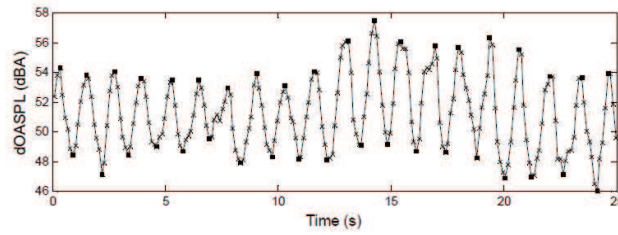
Figure 1.6: Time history of A-weighted overall sound pressure level measured 50 m upwind from a 93-m diameter wind turbine. Taken from [6].

listening test by Lee *et al.* [28] indicate that the equivalent sound level and the amplitude modulation both significantly contribute to noise annoyance. Since wind turbine noise is usually quantified with A-weighted values, this causes a tendency of underestimating the low frequency components. Some research groups have proposed other noise level indicators for assessment of this low frequency noise [29, 30].

There are arguments about infrasound perception in the literature. A review by Salt and Hullar [31] concludes that although infrasound cannot be perceived by human ears, it does have an influence on the inner ear. However, many experimental studies show that most people don't perceive those infrasound and do not suffer from any health defects [32, 33, 34].

1.1.6   Propagation effects

Wind turbines always operate in an environment where many factors play roles on the noise generation and propagation, for example, atmospheric conditions (turbulence, wind shear and direction, temperature, etc), terrain type, obstacles near wind turbines such as houses, forests, see Figure 1.8. Acoustic refraction is an important atmospheric effect related to the variation of temperature and wind speed with height. This effect varies with propagation directions with respect to the wind direction. As can be seen in Figure 1.9, upwind propagating sound waves will be refracted upwards, which creates a shadow zone close to the ground at a certain distance from the wind turbine. Meanwhile, downwind propagating sound waves will be refracted downwards, and may lead to a reinforcement of noise immission. Some studies have shown that wind turbine noise is often stronger at night [9]. This can be attributed to the strong wind shear occurring in stable atmospheric conditions that are typical at night. Figure 1.10 shows the increase of wind speed with height is much larger in stable conditions than in unstable/neutral conditions. There is also energy lost during the propagation due to the atmospheric absorption.

Ground will reflect sound wave, and sound reflection depends on the terrain
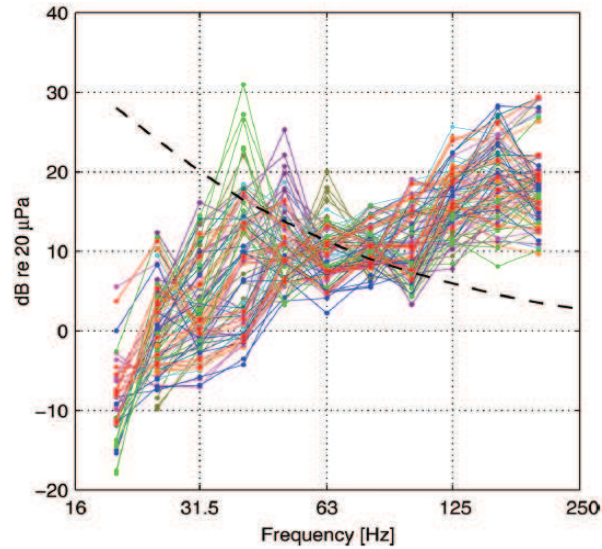
Figure 1.7: Indoor A-weigthed SPL for 81 turbine/room combinations where the outdoor SPL is 44 dBA. Dashed line is the hearing threshold according to ISO 389-7. Taken from [4].
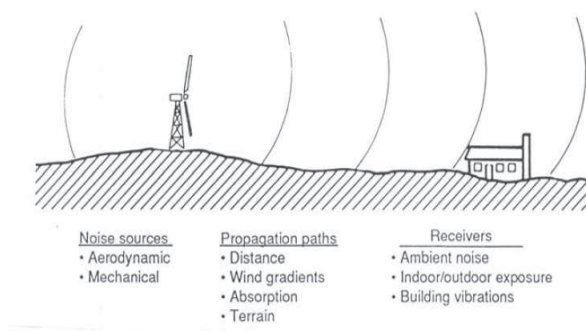
Figure 1.8: Illustration of wind turbine noise generation and propagation. Taken from [7]

shape, roughness, ground impedance [35]. A wind turbine is an extended acoustic source, which has an influence on the ground effect. Heutschi *et al.* [10] compared spectra from point source and extended source calculations, showing that the ground effect cannot be accurately predicted using a point source assumption for a distance smaller than 400 m, see Figure 1.11.
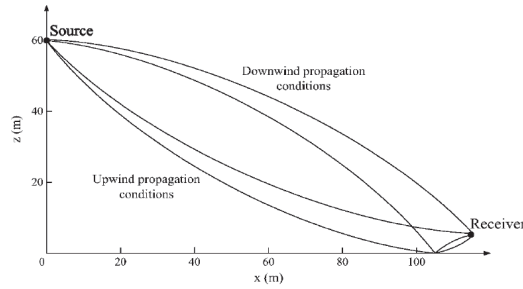
Figure 1.9: Downward and upward refraction for downwind and upwind propagation respectively. Taken from [8].
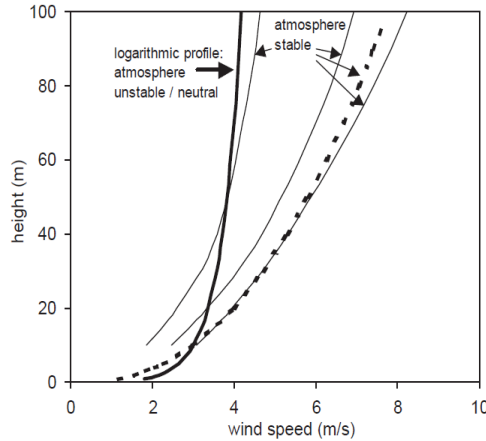
Figure 1.10: Measured wind profiles in a stable atmosphere. Taken from [9].

An accurate noise immission prediction relies on a good propagation model, that can take into account the atmospheric conditions and ground topography. To realize that, proper input parameters for atmospheric turbulence, wind shear, temperature variation etc from measurements or models are essential.

1.1.7   Noise mitigation

There are various ways of reducing wind turbine noise. For example, the airfoil profile can be modified to optimize the power and noise relation: trailing edge thickness design to reduce the bluntness noise; tip shape design to eliminate tip
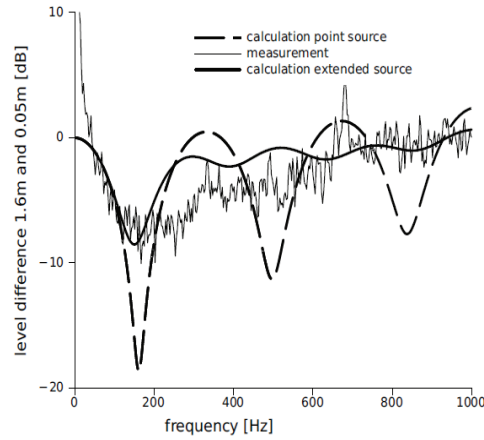
Figure 1.11: Measured and calculated (point source and extended source assumption) relative SPL of wind turbine noise received at 300 m away. Taken from [10].

noise; add-ons to improve blade performance etc, e.g. see Figure 1.12. A field measurement [36] shows that serrated blades yield an average trailing edge noise reduction of 3.2 dB, and the reduction level increases with increasing wind speed. Modification of turbine blades and/or operational characteristics (e.g. pitch angle) also showed success on reducing the amplitude modulation [37].
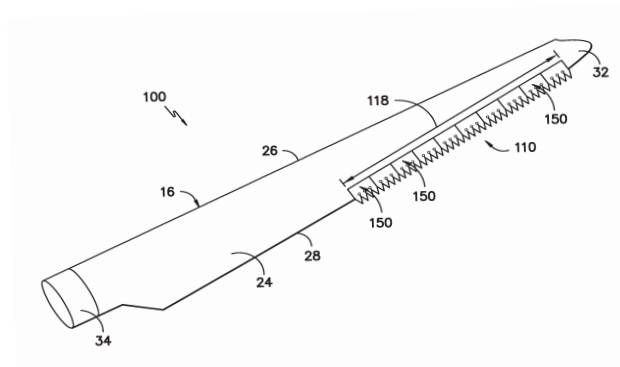
Figure 1.12: Schematic of using trailing edge add-ons (serration) to reduce trailing edge noise. Taken from [11].

1.2   Review of prediction methods for wind turbine noise sources and propagation

1.2.1   Aeroacoustic source models

There exists 3 main types of aeroacoustic source models that can be applied to wind turbine noise prediction: analytical models, semi-empirical models and numerical models.

Analytical models can be categorized into 3 groups according to Howe [38]:

1. theories based on the Fflowcs-Williams-Hawkings acoustic analogy, e.g. Casper and Farassat's time domain model [39];

2. theories based on the solution of special problems approximated by the linearized hydrodynamics equations, e.g. Amiet's analytical models [40, 41];

3. ad hoc models that involve postulated source distributions whose strengths and multipole types are generally determined empirically.

A time domain formulation was proposed by Farassat [42, 43], where several expressions in integral forms are presented for the determination of the acoustic field from a moving body. Body shape, time history of motion and surface pressure distribution are required as input parameters. Later, Casper and Farassat [44] published a new time domain formulation based on Ffowcs Williams-Hawkings equation, so called 'Formulation 1B'. The model is readily to be used for rotating frames, and has shown to provide excellent agreement with measurements [39]. It has been applied to wind turbine noise by Lee *et al.* [27]. Amiet [40] proposed a theoretical model for turbulent inflow noise. He assumed a homogeneous turbulent inflow which can be expressed by sinusoidal wave components and modeled by a von Kármán spectrum. The sound source is assumed to have a dipole character, and the force (surface pressure) exerted from the surface to the fluid is given by a transfer function. Thus, once the transfer function and the incoming turbulence properties are known, the sound generated by the surface pressure can be calculated. Amiet [41] later extended his work to trailing edge noise. A spectrum of surface pressure fluctuation field is required as an input for the model. Moreau and Roger [45] extended Amiet's model to take into account the backscattering effect due to the finite chord of the airfoil. Glegg *et al.* [46] attempted to apply Amiet's model to wind turbine noise, however the predictions are around 10 *dB* lower than the measurements. A TNO model originally proposed by Parchen [47] focus on trailing edge noise. It gives an alternative expression for wall pressure spectrum, which can be modeled by any CFD code that includes a turbulence model.

Besides analytical models, Brooks *et al.* [1] proposed a semi-empirical model for airfoil self-noise based on extensive measurements with NACA 0012 airfoils. It is sometimes called BPM model, after the name initials of the 3 authors. The scaling

is based on the analysis of Ffowcs Williams and Hall [48]. Later Fink [49] assumed a universal spectrum shape that depends only on the ratio of Strouhal number St, defined by $St = f\delta/U$, to its peak value St_{peak}, with f the acoustic frequency, δ the boundary layer thickness and U the free flow velocity. Brooks *et al.* proposed a slightly corrected spectral scaling based on their measurements. The general form of the scaled spectrum is given as [1]:

$$SPL_{1/3} = 10\log\left(M^5\frac{\delta^*L}{r_e^2}\right) + S(St) + K,\qquad(1.1)$$

where M is the Mach number, δ^* is the boundary layer displacement thickness, L is the span of the airfoil, and r_e is the retarded distance between source and observer. $S(St)$ is the universal spectrum shape that depends on Strouhal number St, and K is an empirical constant that modifies the level of the spectrum. For different noise mechanisms, the shape of $S(St)$ and the value of K are different, but they depend on boundary layer parameters δ^* and momentum thickness θ^*. Thus once these values are known, either by measurements or by simulations, the spectrum of sound pressure level in 1/3 octave band can be obtained.

The model is easy to implement, but the NACA 0012 airfoil used in their experiments is a not representative of wind turbine blade cross section. Also its validity for other airfoil profiles is questionable. However, Oerlemans *et al.* [3] and Zhu *et al.* [5] have applied this model on a wind turbine separately and have found good agreements with measurements, as seen in Figure 1.3.

There are also numerical methods based on CFD/CAA. Direct noise simulation is a numerical method that solves the Navier-Stokes equation for the flow and acoustic field without approximations. It is straightforward, but also time consuming and limited by the Reynolds number, see [50]. A hybrid method computes the flow field and the acoustic field separately. Hardin and Pope [51] proposed a LES model based computational aero-acoustics (CAA) method; it is further developed at DTU by Shen *et al.* [52, 53]. It is based on splitting the problem into a viscous incompressible flow part and an inviscid acoustic part. The flow part is solved by LES, and the acoustic part is then solved by solving a set of acoustic perturbation equations using the input data from the flow field. However, it remains difficult for the applications on a large size wind turbine with large Reynolds number.

1.2.2 Acoustic propagation models in the atmosphere

Analytical propagation models are limited to rather simple configurations, such as a point source above an impedance ground in homogeneous conditions [35].

For an inhomogeneous atmosphere, there exist many numerical models, among which we can cite ray-tracing methods, the parabolic equation (PE) method or Finite Difference Time Domain (FDTD) solution of linearized Euler equations(LEE).

Ray-tracing models calculate all the sound paths between the source and the receiver, then sum all the contributions of all the sound rays. It is based on the geometric approximation that is valid at high frequencies. Sound speed gradient can be taken into account. This method has been applied on wind turbine noise by Prospathopoulos and Voutsinas [54]. Another accurate numerical method is obtained using a parabolic approximation of the Helmholtz equation [55]. It is not limited to a layered atmosphere [35] and effects of atmospheric turbulence can be taken into account [56]. The PE method is limited to relatively small propagation angles around the source. Several authors have applied it to wind turbine noise assuming the wind turbine is a point source [57, 58]. Sound propagation can also be modeled by LEE in order to accurately account for atmospheric fluctuations. The LEEs can be solved using high order FDTD schemes, as done by Cotté *et al.* [59] or in EDF Code_Safari [60]. The LEE method requires more intensive computations compared to the PE method.

1.3   Objectives and outline

The promising future of the wind turbine industry and its noise concern encourage us to develop a physically-based noise prediction model that accounts for long range propagation in the atmosphere with satisfying accuracy and efficiency. After studying the existing models, we choose Amiet's analytical model with PE method for this purpose. More specifically, we will:

- investigate the validity of Amiet's model against measurements;

- apply the model to a full size rotating wind turbine;

- estimate the sound pressure level at near field and study the properties of amplitude modulation and directivity, including wind shear and atmospheric turbulence effects;

- couple the source model to the propagation model;

- examine the sound pressure level at far field and the effects of propagation in the atmosphere.

The thesis is organized as follows. In Chapter 2, Amiet's analytical models for trailing edge noise and turbulent inflow noise are described in detail. Extensions and improvements of the models are also shown. The model is then validated against sound pressure level measurements with fixed airfoils. In Chapter 3, the original model is adapted to a rotating blade, by considering the Doppler effect and coordinate transformation. Monin-Obukhov similarity theory is used to predict wind profiles and turbulence parameters in the atmospheric surface layer. The predictions are first compared with measurements for a constant wind profile, then with carefully chosen atmospheric conditions. In Chapter 4, a propagation model based

on the parabolic equation method is coupled to the source model. Propagation effects on overall noise immision, as well as on the amplitude modulation in far field are studied. Conclusions and perspectives are given in Chapter 5.

Amiet's model for the aerodynamic noise of a fixed airfoil

Contents

In this chapter, we present and validate Amiet's theory for a fixed airfoil. In Section 2.1, Amiet's model for trailing edge noise is derived. The difficult part of the model is to estimate the wall pressure fluctuation spectrum. We use an adverse pressure gradient model that yields good predictions against wind tunnel measurements. The turbulent inflow noise model is presented in Section 2.2. We take into account the effect of airfoil thickness on the noise radiation, and validate the model against measurements.

2.1   Amiet's theory for trailing edge noise

2.1.1   Derivation of Amiet's model for trailing edge noise

Amiet's model is based on linearized acoustic theory by assuming a small perturbation on the acoustic field [41]. The turbulence convected by the mean flow is assumed to be 'frozen', that is to say the turbulence properties don't change during the convection. The surface is considered as a rigid, thin plate with no thickness. The model development consists of mainly 3 steps:

1. calculation of surface pressure fluctuation induced by the turbulent perturbation;

2. deduction of far field pressure fluctuation using Ffowcs-Williams-Hawkings acoustic analogy;

3. obtaining the statistic power spectral density of sound pressure level at far field.

The model is later extended by Roger and Moreau [45, 61] by considering a second order iteration at leading edge.

Induced surface pressure fluctuation

Noise is generated when incoming turbulence encounters a solid surface, more specifically, the airfoil in this case. The problem is shown in figure 2.1. The airfoil is considered as a flat plate with zero angle of attack. It is placed in the $z = 0$ plane, the trailing edge is aligned with y axis, therefore the plate is located between $-2b \leq x \leq 0$ in the chord-wise direction, b being the half-chord length, $b = c/2$. The span L is considered as a large but finite number.
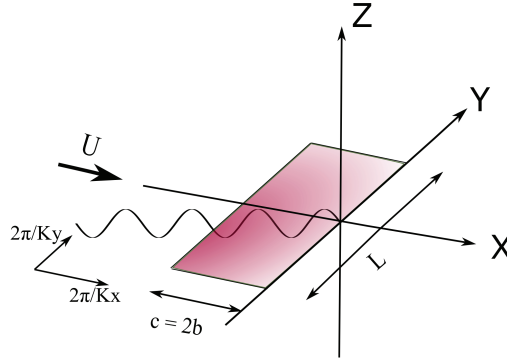
Figure 2.1: 3D geometry for trailing edge noise. We consider an oblique gust with chord-wise wavenumber K_x and span-wise wavenumber K_y.

We consider a general 3D gust case. The derivation starts from the convective linear wave equation, in terms of pressure fluctuation $p(\mathbf{x}, t) = P(x, y, z)e^{i\omega t}$:

$$\frac{D^2 p}{Dt^2} - c_0^2 \nabla^2 p = 0. \tag{2.1}$$

where c_0 is the sound speed in air. The total derivative in x direction reads $\frac{D}{Dt} = \frac{\partial}{\partial t} + U\frac{\partial}{\partial x}$, so the second order derivative can be written as:

$$\frac{D^2}{Dt^2} = \frac{\partial^2}{\partial t^2} + 2U\frac{\partial}{\partial x}\frac{\partial}{\partial t} + U^2\frac{\partial^2}{\partial x^2}. \tag{2.2}$$

The equation (2.1) therefore becomes:

$$\left(\frac{\partial^2 p}{\partial x^2} + \frac{\partial^2 p}{\partial y^2} + \frac{\partial^2 p}{\partial z^2}\right) - \frac{1}{c_0^2}\left(\frac{\partial^2 p}{\partial t^2} + 2U\frac{\partial^2 p}{\partial x \partial t} + U^2\frac{\partial^2 p}{\partial x^2}\right) = 0, \tag{2.3}$$

which can be reorganized as:

$$\beta_0^2\frac{\partial^2 p}{\partial x^2} + \frac{\partial^2 p}{\partial y^2} + \frac{\partial^2 p}{\partial z^2} - 2\frac{U}{c_0^2}\frac{\partial^2 p}{\partial x \partial t} - \frac{1}{c_0^2}\frac{\partial^2 p}{\partial t^2} = 0, \tag{2.4}$$

with $\beta_0 = \sqrt{1 - M^2}$. The incident gust written in the Fourier domain is:

$$p_{in} = P_{in}\, e^{i(\omega t - K_c x - K_y y)}, \tag{2.5}$$

where $K_c = \omega/U_c$ is the turbulence convected wavenumber in the chord-wise direction and K_y is the span-wise turbulence wavenumber. The convective velocity is $U_c = \chi U$ where χ is a coefficient, usually less than 1. The pressure fluctuation field p is imposed by p_{in} with wave like behaviors, that is, p will have a periodic component with the same frequency ω, and the same wave number in span-wise direction K_y. It is not the case for chord-wise direction wavenumber, because in this direction, the field is also modified by the free stream U. Therefore the solution we seek for p can be written in the form:

$$p(\mathbf{x}, t) = P(x, z)e^{i\omega t}e^{-iAx}e^{-iK_y y}. \tag{2.6}$$

Substituting p into Equation (2.4), the convective wave equation becomes:

$$\beta_0^2\frac{\partial^2 P}{\partial x^2} + \frac{\partial^2 P}{\partial z^2} - 2i\left(\beta_0^2 A + \frac{U}{c_0^2}\omega\right)\frac{\partial P}{\partial x} + \left(\frac{\omega^2}{c_0^2} - \beta_0^2 A^2 - \frac{2U}{c_0^2}A\omega - K_y^2\right)P = 0. \tag{2.7}$$

The coefficient of the imaginary term should be zero, that is $\beta_0^2 A + \dfrac{U}{c_0^2}\omega = 0$, thus we find the expression for A as:

$$A = -\frac{kM}{\beta_0^2}, \tag{2.8}$$

where $k = \omega/c_0$ is the acoustic wave number. The pressure fluctuation field that we are trying to solve can be written as:

$$p(\mathbf{x}, t) = P(x, z)e^{i\omega t}e^{ikM/\beta_0^2 x}e^{-iK_y y}. \tag{2.9}$$

Consequently, equation (2.7) is simplified as:

$$\beta_0^2\frac{\partial^2 P}{\partial x^2} + \left(\frac{k^2}{\beta_0^2} - K_y^2\right)P + \frac{\partial^2 P}{\partial z^2} = 0. \tag{2.10}$$

If we introduce non-dimensional variables:

$$\bar{x} = \tfrac{x}{b}, \qquad \bar{y} = \beta_0\tfrac{y}{b}, \quad \bar{z} = \beta_0\tfrac{z}{b},$$
$$\bar{K}_c = bK_c, \quad \bar{K}_y = bK_y, \quad \bar{k} = bk,$$

and also non-dimensional new parameters $\bar{\mu} = \bar{K}_c M/\beta_0^2$ and $\bar{\kappa}^2 = \bar{\mu}^2 - \bar{K}_y^2/\beta_0^2$ to make equation (2.10) more concise, we finally find a Helmholtz equation as:

$$\frac{\partial^2 P}{\partial \bar{x}^2} + \frac{\partial^2 P}{\partial \bar{z}^2} + \bar{\kappa}^2 P = 0. \tag{2.11}$$

To solve equation (2.11), we need to find appropriate boundary conditions. We first assume the plate is semi-infinite with a trailing edge aligned with y axis, and the leading edge is at $-\infty$. The plate is considered as rigid, meaning the velocity gradient normal to the surface is zero, this gives:

$$\frac{\partial P}{\partial \bar{z}} = 0, \quad \bar{x} < 0. \tag{2.12}$$

Second, at trailing edge, Kutta condition requires the total pressure to be zero, meaning, the induced pressure p must be canceled by the incident pressure p_{in}, so we have $p + p_{in} = 0$ for $z = 0$ and $\bar{x} \geq 0$. This gives:

$$\begin{aligned} p(x,y,0,t) &= -p_{in}(x,y,0,t) = -P_{in} \cdot e^{-iK_c x} e^{-iK_y y} e^{i\omega t} \\ &= P(x,0) \cdot e^{i\frac{kM}{\beta_0^2}x} e^{-iK_y y} e^{i\omega t} \quad \bar{x} \geq 0. \end{aligned} \tag{2.13}$$

Thus we obtain for a unit gust ($P_{in} = 1$):

$$P(x,0) = -e^{-iK_c x} e^{-i\frac{kM}{\beta_0^2}x} \quad \bar{x} \geq 0. \tag{2.14}$$

Equation (2.11), together with boundary conditions (2.12) and (2.14) form a Schwarzschild's problem, whose solution can be expressed analytically. Depending on the sign of $\bar{\kappa}^2$, equation (2.11) has different properties thus different solutions: 1) if $\bar{\kappa}^2 > 0$, the equation is hyperbolic, and the gust is called super-critical; 2) if $\bar{\kappa}^2 < 0$, the equation is elliptic, and the gust is called sub-critical; 3) if $\bar{\kappa}^2 = 0$, the gust is critical.

Roger and Moreau [45] give detailed solutions for super- and sub-critical cases for p. For the super-critical case, the solution is obtained from Schwarzschild's problem:

$$\begin{aligned} P(\bar{x},0) &= -\frac{1}{\pi} \int_0^\infty \sqrt{\frac{-\bar{x}}{\xi}} \cdot \frac{e^{-i\bar{\kappa}(\xi - \bar{x})}}{\xi - \bar{x}} \cdot e^{-i\bar{K}_c \xi (\frac{1}{\chi} + \frac{M^2}{\beta_0^2})} d\xi \\ &= -\frac{e^{i\bar{\kappa}\bar{x}}}{\pi} \cdot \int_0^\infty \sqrt{\frac{-\bar{x}}{\xi}} \frac{e^{-i\xi(\bar{K}_c/\chi + \bar{\kappa} + M\bar{\mu})}}{\xi - \bar{x}} d\xi. \end{aligned} \tag{2.15}$$

The integration is calculated as:

$$\int_0^\infty \sqrt{\frac{\bar{x}}{\xi}} \frac{e^{-iB\xi}}{\xi - \bar{x}} d\xi = \pi e^{-iBx} \left[1 - \frac{e^{i\pi/4}}{\pi} \int_0^{-B\bar{x}} \frac{e^{-it}}{\sqrt{t}} dt \right],$$
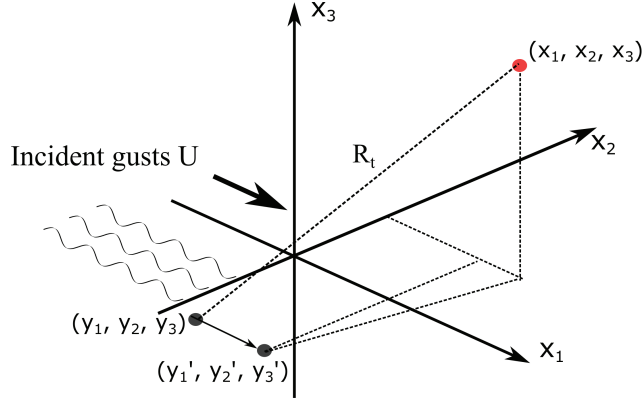
Figure 2.2: Illustration of source being convected by the incident gusts.

with $B = \bar{K}_c/\chi + \bar{\kappa} + M\bar{\mu}$. We recognize that:

$$E^*(x) = \int_0^x \frac{e^{-it}}{\sqrt{2\pi t}}\,dt = C_1(x) - iS_1(x), \qquad (2.16)$$

where C_1 and S_1 are Fresnel integrals. Then we obtain pressure fluctuation as:

$$P(\bar{x}, 0) = e^{-i\bar{x}\bar{K}_c/\chi} f(\bar{x}). \qquad (2.17)$$

where $f(\bar{x}) = [(1+i)E^*(-B\bar{x}) - 1]$ is the complex amplitude of the source distribution. Since in reality the plate is not semi-infinite, but with a finite chord length $c = 2b$, the first boundary condition (Eq. (2.12)) is no longer fulfilled for $x < -2b$ (or $\bar{x} < -2$). Therefore it is necessary to perform a 2nd iteration, corresponding to the leading edge back-scattering. This 2nd iteration is important when the chord is small compared to the acoustic wavelength, and can generally be neglected for wind turbine noise, as shown in Figures 5 and 6 of [45]. More details on the back-scattering correction are given in Appendix A.

Far-field noise calculations

Induced pressure field is now linked to the far field sound pressure level. We assume the observer coordinate is (x_1, x_2, x_3), the source coordinate is (y_1, y_2, y_3) at retarded time, and at current time, the source coordinate is (y_1', y_2', y_3'). The movement of the source is caused by the convective effect of the free stream, as shown in figure 2.2. According to Fflowcs-Williams-Hawkings Analogy, the sound radiation at far field due to a dipole source (a point force) for an unbounded medium can be expressed as [40]:

$$dp'(\vec{x}_i, t) = \frac{\vec{R}_t}{4\pi c_0 R_s^2} \cdot \left[\frac{\partial \vec{F}}{\partial t} \right], \qquad (2.18)$$

where the term inside [ ] is evaluated at retarded time. To obtain the acoustic pressure at the receiver, we integrate equation (2.18) over the flat plate surface S,

and transform it into the Fourier space:

$$
\begin{aligned}
\tilde{p}(\vec{x}_i,\omega) &= \frac{1}{2\pi}\int_S \frac{R_3}{4\pi c_0 R_s^2}\int_\infty^\infty \left[\frac{\partial l(\vec{y},t')}{\partial t'}\right]_{t-R_t/c_0} e^{-i\omega t}\,dtdS \\
&= \int_S \frac{i\omega R_3}{4\pi c_0 R_s^2}\frac{1}{2\pi}\int_{-\infty}^\infty \frac{l(\vec{y},t)}{dt}e^{-i\omega(t+R_t/c_0)}\,dtdS \\
&= \int_S \frac{i\omega R_3}{4\pi c_0 R_s^2}\tilde{l}(\vec{y},\omega)e^{-i\omega R_t/c_0}\,dS,
\end{aligned}
\tag{2.19}
$$

where $dS = dy_1\cdot dy_2$, and $R_i = \sqrt{x_i - y_i}$, $i = 1,2,3$. We must emphasize that the plate is not considered semi-infinite anymore at this stage. Note also that $\tilde{l}(\vec{y},\omega)$ is the Fourier transform of $l(\vec{y},t)$, the lift force due to the pressure jump on the plate surface, and it is identical to the pressure fluctuation p mentioned in the previous section:

$$
d\vec{F} = l(y_1,y_2,t)dS_y\vec{e}_3 = p(y_1,y_2,t)dS_y\vec{e}_3,
\tag{2.20}
$$

and $\vec{F}$ has only the $\vec{e}_3$ component. The derivation from retarded time t' to the current time t by assuming $l(\vec{y},t) = l_0(\vec{y})e^{i\omega t}$ is thus

$$
\left[\frac{\partial l(\vec{y},t')}{\partial t'}\right]_{t-\frac{R_t}{c_0}} = \frac{\partial l_0(\vec{y})e^{i\omega(t-\frac{R_t}{c_0})}}{\partial t}\frac{dt}{dt'} = i\omega l_0(\vec{y})e^{i\omega t}e^{-i\omega\frac{R_t}{c_0}} = i\omega l(\vec{y},t)e^{-i\omega\frac{R_t}{c_0}}.
\tag{2.21}
$$

$\vec{R}_t$ is the position vector between the retarded source location and the observer, and R_s is a modified distance defined as:

$$
R_s^2 = R_1^2 + \beta_0^2(R_2^2 + R_3^2) = (x_1 - y_1)^2 + \beta_0^2((x_2 - y_2)^2 + (x_3 - y_3)^2).
\tag{2.22}
$$

Since $y_1' = y_1 + U\frac{R_t}{c_0}$ with $\frac{R_t}{c_0}$ the propagation time, we can express $\vec{R}_t$ as:

$$
\left(x_1 - y_1 - U\frac{R_t}{c_0}\right)^2 + (x_2 - y_2)^2 + (x_3 - y_3)^2 = R_t^2.
\tag{2.23}
$$

We then solve this second order equation for R_t and get:

$$
\begin{aligned}
R_t &= \frac{-M|x_1 - y_1| + \sqrt{(x_1 - y_1)^2 + \beta_0^2[(x_2 - y_2)^2 + (x_3 - y_3)^2]}}{\beta_0^2} \\
&= (R_s - MR_1)/\beta_0^2.
\end{aligned}
\tag{2.24}
$$

If we further assume that the observer is at far field, that is $x_1 \gg y_1$, $x_2 \gg y_2$, and note $y_3 = 0$ on the airfoil surface, we can approximate R_s as:

$$
\begin{aligned}
R_s^2 &= (x_1 - y_1)^2 + \beta_0^2\left[(x_2 - y_2)^2 + (x_3 - y_3)^2\right] \\
&= [x_1^2 + \beta_0^2(x_2^2 + x_3^2)]\left[1 + \frac{y_1^2 - 2x_1y_1 + \beta_0^2 y_2^2 - 2\beta_0^2 x_2 y_2}{x_1^2 + \beta_0^2(x_2^2 + x_3^2)}\right] \\
&\simeq S_0^2\left[1 - \frac{2(x_1y_1 + \beta_0^2 x_2 y_2)}{S_0^2}\right],
\end{aligned}
\tag{2.25}
$$

with $S_0 = \sqrt{x_1^2 + \beta_0^2(x_2^2 + x_3^2)}$. Thus:

$$
\begin{aligned}
R_s &\simeq S_0 \left(1 - \frac{2(x_1 y_1 + \beta_0^2 x_2 y_2)}{S_0^2} \right)^{\frac{1}{2}} \\
&\simeq S_0 \left(1 - \frac{x_1 y_1 + \beta_0^2 x_2 y_2}{S_0^2} \right) \quad \text{(Taylor expansion)}.
\end{aligned} \tag{2.26}
$$

If we write $P(\bar{y}_1, \bar{y}_2) = f(\bar{y}_1)e^{-i(\bar{K}_x \bar{y}_1 + \bar{K}_y \bar{y}_2)}$, with $\bar{K}_x = \omega/U = \chi \bar{K}_c$, the radiation integral becomes:

$$
\begin{aligned}
\tilde{p}(\vec{x}_i, \omega) &= \frac{-i\omega x_3}{4\pi c_0 S_0^2} b^2 \int_{-2}^{0} \int_{-L/2b}^{L/2b} f(\bar{y}_1) e^{-i(\bar{K}_x \bar{y}_1 + \bar{K}_y \bar{y}_2)} \\
&\qquad \cdot e^{-i\frac{k}{\beta_0^2}[S_0 - \frac{x_1 \bar{y}_1 + \beta_0^2 x_2 \bar{y}_2}{S_0}b - M(x_1 - b\bar{y}_1)]} \, d\bar{y}_1 d\bar{y}_2.
\end{aligned} \tag{2.27}
$$

To obtain this expression, we used Equation (2.26) for the phase, and $R_s \simeq S_0$ for the amplitude. The integral concerning $\bar{y}_2$ is

$$
b \int_{-L/2b}^{L/2b} e^{-i\bar{K}_y \bar{y}_2} e^{-i\frac{k}{\beta_0^2} \cdot (-\frac{\beta_0^2 x_2 b}{S_0})\bar{y}_2} \, d\bar{y}_2 = L \, \text{sinc} \left\{ \frac{L}{2b} \left(\bar{K}_y - \bar{k}\frac{x_2}{S_0} \right) \right\}, \tag{2.28}
$$

where $\text{sinc}(x) = \sin(x)/x$ and this leads to

$$
\begin{aligned}
\tilde{p}(\vec{x}_i, \omega) &= \frac{-i\omega L x_3 b}{4\pi c_0 S_0^2} \, \text{sinc}\left[\frac{L}{c}(\bar{K}_y - \bar{k}x_2/S_0) \right] \\
&\qquad \cdot e^{-i\frac{k}{\beta_0^2}(S_0 - Mx_1)} \int_{-2}^{0} f(\bar{y}_1) e^{-i\bar{y}_1[\bar{K}_x - \mu(x_1/S_0 - M)]} \, d\bar{y}_1.
\end{aligned} \tag{2.29}
$$

Power spectrum density of acoustic pressure at far field

The power spectral density of the far-field sound at frequency ω is the results of all the 3D gusts. If we assume the turbulence is 'frozen' while convected by the mean flow inside the boundary layer, then the chord-wise wave number for this frequency is selected by $K_x = K_c = \omega/U_c$ where U_c is the convected velocity and K_c is the convected wave number. Thus the fluctuating wall pressure field can be expressed as

$$
P(\vec{x}_i, \omega) = \frac{1}{U_c} \int_{-\infty}^{\infty} g\left(x_1, \frac{\omega}{U_c}, K_y \right) A_0\left(\frac{\omega}{U_c}, K_y \right) e^{-iK_y x_2} \, dK_y, \tag{2.30}
$$

where g is a transfer function that connects the incident pressure perturbation p_{in} of amplitude A_0 to the pressure field P. If we assume the surface pressure fluctuation caused by the turbulence to be a stationary random process, then we can analyze $P(\vec{x}_i, \omega)$ statistically. The power spectral density between 2 points on the airfoil surface $\vec{y}$ and $\vec{y}'$ is defined as

$$
S_{PP} = \frac{1}{U_c} \int_{-\infty}^{\infty} g(y_1, \frac{\omega}{U_c}, K_y) \, g^*(y_1', \frac{\omega}{U_c}, K_y) e^{-iK_y \eta} \Pi_0\left(\frac{\omega}{U_c}, K_y \right) \, dK_y, \tag{2.31}
$$

where $\eta = y_2 - y_2'$, Π_0 is the wavenumber spectrum of the incident gust amplitude A_0, and is estimated by Schlinker and Amiet [62] as

$$\Pi_0 \left(\frac{\omega}{U_c}, \bar{K}_y \right) = \frac{U_c}{\pi} \Phi_{pp}(\omega) l_y(\omega, K_y), \tag{2.32}$$

with Φ_{pp} the surface pressure fluctuation spectrum, and l_y the span-wise correlation length. Corcos [63] proposed a model that connects this correlation length to the flow velocity as:

$$l_y(\omega, K_y) = \frac{\omega/(b_c U_c)}{K_y^2 + \omega^2/(b_c U_c)^2}. \tag{2.33}$$

with b_c a constant that should be measured experimentally. In the mid-span plane, the correlation length reduces to the classical result:

$$l_y(\omega) = \frac{b_c U_c}{\omega}. \tag{2.34}$$

However, it is needed to note that use of Corcos model at low frequency range is limited, more investigations on the model are desired for low frequency noise study. The power spectral density of far field sound is then obtained from Eq. (2.29) and (2.31) as:

$$\begin{aligned} S_{pp}(\vec{x}, \omega) &= \left(\frac{\omega L x_3}{4\pi c_0 S_0^2} \right)^2 \frac{c}{2\pi} \int_{-\infty}^{\infty} \Phi_{pp}(\omega) \\ & \quad \text{sinc}^2 \left\{ \frac{L}{c}(\bar{K}_y - \bar{k} x_2/S_0) \right\} \left| \mathscr{L} \left(\frac{\omega}{U_c}, \bar{K}_y \right) \right|^2 l_y(\omega, K_y) \, d\bar{K}_y, \end{aligned} \tag{2.35}$$

where $\mathscr{L}$ is the airfoil transfer function (integral form of g). Equation (2.35) is an exact solution that requires the integration over all y_2 direction wavenumbers. However, a simplification can be made by studying the property of the $\text{sinc}(x)$ function. If L/b is large, $\text{sinc}^2(x)$ can be approximated by a Delta function:

$$\text{sinc}^2 \left\{ \frac{L}{2b}(\bar{K}_2 - \bar{k} \frac{x_2}{S_0}) \right\} \simeq \frac{2\pi b}{L} \delta(\bar{K}_2 - \bar{k} \frac{x_2}{S_0}). \tag{2.36}$$

This means for each frequency ω, there is only one privileged oblique gust $\bar{K}_y = \bar{k} \frac{x_2}{S_0}$ will efficiently radiate to the far field, therefore the exact solution reduces to a simplified solution:

$$S_{pp}(\vec{x}, \omega) = \left(\frac{\omega c x_3}{4\pi c_0 S_0^2} \right)^2 \frac{L}{2} \left| \mathscr{L} \left(\frac{\omega}{U_c}, \frac{\bar{k} x_2}{S_0} \right) \right|^2 \Phi_{pp}(\omega) l_y \left(\omega, \bar{k} \frac{x_2}{S_0} \right). \tag{2.37}$$

Derivation of transfer function $\mathscr{L}$ is given by Roger and Moreau [45] for super-critical and sub-critical cases respectively. For super-critical case

$$\mathscr{L} = \mathscr{L}_1 + \mathscr{L}_2 = \int_{-2}^{0} [f_1(\bar{y}_1) + f_2(\bar{y}_1)] e^{-iC\bar{x}} \, d\bar{x}, \tag{2.38}$$

where $f_2(\bar{y}_2)$ corresponds to the leading edge correction term P_2. For the first order term, we have:

$$\mathcal{L}_1 = -\frac{e^{2iC}}{iC}\left\{(1+i)e^{-2iC}\sqrt{\frac{B}{B-C}}E^*[2(B-C)] - (1+i)E^*(2B) + 1\right\}, \quad (2.39)$$

where $C = \bar{K}_c - \bar{\mu}(x_1/S_0 - M)$. As explained by Roger and Moreau [45], this expression includes the incident pressure jump correction proposed by Amiet [64]. Expressions for $\mathcal{L}_2$ and for sub-critical gusts are given in Appendix A.

2.1.2 Wall pressure spectrum model

2.1.2.1 Existing models for wall pressure fluctuation

Amiet's model uses airfoil response functions to connect the surface pressure fluctuation spectrum to the acoustic pressure jump at a far field point. A key element for estimating the far field SPL accurately is to estimate correctly the surface pressure fluctuation spectrum. Since the wall pressure fluctuation is characterized statistically, it is usually expressed in the form of power spectral density functions in the frequency domain [65].

Numerical models An accurate estimation of wall pressure fluctuation spectrum can be obtained with direct numerical simulation (DNS) or large eddy simulation (LES). However these computations are really time consuming and are limited to relatively small Reynolds numbers. A less computational expensive method is to perform Reynolds Averaged Navier-Stokes Simulation (RANS) with a turbulence model.

Analytical models for zero pressure gradient Another technique for obtaining wall pressure fluctuation spectrum is called scaling law method. It is based on extensive flow measurements, and trying to find appropriate scaling parameters to make all the normalized spectral curves collapse together. Scaling parameters can be inner and/or outer variables of the boundary layer. Inner variables correspond to the region where the velocity is a function of viscosity and wall shear stress, while outer variables correspond to the region where the velocity depends on the external velocity and the boundary layer thickness δ. In Amiet's original paper for trailing edge noise [41], he suggested an empirical formula based on the Willmarth and Roos' experimental data, by scaling with a single outer variable δ^*:

$$\frac{\Phi_{pp}(\omega)}{\rho_0\delta^*U_e^3} = 2\cdot10^{-5}\frac{F(\tilde{\omega})}{2}, \quad (2.40)$$

where

$$F(\tilde{\omega}) = (1 + \tilde{\omega} + 0.217\tilde{\omega}^2 + 0.00562\tilde{\omega}^4)^{-1}, \quad (2.41)$$

with $\tilde{\omega} = \omega\delta^*/U_e$ the reduced frequency, δ^* the displacement thickness and U_e the external velocity. Since the small scales in the boundary layer are not well represented by this outer variable, Amiet's model does not give a good collapse in the high frequency range. Later, Goody [66] attributed the high frequency discrepancies of Amiet's single parameter model to the Reynolds number effect, and thus proposed an improved model that takes into account this effect by using mixed (inner and outer) variables:

$$\frac{\Phi_{pp}(\omega)U_e}{\tau_w^2\delta} = \frac{c_2(\omega\delta/U_e)^2}{[(\omega\delta/U_e)^{0.75} + c_1]^{3.7} + [c_3(\omega\delta/U_e)^7]}, \tag{2.42}$$

where $\tau_w = \mu(dU_e/dy)$ is the wall shear stress, and the constants c_1, c_2 and c_3 are suggested to be 0.5, 3.0 and $1.1R_T^{-0.57}$ respectively, with $R_T = (\delta/U_e)/(\nu/u_*^2)$ the ratio of the outer to inner boundary layer time scales, ν the air kinematic viscosity, and u_* the friction velocity.

Adverse pressure gradient model Considering the application of Amiet's model on a real size wind turbine, it is preferable to use a scaling formula for the wall pressure fluctuation spectrum for its efficiency. However, both Amiet's one parameter model and Goody's model are for a zero pressure gradient (ZPG) flow condition, that is to say for a plat plate with a fully developed boundary layer. It is not realistic for an airfoil where an adverse pressure gradient (APG) is observed before the trailing edge. To take into account this effect, Rozenberg *et al.* [67] proposed a more complex model based on Goody's model and various experimental and numerical data. In this APG wall pressure spectrum model, two new parameters are introduced: Δ and β_c. $\Delta = \delta/\delta^*$ is the ratio between boundary layer thickness δ and displacement thickness δ^*, and β_c is an indicator for the surface pressure gradient. Then Φ_{pp} scales as

$$\frac{\Phi_{pp}(\omega)U_e}{\tau_{max}^2\delta^*} = \frac{\left[2.82\Delta^2(6.13\Delta^{-0.75} + F_1)^{A_1}\right]\left[4.2\cdot\left(\frac{\Pi}{\Delta}\right)\right]\tilde{\omega}^2}{[4.76\tilde{\omega}^{0.75} + F_1]^{A_1} + [8c_3\tilde{\omega}]^{A_2}}, \tag{2.43}$$

where the main parameters of the model are [67]:

- the wake strength parameter $\Pi = 0.8(\beta_c + 0.5)^{3/4}$,

- the Clauser parameter $\beta_c = \frac{\theta^*}{\tau_w}\frac{dp}{dx}$ that compares pressure forces on the boundary layer to the wall shear forces,

- the ratio of boundary layer thickness to displacement thickness $\Delta = \delta/\delta^*$,

with θ^* the momentum thickness, τ_{max} the maximum shear stress along the normal direction, and $\frac{dp}{dx}$ the pressure gradient. In addition, A_1, A_2 and F_1 are empirical
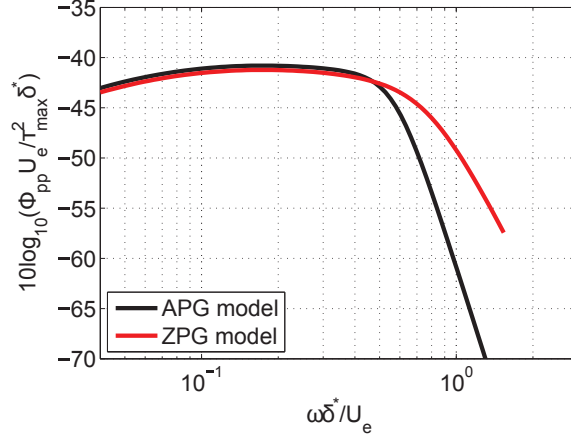
Figure 2.3: Normalized wall pressure spectrum for APG model and Goody's ZPG model for $\beta_c = 0$.

coefficients given by:

$$A_1 = 3.7 + 1.5\beta_c, \tag{2.44}$$

$$A_2 = \min(3, 19/\sqrt{R_T}) + 7, \tag{2.45}$$

$$F_1 = 4.76 \left(\frac{1.4}{\Delta}\right)^{0.75} [0.375A_1 - 1]. \tag{2.46}$$

Compared to Goody's model, the proposed APG model uses δ^* instead of δ, τ_w is replaced by τ_{max}, which is the maximum shear stress in the normal direction of the airfoil surface. Wake strength parameter Π can be measured by experiment, however, Rozenberg [67] cited an empirical formula that relates Π and β_c as:

$$\Pi = 0.8(\beta_c + 0.5)^{3/4}.$$

APG model is then coded in MATLAB to perform some parametric study and validations. All the necessary input parameters can be calculated by using CFD tools. Here, XFOIL (version 6.96) is used. β_c is the key parameter for this model as it quantifies the local pressure gradient. The first validation is done by setting β_c to 0; it is expected that APG model reduces to Goody's model. The parameters used are the data for V2 airfoil at the location RMP23 (cf [67]), except that Δ is set to 8 instead of 3.9. The result is shown in figure 2.3.

We can see that when the pressure gradient is set to 0, the two models produce the same spectra at low frequency, but APG model shows a more rapid decrease slop at high frequency. This is because Rozenberg considers that as $\omega \rightarrow \infty$, spectral level should decay faster than ω^{-5} according to the experimental data that he has collected.

To study the effects of the adverse pressure parameters, we gradually vary one parameter, while keeping the other ones fixed. In Figure 2.4, when we vary Δ, β_c and Π are held constant at 2.5 and 1.82 respectively; on the other hand, when we gradually vary β_c and Π, Δ is held constant at 8. From the results, we can see that when β_c is fixed, along with decreasing Δ, the spectral peak moves to higher frequencies, and an increase in the peak value is observed. When we fix Δ and gradually decrease β_c, the spectra becomes flatter in the middle range by increasing the level on the right side of the spectra peak.

(a) $\Delta \in [2 \ \ 8]$.   (b) $\beta_c \in [0 \ \ 4]$.
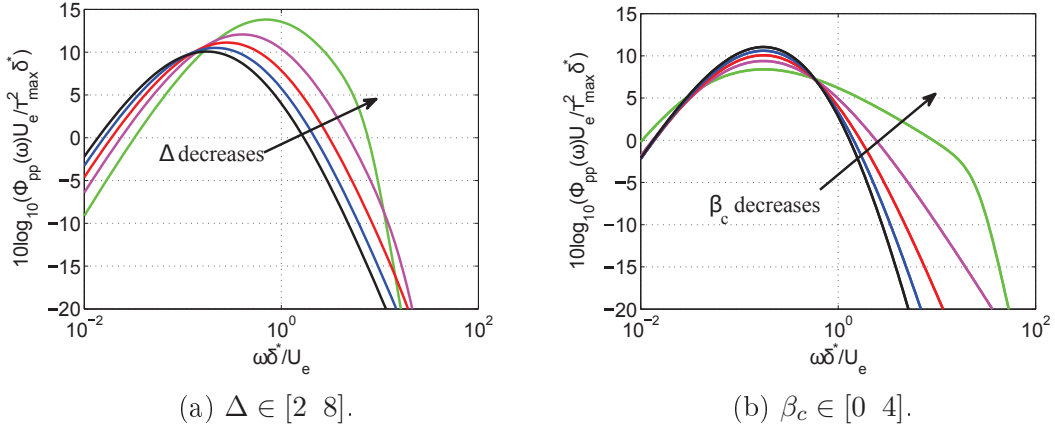
Figure 2.4: Behaviors of adverse pressure parameters in APG model.

Note that other wall pressure fluctuation models exist, such as the TNO-Blake model. Some recent studies have shown that turbulence anisotropy effects need to be included to improve the model accuracy [12, 68]. In this modified TNO-Blake model, the turbulence intensity and integral length-scale are allowed to be different in the three orthogonal directions.

2.1.2.2 Parametric study for boundary layer related terms using XFOIL

XFOIL is an interactive program for the analysis of isolated airfoils in incompressible potential flows. The geometry of the airfoil is divided into piecewise straight line panels with associated vortex sheets [69]. All input parameters and flow settings can be realized by command lines. In XFOIL, an option xtr controls the transition point. By default, $xtr = 1$ for both sides, standing for a free transition.

Wind tunnel turbulent intensity is determined by a N_{crit} value in XFOIL. N_{crit} is the critical N value for e^n method, it is the log of the amplification factor of the most amplified frequency which triggers transition [19]: $N_{crit} = -8.43 - 2.4 \ln(I\%/100\%)$, with I being the turbulence intensity. A suitable value of N_{crit} depends on the ambient disturbance level in which the airfoil operates, and mimics the effect of such disturbances on transition. Table 2.1 gives typical values of N_{crit} for various situations.

situation	N_{crit}	Correspond I (%)	
sailplane	12-14	0.02 - 0.009	
motor glider	11-13	0.03 - 0.01	
clean wind tunnel	10-12	0.05 - 0.02	
average wind tunnel	9	0.07	$\leftarrow$ standard e^9 method
dirty wind tunnel	4-8	0.56 - 0.11	

Table 2.1: Classification of N_{crit} with corresponding wind tunnel conditions [19].

N_{crit} value has an effect on the laminar-to-turbulence transition point on the airfoil surface, as seen in Figure 2.5 for a symmetric NACA 0012 airfoil and a cambered NACA 63-415 airfoil (see Figure 2.6). Lower N_{crit} (higher turbulence intensity) leads to a transition point closer to the leading edge. If the turbulent intensity is not mentioned explicitly, default value $Ncrit = 9$ is used. In XFOIL, directly obtained parameters are δ^*, θ^*, skin friction coefficient C_f, and pressure distribution. Boundary layer thickness δ is calculated by a formula given in [70]:

$$\delta = \theta^* \left(3.15 + \frac{1.72}{H_k - 1} \right) + \delta^*, \tag{2.47}$$

where $H_k = \delta^*/\theta^*$ is the kinematic shape factor. We cannot estimate τ_{max} from XFOIL, so we assume $\tau_{max} = \tau_w$ in the following, with $\tau_w = \frac{1}{2}\rho U^2 C_f$.

(a) NACA 0012   (b) NACA 63-415
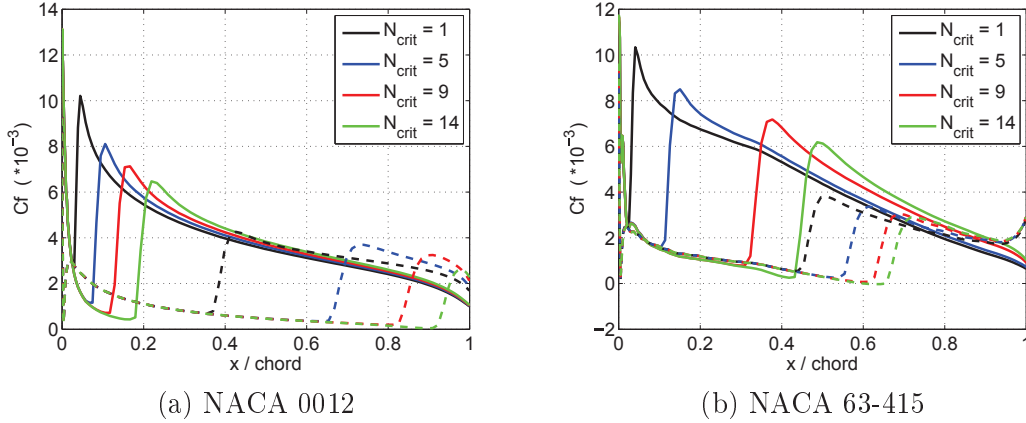
Figure 2.5: Skin coefficient C_f for different N_{crit} values. AoA $= 4^o$ and $Re = 4 \cdot 10^6$ for all cases. Solid lines: suction sides; dashed lines: pressure sides.

Rozenberg's wall pressure model is proposed for an adverse pressure gradient flow condition. At the same time, the flow should not be detached. Figures 2.7 and 2.8 show the pressure and skin friction coefficients around NACA 0012 and NACA 63-415 airfoil surfaces, respectively. The Reynolds number is $4 \cdot 10^6$ and the test AoA are $0^o, 5^o$ and 10°. N_{crit} value is set as 9, and a free transition
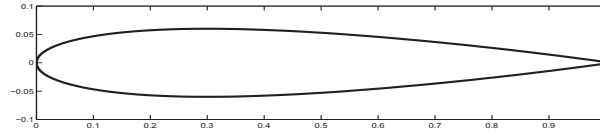
(a) Profile of a NACA 0012 airfoil.
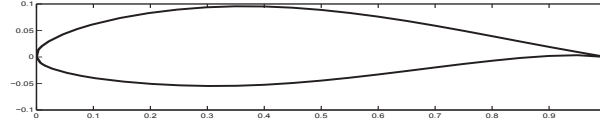
(b) Profile of a NACA 63-415 airfoil.

Figure 2.6: Profiles of NACA 0012 and NACA 63-415 airfoil.

configuration is used. Depending on the shape of each airfoil (see Figure 2.6), near trailing edge, there might appear a favorite pressure gradient (FPG), that is to say, the pressure decreases along the surface in the flow direction. And for a FPG flow condition, the validity of Rozenberg's APG model has not been tested. This is the case for the NACA 63-415 airfoil on the pressure side. The skin friction coefficient is also plotted to examine if the flow separation is present. In XFOIL calculation, when a flow separation appears, the skin friction coefficient is zero. In the test cases, this situation did not happen for either of the airfoil type.

(a) Pressure coefficient C_p.

(b) Skin friction coefficient C_f.
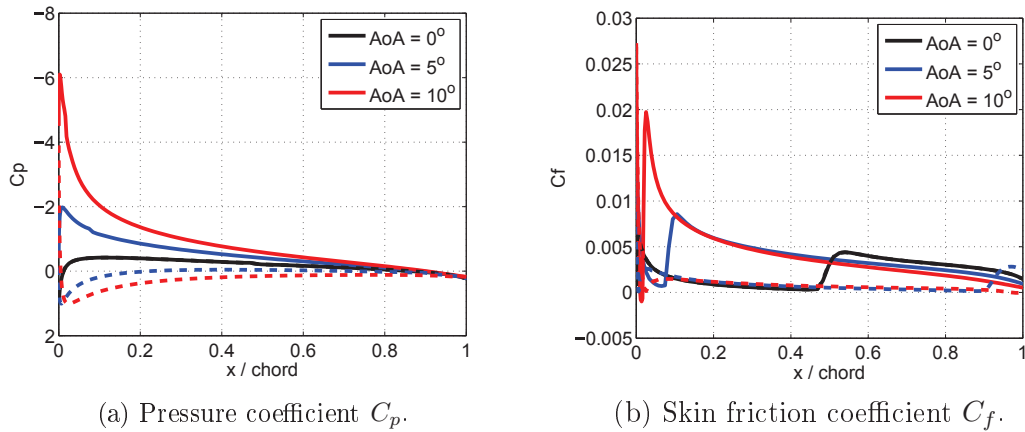
Figure 2.7: Pressure and skin friction coefficients for a NACA 0012 airfoil at a Reynolds number of $4 \cdot 10^6$. Solid lines: suction side; dashed lines: pressure side.

(a) Pressure coefficient C_p (b) Skin friction coefficient C_f
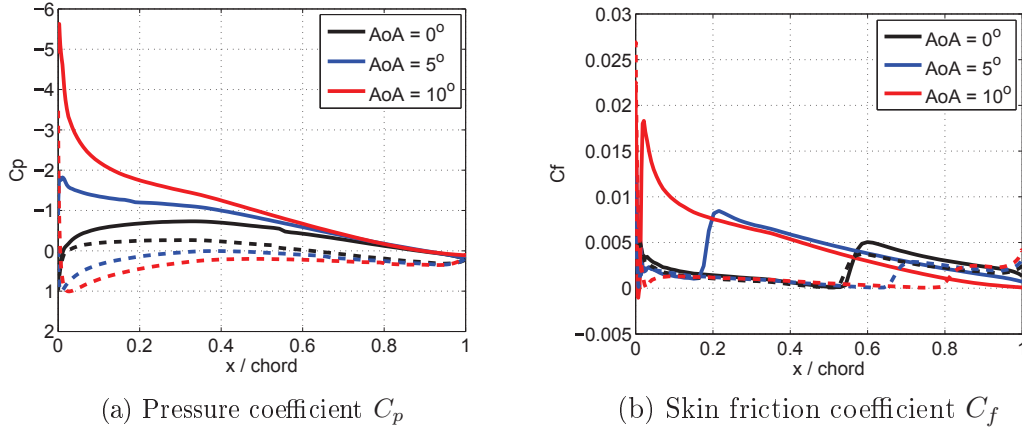
Figure 2.8: Pressure and skin friction coefficients for a NACA 63-415 airfoil at a Reynolds number of $4 \cdot 10^6$. Solid lines: suction side; dashed lines: pressure side.

2.1.3 Large aspect ratio assumption

In Section 2.1.1, the PSD of far field sound pressure level is obtained for exact formulation 2.35 and simplified formulation 2.37 under large aspect ratio assumption. The exact formulation involves sub-critical gusts as well as an integration over K_y during the calculation. If the aspect ratio is sufficiently large, it is expected that the simplified formulation can be used without losing accuracy.

A test case is performed for a fixed NACA0012 airfoil of chord $0.5\,m$. The span is chosen as $0.5\,m$, $1.5\,m$ and $2.5\,m$, so that the aspect ratio is 1, 3, and 5 respectively. The test velocity is $80\,\mathrm{m/s}$. Rozenberg's APG model is used for Φ_{pp}. Far field SPL is calculated by both exact and simplified formulations. The observer is $2\,m$ above the airfoil in the mid-span plane. The results are shown in Figure 2.9. As the aspect ratio increases, the sinc^2 function behaves more like a Delta function. When L/c is greater than 3, the simplified formulation gives almost identical results as the exact formulation over the whole frequency range, which confirms Moreau and Roger's conclusions [61]. Also, under large aspect ratio assumption, we have $\bar{K}_y = \bar{k}x_2/S_0$, thus

$$
\begin{aligned}
\bar{\kappa}^2 &= \bar{\mu}^2 - \frac{\bar{K}_y^2}{\beta_0^2} \\
&= \frac{\bar{k}^2 M^2}{\beta_0^4} - \frac{\bar{k}^2 x_2^2}{\beta_0^2 S_0^2} = \frac{\bar{k}^2}{\beta_0^2}\left(\frac{1}{\beta_0^2} - \frac{x_2^2}{S_0^2}\right).
\end{aligned} \tag{2.48}
$$

Since $1/\beta_0^2$ is always greater than 1, while x_2^2/S_0^2 is always smaller than 1, the result of $\bar{\kappa}$ is always greater than zero. Therefore, when large aspect ratio assumption applies, there will be no sub-critical gusts occur during the calculations.

(a-1) SPL for L/c = 1   (a-2) sinc^2 function

(b-1) SPL for L/c = 3   (b-2) sinc^2 function

(c-1) SPL for L/c = 5   (c-2) sinc^2 function
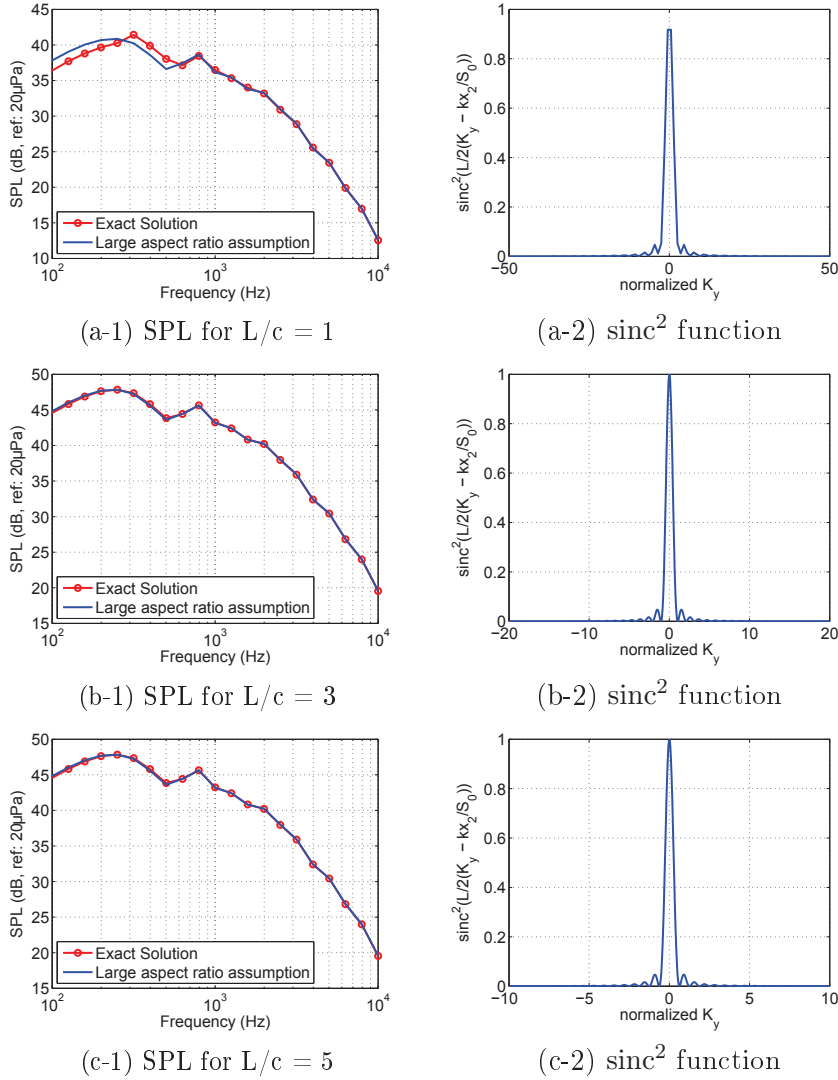
Figure 2.9: SPL by exact and simplified formula for NACA 0012 airfoils with different aspect ratio.

When using the exact solution, it is still needed to verify the contribution of sub-critical gusts. A prediction using the exact solution is performed using a plate with a span of $1\,m$, and a chord of $1\,m$ or $0.33\,m$. The flow velocity is $80\,m/s$, and the receiver is $2\,m$ away from the plate mid-span. The SPL of trailing edge noise is calculated for these two chords, considering super-critical gusts contributions only, sub-critical gusts contributions only, and both contributions, as shown in Figure 2.10. We can see that sub-critical gusts dominate mainly at really low frequencies (below $100\,Hz$). When the aspect ratio is relatively large, it is acceptable to omit the sub-critical gusts at sufficiently high frequencies.

(a) Chord $= 1\,m$. (b) Chord $= 0.33\,m$.
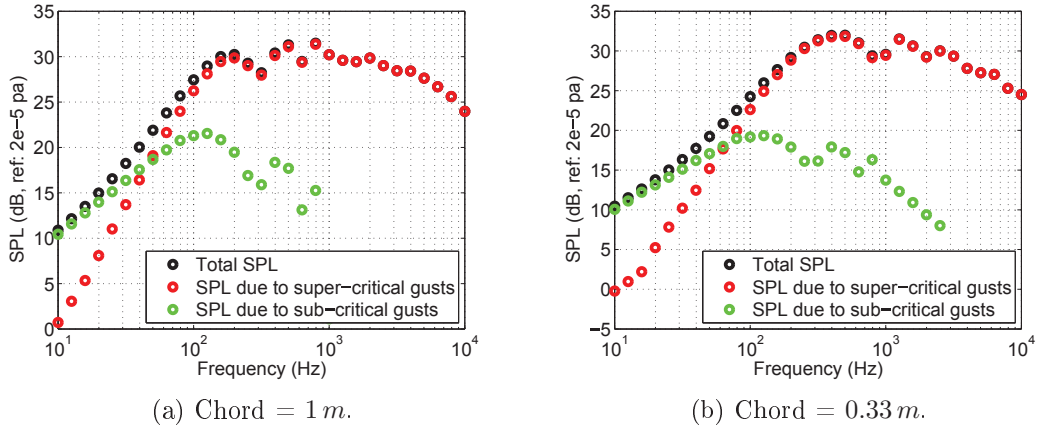
Figure 2.10: SPL prediction with exact solution for trailing edge noise. Super/sub-critical gusts are shown separately.

2.1.4 Model validations with fixed airfoil

2.1.4.1 Wall pressure fluctuation and SPL spectrum validation against measurements

To validate the effect of adverse pressure gradient on the noise generation, the wall pressure fluctuation model is compared with Goody's ZPG model against the data from Brooks and Hodgson [71] for a NACA 0012 airfoil and from Kamruzzaman [12] for a NACA 63-415 airfoil. A factor of 4π needs to be included when comparing wall pressure and SPL spectra with measurements. As reminded by Paterson and Amiet [13], a factor of 2 comes from the fact that the physically realizable one-sided PSD is defined for positive frequencies only, and a factor of 2π is accounted for in expressing results in terms of frequency f rather than the circular frequency ω.

In Brooks and Hodgson's work, a NACA 0012 airfoil of chord $0.61\,m$ and span $0.46\,m$ is placed in an anechoic quiet-flow facility. The test velocity is $69.5\,\mathrm{m/s}$. A series of surface pressure sensors are mounted on both sides of the airfoil surface inline with the chord. The last sensor is $1.854\,cm$ away from the trailing edge. Figure 2.11(a) compares the surface pressure fluctuation spectrum for APG and ZPG models to the measurements at the last sensor. In Figure 2.11(b), the comparison for SPL is presented for the same experimental settings. Microphones are placed in the mid-span $1.2\,m$ above the trailing edge. The APG model effectively increases the surface pressure spectrum levels at frequencies below $5\,\mathrm{kHz}$, thus the SPL spectrum, and the predicted results are closer to the measurements.

Kamruzzaman *et al.* [12] have performed surface pressure measurements on an asymmetric NACA 64$_3$-418 airfoil of chord 60 cm on both pressure and suction sides

(a)   (b)
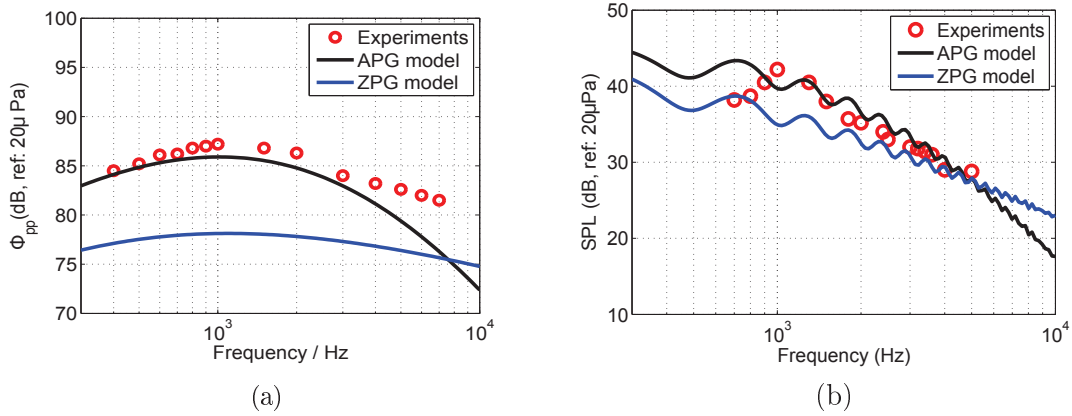
Figure 2.11: Comparison between APG model, Goody's ZPG model and measurements for a NACA0012 airfoil. (a) Wall pressure spectrum comparison; (b) Far field SPL comparison.

	$AoA = 0^o$		$AoA = 3^o$	
	$\delta^*(mm)$	$\theta^*(mm)$	$\delta^*(mm)$	$\theta^*(mm)$
Exp.	6.76	2.99	9.71	3.59
XFOIL	6.0	3.1	8.1	3.7

Table 2.2: Boundary layer parameters calculated by XFOIL and measured by Kamruzzaman *et al.* [12] at x/c = 0.995.

which permits us to study the spectrum on both sides of the airfoil. The inflow velocity is 62 m/s and the AoA is 0°. The boundary layer displacement thickness δ^* and momentum thickness θ^* calculated by XFOIL are compared to measured values in Table 2.2 (suction side only).

Figure 2.12 shows the pressure coefficient and skin friction coefficient on the airfoil surface at zero AoA. Both plots show that the adverse pressure only appears on the suction side while on the pressure side, a favorite pressure gradient is observed. This makes the application of APG model on the pressure side questionable. Here we will only apply the APG model on the suction side, and Goody's ZPG model will be used for the pressure side.

Associated wall pressure spectra are plotted in Figure 2.13(a). On the suction side, the predictions are much closer to the measurements using the APG model compared to the ZPG model, although the levels are still lower than the measured ones. Figure 2.13(b) compares the SPL spectrum predictions to the measurements. Using the APG model on the suction side and the Goody's ZPG model on the pressure side, a better agreement is found although the predictions still underestimate

(a)Cp   (b) Cf
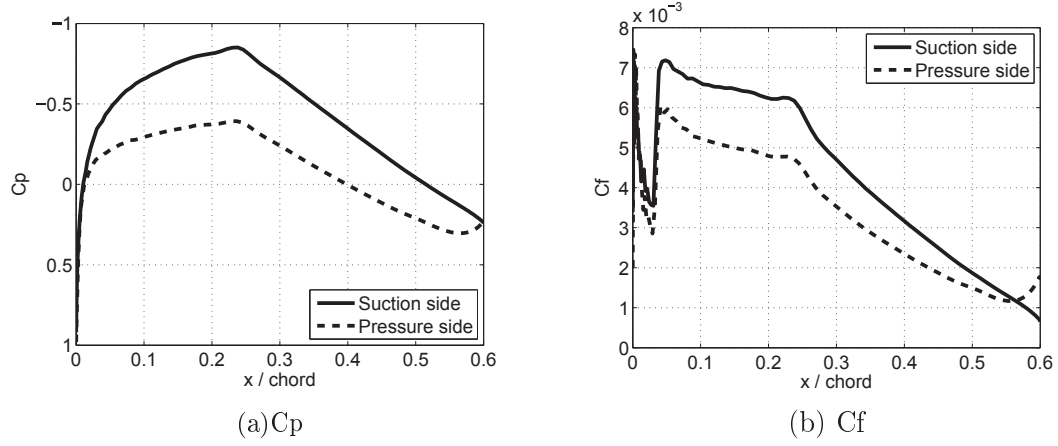
Figure 2.12: Pressure coefficient and skin friction coefficient for NACA64₃418 airfoil at zero AoA.

the measured values.

As a conclusion, it is clear that the adverse pressure gradient has an important effect on the SPL prediction, however its modeling is still an open issue in the aeroacoustics community.

(a)   (b)
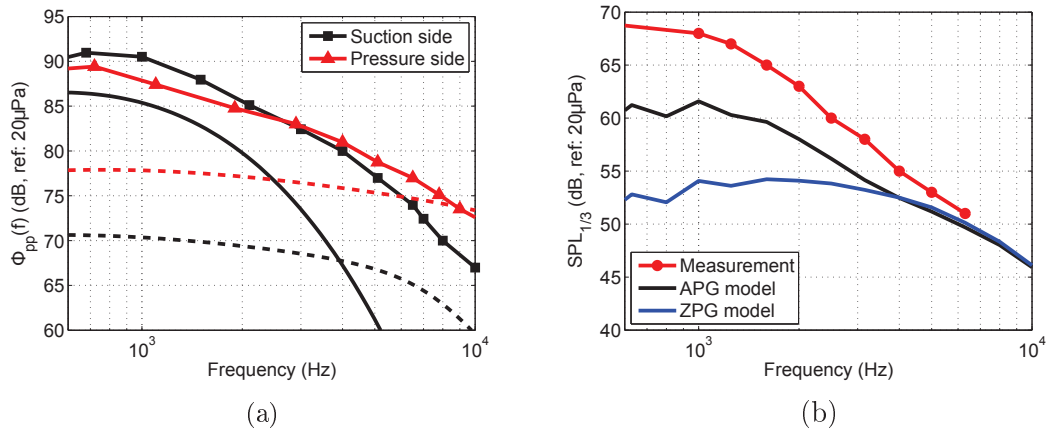
Figure 2.13: (a) Wall pressure spectra on the suction side (black lines) and on the pressure side (red lines) measured by Kamruzzaman *et al.* [12] (symbols) and predicted by APG (solid lines) and ZPG models (dashed lines) models. (b) Third octave band spectra of far-field SPL. Symbols: measurements; black line: APG model applied on suction side, and Goody's ZPG model on pressure side; blue line: ZPG model.

2.1.4.2   SPL comparison with semi-empirical model

Extensive measurements with NACA 0012 airfoil are performed by Brooks, Pope and Marcolini [1] (BPM report), providing us the possibility of validating Amiet's model for trailing edge noise. They proposed a semi-empirical model based on these measurements with fixed NACA 0012 airfoils. Thus their model requires many direct boundary layer parameters as input, such as boundary layer thickness δ^*, momentum thickness θ^*. The airfoils have various chord lengths, $0.1016\,m$, $0.1524\,m$, $0.2286\,m$, $0.3048\,m$. The span is $0.46\,m$, so only the airfoils with chords of $0.1016\,m$, $0.1524\,m$ fulfill the large aspect ratio criteria. Tested angles of attack (AoA) are from 0° to 12.6^o. Boundary layer parameter measurements are made at 0.64 mm from the trailing edge. Airfoils are tested with tripped and un-tripped surfaces. For tripped cases, the boundary layer transition from laminar to turbulence was achieved by a random distribution of grit in strips from the leading edge to 20% chord; while for un-tripped cases, the surfaces were smooth and clean, and free transition was expected. This transition location is realized by changing the *xtr* value in XFOIL, as explained in Section 2.1.2.2. Test velocities at free stream were up to 71.3m/s, corresponding to a Mach numbers up to 0.208, and a Reynolds numbers up to $1.5 \cdot 10^6$ for the largest chord.

In this BPM report, empirical expressions for $\delta, \delta^*, \theta^*$ for a NACA 0012 airfoil with sharp trailing edge are given for both tripped and un-tripped cases, and for both sides. All the expressions are obtained based on the experimental results (See Figures 6-8 in the report). XFOIL results for δ^* and θ^*, and estimation of δ from Equation (2.47) are compared with the empirical curves in Figure 2.14. We can see that the boundary layer thicknesses of the tripped case fit better with the empirical curves than those of the un-tripped case. This may be because for un-tripped cases, especially at low Reynolds, the boundary layer remains laminar till trailing edge, and thus it is thicker than the tripped case with the same Reynolds. The results for larger chords fit better than those for smaller chords, because it has larger Reynolds number for the same velocity. The case with $0.1524\,m$ chord fits the best among all chords for both δ^* and θ^*. Boundary layer thickness δ is in good agreement in the Reynolds range where δ^* and θ^* are well fitted, which means expression (2.47) can be used to calculated δ.

Boundary layer parameters as a function of AoA are plotted in Figure 2.15. Only the tripped case are shown for inflow velocities of $39.6\,m/s$ and $71.3\,m/s$. The fitting is better for pressure side than suction side. This may be due to the fact that on the suction side, there is a risk of flow detachment. Under this situation, XFOIL cannot provide correct results. For the pressure side, the boundary layer is less likely to detach, thus XFOIL results are more reliable.

For the SPL measurements, a microphone is placed $1.22\,m$ away from the airfoil trailing edge in the mid-span. Free stream velocity is $71.3\,m/s$ for all the cases.

(a) δ^*/c

(b) θ^*/c

(c) δ/c
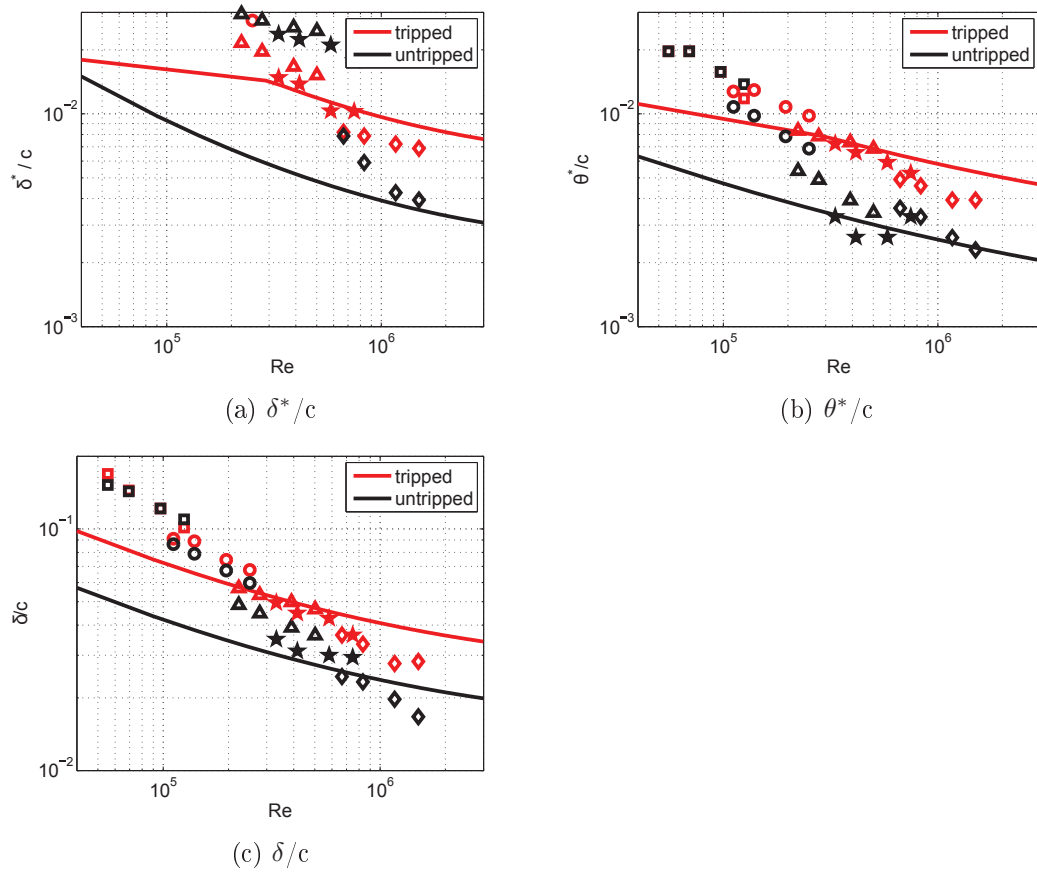
Figure 2.14: Boundary layer parameters calculated with XFOIL (symbols) comparing with empirical curves (lines) given by [1], AoA $= 0^o$. Symbols represent different chord length: $\diamond$, 0.3048m; $\star$, 0.1524m; $\triangle$, 0.1016m; $\bigcirc$, 0.0508; $\square$, 0.0254m.

(a) $U = 71.3 \ m/s$

(b) $U = 39.6 \ m/s$
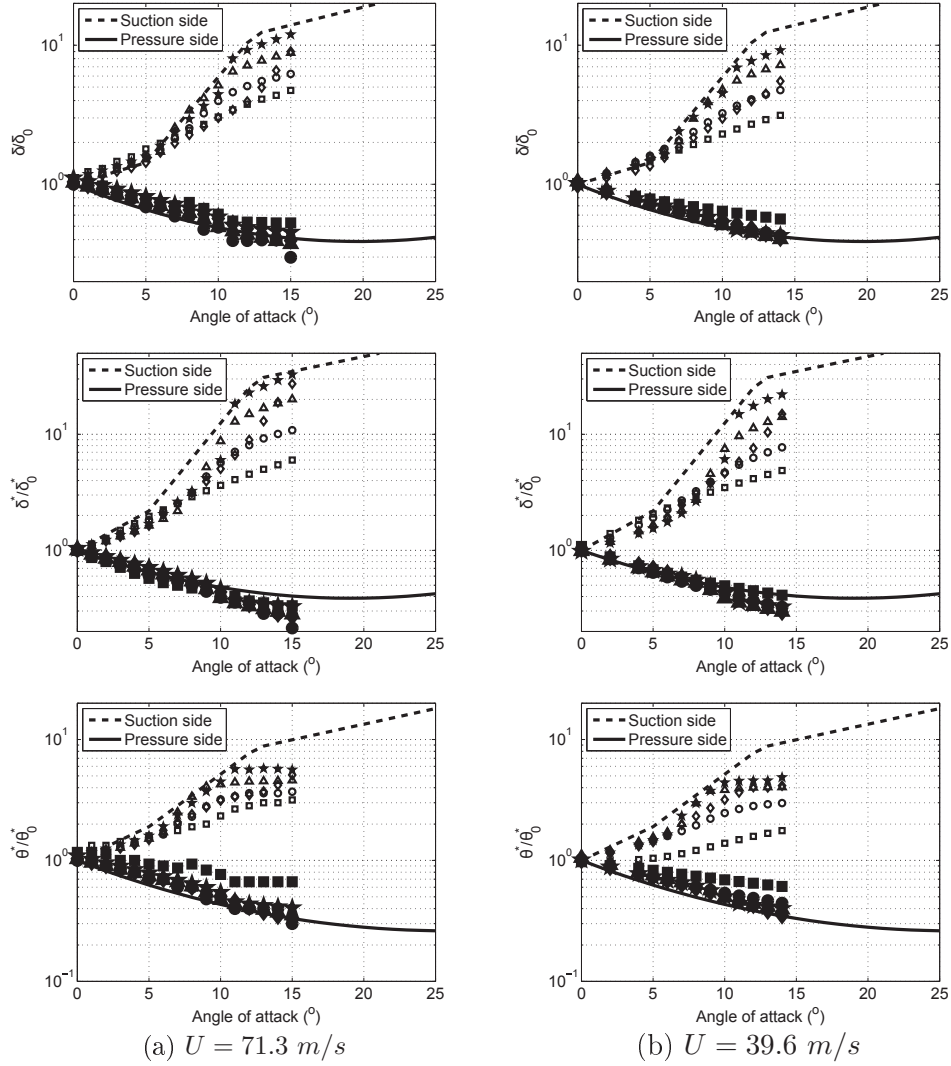
Figure 2.15: Comparison of δ^*, δ and θ^* calculated by XFOIL for tripped cases at various AoA. Symbol shapes are consistent with Figure 2.14. Empty symbols are for suction side, and filled symbols are for pressure side. Left column consists figures with free stream velocity $U = 71.3 \ m/s$, right column consists figures with free stream velocity $U = 39.6 \ m/s$. Subscription $_0$ stands for the corresponding terms at 0° AoA.

Results for chord of $0.1524\,m$ are shown with various AoAs in Figure 2.16. Markers are results from BPM semi-empirical model; lines are results from Amiet's model, with Goody's ZPG model (left column) and the APG model (right column) respectively. For a NACA 0012 airfoil, adverse pressure gradient appears on both side of the trailing edge, thus Goody's model underestimate the results. APG model gives relatively good results, especially in the lower frequency range, but over estimates the SPL at higher frequencies. However, using APG model, we can capture the phenomenon that TEN is dominant on the suction side, and the level is proportional to the displacement thickness, while the spectrum peak frequency is inversely proportional to the displacement thickness, as mentioned by Brooks and Hodgson [71]. For AoA greater than approximately 5°, separation noise become dominant according to BPM model. Separation noise is not accounted for in our model, which might underestimate the SPL at high AoA.

2.2 Amiet's theory for turbulent inflow noise

2.2.1 Derivation of Amiet's model for turbulent inflow noise

When a turbulent gust encounters an airfoil (or a plate), this fluctuating gust will cause a fluctuating lift (or fluctuating pressure) on the airfoil surface, which in turn, lead to the generation of sound. Amiet's analytical model for turbulent inflow noise [40] was proposed before trailing edge noise [41]. The procedure is similar as for trailing edge noise. First, the pressure fluctuation on the airfoil surface due to incoming gusts is determined. This is usually done in the Fourier domain by decomposing the incoming gusts in wave numbers. Then acoustic analogy is applied to obtain the far field pressure fluctuation. The last step consists of calculating the power spectral density of far field pressure fluctuations, to get the SPL spectrum at far field.

Induced surface pressure fluctuation

As for trailing edge noise, we first assume a flat plate with a semi-infinite chord. An illustration of the configuration is shown in Figure 2.17. The leading edge is aligned with y axis, flow is in x direction, and z is the direction normal to the plate surface. Incoming turbulence is convected by the mean flow U. We assume that during the convection, turbulence properties do not change (frozen turbulence). If we decompose the turbulent gust in the Fourier domain, we can express the gust in form

$$w = w_0 e^{i(\omega t - K_x x - K_y y)}, \tag{2.49}$$

where K_x and K_y are the chord-wise and span-wise wavenumber respectively. The velocity potential field ϕ imposed by w with is then

$$\phi(x, y, z, t) = \varphi(x, z) e^{i\omega t} e^{\frac{kM}{\beta_0^2} ix} e^{-iK_y y}. \tag{2.50}$$

(a) Goody's model

(b) APG model

(c) Goody's model

(d) APG model

(e) Goody's model

(f) APG model

(g) Goody's model

(h) APG model
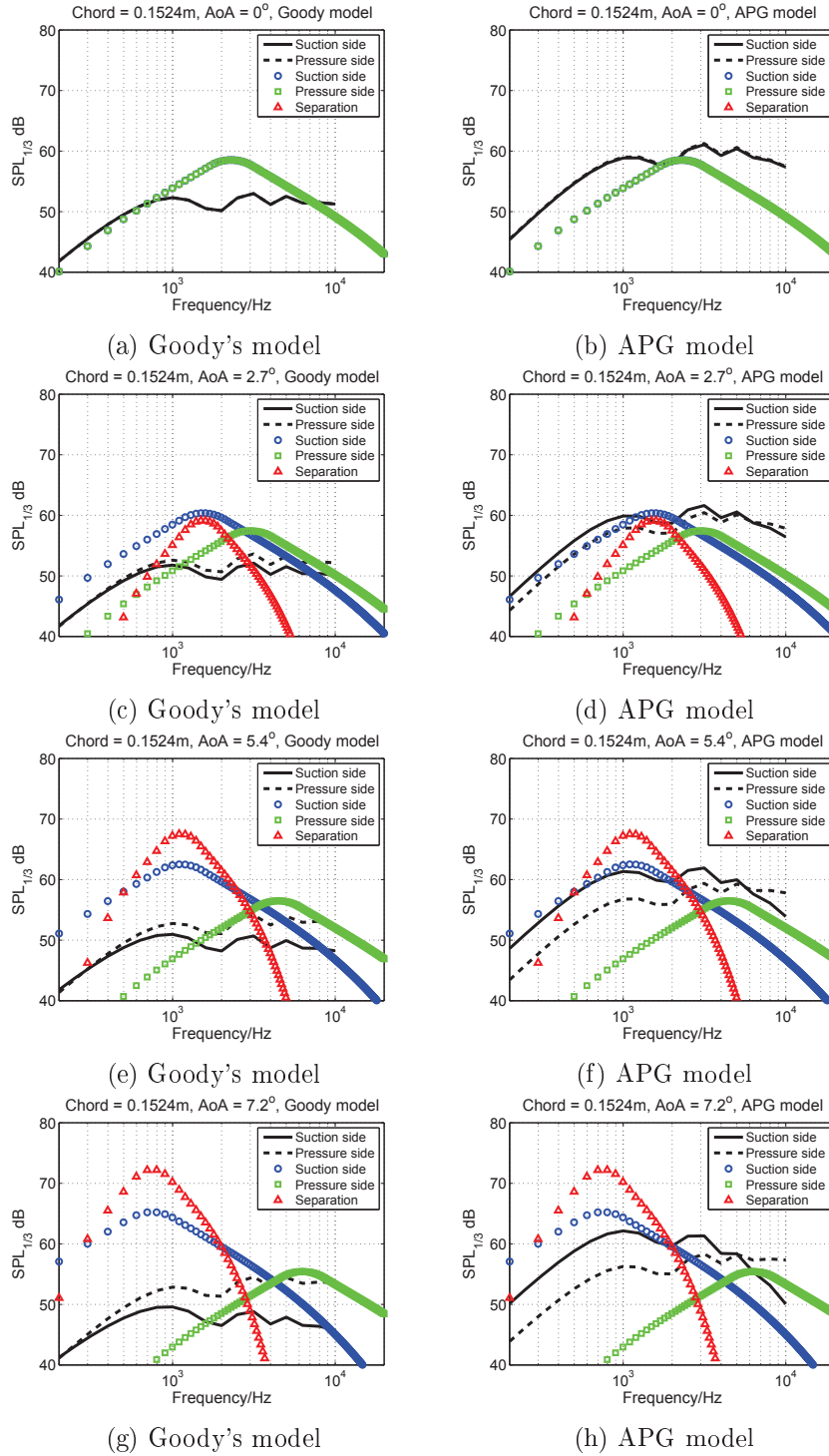
Figure 2.16: SPL predictions for chord $= 0.1524\,m$. Markers: BPM model; lines: Amiet's model.

Following the similar procedure as for trailing edge noise, we obtain the 3D Helmholtz equation in term of ϕ as:

$$\frac{\partial^2 \varphi}{\partial \bar{x}^2} + \frac{\partial^2 \varphi}{\partial \bar{z}^2} + \bar{\kappa}^2 \varphi = 0, \tag{2.51}$$

where $\bar{\kappa}$ has the same expression as in Section 2.1.1, replacing K_c by K_x. The main term of induced surface pressure is linked with the velocity potential ϕ, thus it can be calculated after solving equation (2.51) for ϕ:

$$p_1(x, y, 0, t) = \rho_0 w_0 U \frac{e^{-i\pi/4}}{\sqrt{\pi(\beta_0^2 \bar{\kappa} + K_x b)\bar{x}}} e^{i(\omega t + (\bar{K}_x M^2/\beta_0^2 - \bar{\kappa})\bar{x} - K_y y)}. \tag{2.52}$$

The trailing edge correction term (corresponds to leading edge correction term for trailing edge noise) is given in Appendix A
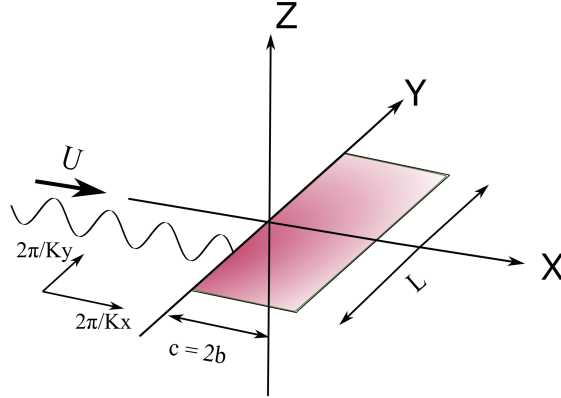
Figure 2.17: 3D geometry for turbulent inflow noise.

Far-field pressure fluctuation calculation

The induced pressure field distribution is linked to the far field sound pressure level. According to equation (2.18), the integrated surface pressure is written as:

$$\tilde{p}(\vec{x}, \omega) = \int \frac{i\omega R_3}{4\pi c_0 R_s^2} \tilde{l}(\vec{y}, t) e^{-i\omega R_t/c_0} \, dS_y. \tag{2.53}$$

The incoming incident turbulence considering the convective velocity can be written in wave number form as:

$$w(y_1, y_2, t) = \hat{\hat{w}}(K_x, K_y) e^{i[-iK_x(y_1 - Ut) - K_y y_2]}, \tag{2.54}$$

where $\hat{\hat{w}}(K_x, K_y)$ is the 2D spatial Fourier transform of $w(y_1, y_2, t)$. The local lift force is equal to the pressure jump, thus it can be expressed as:

$$
\begin{aligned}
l'(y_1, y_2, t) = \Delta P(y_1, y_2, t) &= 2\pi\rho_0 U w(y_1, y_2, t) g(y_1, y_2, t) \\
&= 2\pi\rho_0 U \hat{w}(K_x, K_y) g(y_1, K_x, K_y) e^{i[-K_x(y_1 - Ut) - K_y y_2]},
\end{aligned}
\tag{2.55}
$$

where $g(y_1, K_x, K_y)$ is the airfoil transfer function for turbulent inflow noise, linking the incident turbulent gusts and the far field acoustic pressure. The Equation (2.55) gives the lift force due to a single incident gust. By integrating over all wave numbers, we get the total lift force at the point (y_1, y_2):

$$
\begin{aligned}
l(y_1, y_2, t) &= \iint\limits_{-\infty}^{\infty} l'(y_1, y_2, t) dK_x \, dK_y \\
&= 2\pi\rho_0 U \iint\limits_{-\infty}^{\infty} \hat{w}(K_x, K_y) g(y_1, K_x, K_y) e^{i[-K_x(y_1 - Ut) - K_y y_2]} dK_x \, dK_y.
\end{aligned}
\tag{2.56}
$$

The time domain Fourier transform of Equation (2.56) leads to:

$$
\tilde{l}(\vec{y}, \omega) = 2\pi\rho_0 \iint\limits_{-\infty}^{\infty} \hat{w}(K_x, K_y) g(y_1, K_x, K_y) e^{-iK_y y_2} \left(\frac{U}{2\pi} \int_{-\infty}^{\infty} e^{i(K_x U - \omega)t} dt \right) dK_x \, dK_y.
\tag{2.57}
$$

Applying Dirac function:

$$
\int_{-\infty}^{\infty} e^{i(K_x U - \omega)t} dt = \frac{2\pi}{U} \delta(K_x U - \omega),
\tag{2.58}
$$

we can simplify equation (2.57) as:

$$
\tilde{l}(\vec{y}, \omega) = 2\pi\rho_0 \int_{-\infty}^{\infty} \hat{w}\left(\frac{\omega}{U}, K_y \right) g\left(y_1, \frac{\omega}{U}, K_y \right) e^{-iK_y y_2} dK_y.
\tag{2.59}
$$

Far field spectrum of sound pressure level calculation

We then introduce the cross power spectra density (cross-PSD) in statistical variables S_{ll} for the local lift as:

$$
\begin{aligned}
&S_{ll}(\vec{y}, \vec{y}', \omega) \\
&= (2\pi\rho_0)^2 \iint \hat{w}(\frac{\omega}{U}, K_y) \hat{w}^*(\frac{\omega}{U}, K_y') g(y_1, \frac{\omega}{U}, K_y) g^*(y_1', \frac{\omega}{U}, K_y') e^{-i(K_y y_2 - K_y y_2')} dK_y dK_y'.
\end{aligned}
\tag{2.60}
$$

Due to the statistical orthogonality of the wave vectors, it is shown that [72]:

$$\hat{w}\left(\frac{\omega}{U}, K_y\right)\hat{w}^*\left(\frac{\omega}{U}, K_y'\right) = U\delta(K_y - K_y')\Phi_{ww}\left(\frac{\omega}{U}, K_y\right), \qquad (2.61)$$

where Φ_{ww} is the 2D turbulence energy spectrum. Now introducing equation (2.61) into (2.60), we get the cross-PSD as:

$$S_{ll}(\vec{y}, \vec{y}', \omega) = (2\pi\rho_0)^2 U \int_{-\infty}^{\infty} \Phi_{ww}\left(\frac{\omega}{U}, K_y\right) g\left(y_1, \frac{\omega}{U}, K_y\right) g^*\left(y_1', \frac{\omega}{U}, K_y'\right) e^{-iK_y(y_2 - y_2')} dK_y. \qquad (2.62)$$

Recall equation (2.53) for the acoustic pressure at far field, we can derive the far field PSD as [73]:

$$S_{pp}(\vec{x}, \omega) = \tilde{p} \cdot \tilde{p}^* = \iint \left(\frac{\omega R_3}{4\pi c_0 R_s^2}\right)^2 S_{ll}(\vec{y}, \vec{y}', \omega) e^{-i\omega(R_t - R_t')/c_0} dSy dSy'$$

$$= \left(\frac{\rho_0 \omega R_3}{2c_0 R_s^2}\right)^2 U \iint e^{-i\omega(R_t - R_t')/c_0}$$

$$\int_{-\infty}^{\infty} \Phi_{ww}\left(\frac{\omega}{U}, K_y\right) g\left(y_1, \frac{\omega}{U}, K_y\right) g^*\left(y_1', \frac{\omega}{U}, K_y'\right) e^{-iK_y(y_2 - y_2')} dK_y dSy dSy'. \qquad (2.63)$$

The distance R_t between the retarded source location and the observer is defined by Equation (2.24), thus the term $R_t - R_t'$ can be approximated as:

$$R_t - R_t' = \frac{R_s - M_x(x_1 - y_1)}{\beta_0^2} - \frac{R_s' - M_x(x_1 - y_1')}{\beta_0^2}$$

$$\approx \frac{(y_1' - y_1)(x_1 - S_0 M_x) + \beta_0^2 x_2(y_2' - y_2)}{\beta_0^2 S_0}. \qquad (2.64)$$

Substituting it into equation (2.63), and using the same geometric approximations as in Section 2.1.1, we get:

$$S_{pp}(\vec{x}, \omega) = \left(\frac{\rho_0 \omega x_3}{2c_0 S_0^2}\right)^2 U \iint e^{-\frac{i\omega}{c_0 S_0 \beta_0^2}(y_1' - y_1)(x_1 - S_0 M_x) + \beta_0^2 x_2(y_2' - y_2)}.$$

$$\int_{-\infty}^{\infty} \Phi_{ww}(\frac{\omega}{U}, K_y) g(y_1, K_x, K_y) g^*(y_1', K_x, K_y') e^{-iK_y(y_2 - y_2')} dK_y dSy dSy', \qquad (2.65)$$

where $dSy = dy_1 dy_2$ and $dSy' = dy_1' dy_2'$. Detailed calculations can be found in [73, 74]. The far field SPL S_{pp} is finally expressed by the airfoil transfer function for turbulent inflow noise $\mathscr{L}$:

$$S_{pp}(\vec{x}, \omega) = \left(\frac{\rho_0 \omega c x_3}{2c_0 S_0^2}\right)^2 U \int_{-\infty}^{\infty} \Phi_{ww}(\frac{\omega}{U}, K_y)\mathscr{L}^2\left(x_1, \frac{\omega}{U}, K_y\right) \text{sinc}^2\left[\frac{L}{2}\left(\frac{kx_2}{S_0} - K_y\right)\right] dK_y. \qquad (2.66)$$

If the aspect ratio L/c is large enough, we can express the $\text{sinc}^2(x)$ function by a Delta function, and then the PSD of turbulent inflow noise at far field is reduced as

$$S_{pp}(\vec{x}, \omega) = \left(\frac{\rho_0 \omega c x_3}{2 c_0 S_0^2}\right)^2 \pi U \frac{L}{2} \Phi_{ww}\left(\frac{\omega}{U}, \frac{k x_2}{S_0}\right) \left|\mathscr{L}\left(x_1, \frac{\omega}{U}, \frac{k x_2}{S_0}\right)\right|^2. \qquad (2.67)$$

For the super-critical case, the expression for the first-order term of the airfoil transfer function is written as:

$$\mathscr{L}_1(\vec{x}_i, K_x, K_y) = \frac{1}{\pi} \sqrt{\frac{2}{(\beta_0^2 \bar{\kappa} + \bar{K}_x) \cdot \Theta_1}} E^*[2\Theta_1] e^{i\Theta_2}. \qquad (2.68)$$

As in the trailing edge noise model, we neglect the second-order back-scattering correction because it is small for the chord and frequencies considered in the study. For the sub-critical case, the expression for the airfoil transfer function is given in Appendix A.

Von Kármán spectrum for isotropic turbulence

Φ_{ww} that appears in Equation (2.67) is the 2D energy spectrum of vertical velocity fluctuation for isotropic turbulence. We used the Von Kármán spectrum model, thus the spectrum is given in the form:

$$\Phi_{ww}(K_x, K_y) = \frac{4}{9\pi} \frac{\bar{\sigma}_u^2}{K_e^2} \frac{\hat{K}_x^2 + \hat{K}_y^2}{(1 + \hat{K}_x^2 + \hat{K}_y^2)^{7/3}}, \qquad (2.69)$$

where $\hat{K} = K/K_e$ and $K_e = \frac{\sqrt{\pi}}{\Lambda} \frac{\Gamma(5/6)}{\Gamma(1/3)} \simeq 0.747/\Lambda$, with Λ the turbulence integral length scale, and σ_u is the root-mean-square of turbulent velocity fluctuations.

2.2.2 Airfoil thickness correction for turbulent inflow noise

In the report of Paterson and Amiet [13], it is observed that for the turbulent inflow noise, there is a great discrepancy between the measured far field SPL and the prediction. This discrepancy becomes larger at high frequency and low Mach number. They attribute this discrepancy to the fact that the thickness of the airfoil is not taken into account by the model (because of the thin flat plate assumption). Recently, Devenport [14], Roger and Moreau [75] showed that turbulent inflow noise is almost independent of AoA for a symmetric airfoil such as a NACA 0012 profile. However, it is subject to the airfoil thickness, especially for the incoming turbulence with eddy size that is comparable with the airfoil thickness. The thickness of a airfoil tends to reduce the turbulent inflow noise level. We propose here an empirical correction based on the data shown in Figure 6 of Roger and Moreau's publication [75]. The reduction level in dB due to airfoil thickness is calculated by linear interpolation based on these data:

$$SPL_R(dB) = 9/50 \cdot (e/c)/(e/c)_{ref} \cdot f/U \cdot (\Lambda/c)_{ref}/(\Lambda/c), \qquad (2.70)$$

where e is the airfoil maximum thickness, and Λ is the turbulent integral length scale. The subscription $_{ref}$ stands for the value of reference experimental data from a NACA 0012 airfoil, which is: $(e/f)_{ref} = 0.12$, and $(\Lambda/c) \approx 0.1$.

2.2.3 Sound pressure level comparison with fixed airfoil

Amiet's model for turbulent inflow noise is validated in this section for symmetric and asymmetric airfoils respectively. The experimental data for a NACA 0012 airfoil from Paterson and Amiet [13] and a NACA 0015 airfoil from Devenport *et al.* [14] are chosen for the symmetric airfoil validations. The data for a S831 airfoil from Devenport *et al.* [14] are chosen for the asymmetric airfoil validations.

2.2.3.1 Turbulent inflow noise validations for symmetric airfoils

The first validation for a NACA 0012 airfoil with thickness correction is shown in Figure 2.18. The measurements are from Paterson and Amiet [13] for a NACA 0012 of chord 23 cm. Test Mach numbers are between 0.12 and 0.5. The turbulence intensity is around 4 to 5 percent, and the longitudinal integral length scale is $0.03\,m$. Airfoil maximum thickness is 12% of the chord. The agreement between model and measurements is greatly improved when the thickness correction is considered, which is expected since this set of data was used to obtain Equation (2.70). We can also see that the SPL reduction due to the thickness correction is more pronounced at high frequencies and low Mach number.
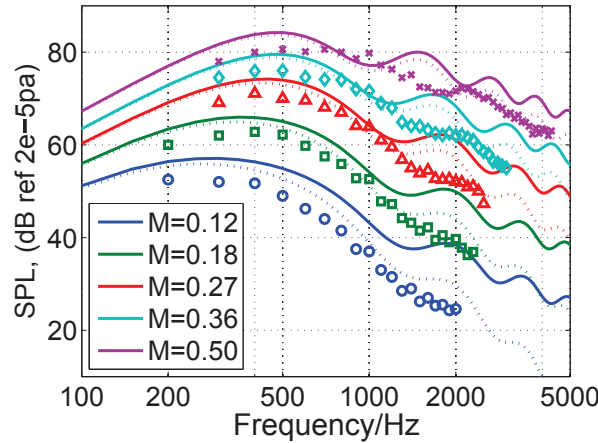
Figure 2.18: Turbulent inflow noise with thickness correction for a NACA0012 airfoil. Symbols: measurements from [13]; solid lines: Amiet's turbulent inflow noise model without thickness correction; dashed lines: Amiet's turbulent inflow noise model with thickness correction.
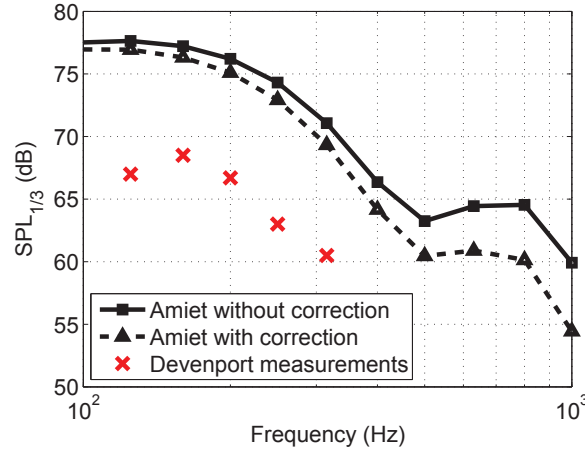
Figure 2.19: SPL comparison for a NACA 0015 airfoil. Measurments from [14].

The second validation for a symmetric airfoil is against measurements from Devenport *et al.* [14]. Experiments are performed in a wind tunnel at a Mach number of 0.08. A biplanar rectangular grid is placed in the contraction part of the tunnel. The turbulence property measurements confirm a von Kármán spectrum whose longitudinal integral length is $82\,mm$, and turbulence density is $3.9\,\%$ at flow velocity of $30\,m/s$. The microphone is placed $1.8\,m$ above the leading edge of the airfoil in the mid-span plane for the noise measurement. The span of the tested NACA 0015 airfoil is $1.83\,m$, and the chord is $0.61\,m$. Figure 2.19 shows that Amiet's model overestimates the measured SPL. With thickness correction. The results are little better comparing to the measurements, however, the overestimation is still up to 10dB. We need to note that the thickness correction does not include airfoil curvature, which might be a source of overestimation.

2.2.3.2   Turbulent inflow noise validations for asymmetric airfoils

Measurements from Devenport *et al.* [14] for a S831 are considered in this section. Wind tunnel and experimental setups are identical as explained in previous section for NACA 0015 airfoil. The test airfoil has a span of $1.83\,m$ and the chord of $0.914\,m$. SPL prediction with and without thickness correction are compared with the measurements in Figure 2.20, at angle of attack of 0° and 2°. The thickness correction slightly improves the agreement between predictions and measurements, but it not sufficient to provide a satisfying agreement below $200\,Hz$. This discrepancy can be attributed to AoA, curvature and camber effects. As noted by Devenport *et al.* [14], turbulent inflow noise is almost independent of AoA for symmetric airfoils, but is influenced by the airfoil geometry for the S831. This is clear seen in the predictions of Devenport *et al.* [14] for AoA between 0° and 4°, reproduced in Figure 2.20. These predictions are based on a panel method described in [76] that exactly accounts for the airfoil geometry. Figure 2.20 shows that these predictions correctly capture the

thickness effect, and that the effect of AoA is significant, with a decrease of about $4\,dB$ between 0° and 4°. Even though Amiet's predictions tend to overestimate the noise levels in this case, one must keep in mind that the Mach number is very small in this experiment, thus the discrepancy seen in Figure 2.20 can be considered as the worst scenario for wind turbine blades.
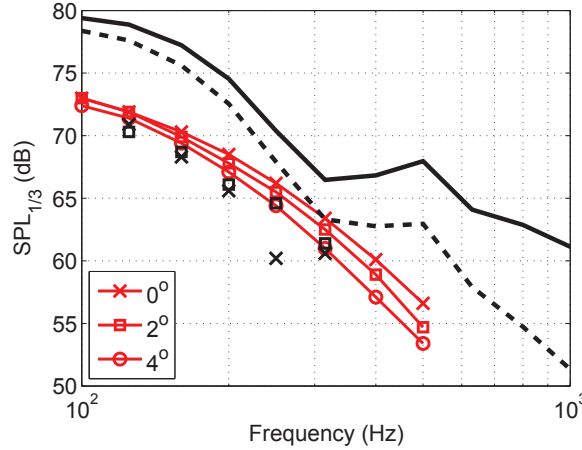
Figure 2.20: Turbulent inflow noise with (black dashed lines) and without (black solid lines) thickness correction for a S831 airfoil. The results are compared to the measurements (black symbols) and predictions (red lines) of Devenport *et al.* [14] for AoA of 0°, 2° and 4°.

2.3 Conclusions

In this chapter, Amiet's analytical model for trailing edge noise and turbulent inflow noise have been presented in details. Pressure fluctuation in the far field is related to the surface pressure jump by airfoil transfer functions. The power spectral densities of SPL for the two noise mechanisms are obtained using statistical methods. The expressions can be simplified if the airfoil geometry satisfies the large aspect ratio assumption, with a greatly reduced computation time without losing accuracy.

The trailing edge noise theory requires surface pressure fluctuation spectrum as an important input data. A wall pressure spectrum model that considers an adverse pressure gradient (APG) flow proposed by Rozenberg *et al.* is examined in this chapter as an improvement to the original Goody's expression for zero pressure gradient (ZPG) flow. The results show that the APG model greatly improves the predictions. However, more accurate and efficient predictions, such as the ones obtained with the modified TNO-Blake model, are desired and are currently under study in the aeroacoustics community.

For turbulent inflow noise, Devenport *et al.* and Roger & Moreau showed that the level is independent of angle of attack for a symmetric profile, but is influenced by the airfoil thickness. According to experiments, a thicker airfoil radiates less noise. The reduced level is related to the turbulence integral length scale, as well as the thickness of the airfoil itself. An empirical correction by Roger and Moreau is used in this chapter to take into account this effect. Validations for this thickness correction are performed against measurements for both symmetric and asymmetric airfoils. The results show that the correction is able to reflect the trend of reduction with respect to the flow Mach number and frequency. However, the reduction level is not enough to bring the prediction levels down to the measurements especially for an asymmetric airfoil. This indicates that camber effect and airfoil geometry have influences on the turbulent inflow noise, also, other turbulence parameters might need to be used in the empirical correction.

Noise prediction for a full size wind turbine in free field

Contents

3.1 Introduction

Amiet's analytical models for trailing edge noise and turbulent inflow noise presented in Chapter 2 are applied to wind turbine noise prediction in this chapter. The original models are based on a fixed flat plate, thus it requires an adaptation to a rotating airfoil. The blade is divided into shorter segments to better describe the variation of the flow conditions along the blade, and then the logarithm summation is performed over all the segments to get the total noise level. It is also possible to deduce the noise directivity and to study its amplitude modulations. Furthermore, the effect of wind shear can be examined since the wind speed profile is taken as an input parameter. Amiet's source model assumes propagation in free field conditions. However, we will see in the next chapter that it can be coupled to a propagation model to take into account ground and refraction effects.

First the wind turbine aerodynamics is studied using the blade element momentum theory in Section 3.2. Then, the adaptation to a $2.3MW$ wind turbine with

rotating blades will be explained in Section 3.3, considering Doppler effect, blade division and the coordinate transfer. In the same section, studies on atmospheric conditions, namely wind shear and atmospheric turbulence, are also presented, in order to obtain suitable input parameters for the noise models. In section 3.4, results on SPL, directivity, amplitude modulation, as well as the effects of wind shear and atmospheric turbulence are examined in detail.

3.2 Aerodynamics of a wind turbine using blade element momentum theory

Blade element momentum theory (BEM) is the combination of blade element theory and momentum theory. It is one of the fundamental aerodynamic theory for rotating blades (wind turbine blade, propeller), and is used to calculate blade local forces, thrust, induced velocity, etc [77, 78]. If we consider an isolated stream flow passing through the rotor plane as shown in Figure 3.1, the flow is irrotational on the left side of the rotor, then gains angular momentum after passing through the rotor. Since for this isolated system, conservation laws must be obeyed, there must be an equal and opposite angular momentum imposed on the rotor blade. At the same time, the flow axial velocity changed after passing through the rotor because part of the energy is converted to rotating motion. We relate the change in axial velocity with an induction factor a, and the change in angular velocity of the rotor blade with a tangential induction factor a', see Figure 3.2. Using force balance and torque balance on the blade, we can obtain the expressions for a and a' as [77]:

$$a = \left(\frac{4\sin^2(i+\alpha)}{\sigma_a C_n} + 1 \right)^{-1} \tag{3.1}$$

and

$$a' = \left(\frac{4\sin(i+\alpha)cos(i+\alpha)}{\sigma_a C_t} - 1 \right)^{-1}, \tag{3.2}$$

where C_n, C_t are axial and tangential force coefficient respectively, related with lift and drag coefficients by

$$C_n = C_l \cos(\alpha) + C_d \sin(\alpha) \quad and \quad C_t = C_l \sin(\alpha) - C_d \cos(\alpha), \tag{3.3}$$

with α the angle of attack and i the angle between the rotor plane and the chordline (see Figure 3.2). σ_a is called the local solidity defined as: $\sigma_a = B_n c/2\pi r$ with B_n the number of the blades, and r the distance from a blade section to the rotor.

BEM method is important for wind turbine operations; it can be used in blade design, power output calculation and performance optimization. From an acoustic point of view, it is of most interest to know the induction factor a and a', since they modify the AoA at the leading edge of the blade. An iterative procedure by assuming $a = a' = 0$ at beginning is usually used to obtain converged value of a and a' [77, 78]. Other input parameters are chord length, blade twist, local lift and
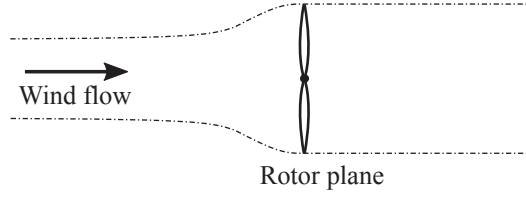
Figure 3.1: Free flow passing through the rotor plane.
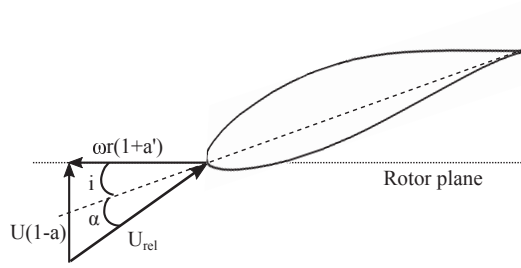
Figure 3.2: Induced velocity in the rotor plane.

drag coefficients. Prandtl's tip loss factor is also considered to correct the infinite number of blades assumption [77].

BEM method is now applied for a test case of a 5MW wind turbine. This wind turbine is used in assessing offshore wind technology by NREL [15]. The advantages of this reference is that blade twist and chord variations along the blade is given in their report, which is not often the case for commercial wind turbines. This specific upwind 3-blade wind turbine has a tower height of $90\,m$, rotor diameter of $126\,m$, rated speed of $11.4\,m/s$, and rotor speed of $12.1\,rpm$. In their study, each blade is divided in strips in order to describe the airfoil shape variations. The airfoil profile changes along the blade: near the root, a cylinder cross-section is used, then the profiles change to DU40, DU35, DU30, DU25, DU21, where 'DU' stands for 'Delft University'. The last 1/3 of the blade till the tip, a NACA 64 profile is used. It is not specified in their report which type of NACA 64*** airfoil is used near the tip region. However, the lift and drag coefficients, shown in Figure 3.3 are similar to those of a NACA 63-415 airfoil that will be used in the rest of this chapter.

Figure 3.4 shows the angle of attack calculated by BEM theory, that is, after considering induced velocity change, in both axial and tangential directions. We can see that near the tip region, the AoA is approximately 5°, which is the angle where C_l/C_d reaches the maximum for the NACA 64 airfoil, see Figure 3.5. The dashed line in Figure 3.4 stands for the AoA where no BEM method is used. It is simply calculated by $\alpha = \tan(U/\omega r)$, corresponding to $a = a' = 0$. We can see that the BEM method reduces the AoA by up to 3° near the tip region. This reduction of AoA can have an influence on the boundary layer parameter calculations when applying wall
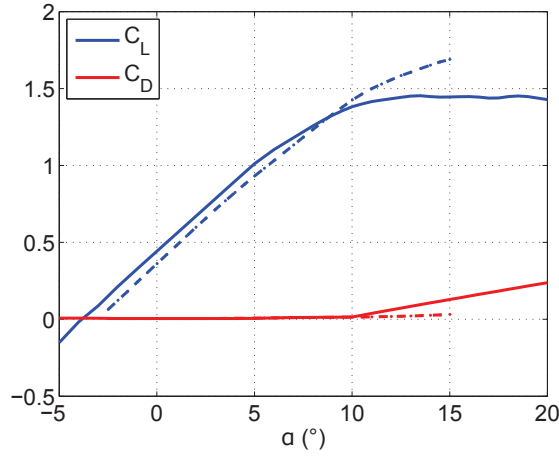
Figure 3.3: Comparison of lift and drag coefficients for the NACA 64 airfoil (dash-dotted line) used in [15] and the NACA 63-415 airfoil (solid line).

pressure fluctuation spectrum model, as we have shown in Section 2.1.2. Converged values of induction factors a and a' as a function of distance to the rotor center are shown in Figure 3.6, from where we can see that the angular induction factor is very small along the blade, while axial induction factor is more important in the point of view of changing the AoA. It is needed to point out that when the axial induction factor becomes larger than approximately 0.4, an empirical correction for induction factors should be applied [77]. We did not apply this correction, although it would be needed for the tip segment.

We compared our BEM results with the results of FAST version 8.12 that is developed by NREL (National Renewable energy laboratory). As seen in Figure 3.4, the AoA predictions are similar except close to the tip. Also, Figure 3.6 shows that FAST predicts a more realistic axial induction factor that remains close to 0.2 along most of the blade segments.

To apply BEM theory on a wind turbine, it is necessary to have the knowledge of the blade twist. However, this information is usually not available for commercial wind turbines, so BEM theory will not be applied hereafter. Instead, the optimal AoA is set as a constant along a blade corresponding to the value where C_l/C_d reaches the maximum as we saw from Figures 3.4 and 3.5.

3.3   Application of Amiet's model to a 2.3MW wind turbine

Schlinker and Amiet [62] applied Amiet's model to a helicopter rotor to predict the noise generation. In this section, the preparation work for applying Amiet's model
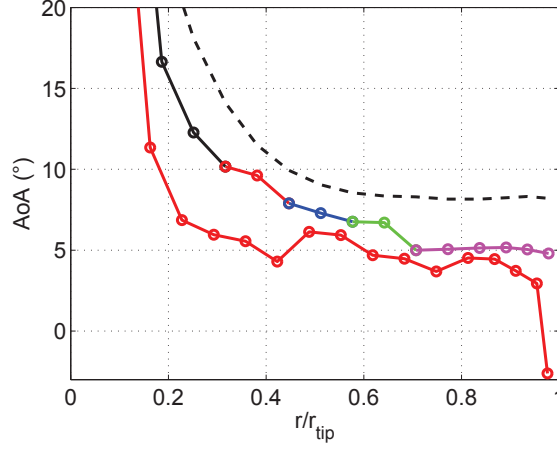
Figure 3.4: Angle of attack along the blade of the 5MW wind turbine calculated by BEM theory. Black dash line: induced velocity is not considered ($a = a' = 0$); color line: induced velocity is considered, and colors corresponds to different profile sections as shown in Figure 3.5; red line: induced velocity is considered and predicted by FAST. Tip loss factor is considered.
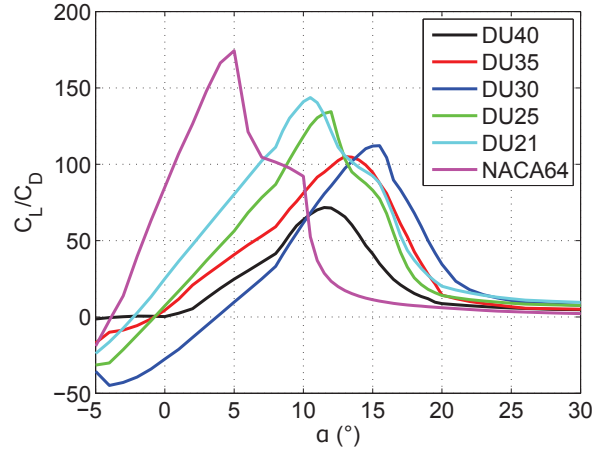
Figure 3.5: C_l/C_d for all the blade sections mentioned in [15].
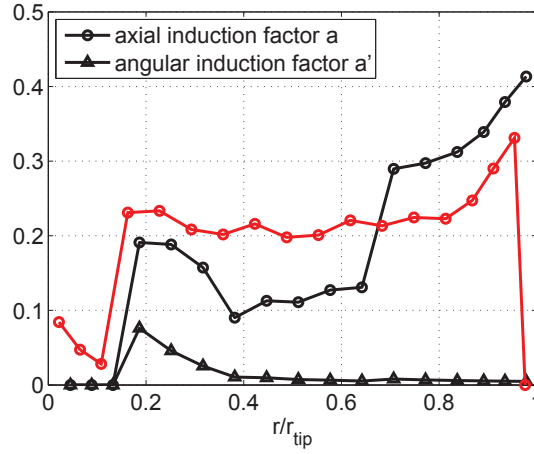
Figure 3.6: Axial and angular induction factors calculated by our BEM code (black lines), and axial induction factor calculated by FAST (red line) for a 5MW wind turbine.

	Wind speed at hub height (m/s)	Rotor speed (rpm)
case 1	6	13
case 2	8	14

Table 3.1: Parameters for the two test cases from Reference [18].

on a full size wind turbine is detailed, including the limitation on the frequency range of Schlinker and Amiet's approach when considering the rotating motion, the coordinate transfer between source and observer, the blade division principles, etc. The wind turbine is a 2.3MW Siemens SWT 2.3-93 wind turbine, with a tower height of $80\,m$, and three 45B blades of length $45\,\mathrm{m}$ that have controllable pitch angle. The chord length is $3.5\,\mathrm{m}$ at the root of the blade and $0.8\,\mathrm{m}$ at the tip, and we assume a linear variation from root to tip. All these data in addition to the sound power level measurements are found in Reference [18]. As for the airfoil section, we choose a NACA 63-415 airfoil, because it is a common airfoil used for a modern wind turbine [79], and it has visually a similar shape as B45 profile [80]. A default AoA of 4° is chosen, as the maximum C_l/C_d value is at an AoA of 4° for $Re = 4 \cdot 10^6$ in Figure 3.7. Two cases mentioned in Reference [18] are summarized in Table 3.1 and studied hereafter.

To apply Amiet's model to a rotating blade, we first divide the 3 blades into segments, then XFOIL is used to calculate the boundary layer related parameters. In this step, blade twist, blade position are taken into account. After coordinate transform, we apply Amiet's model on each segment, to calculate the noise generated

by each segment. Doppler factor is taken into account in this step. Finally, we perform logarithm summation over all segments, to obtain the total SPL for this specific observer position, and specific frequency. Detailed explanations are given in the following sections.
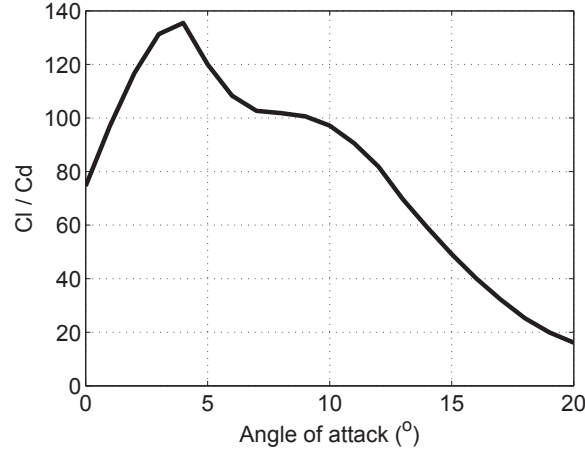
Figure 3.7: C_l/C_d as a function of AoA for a NACA 63-415 airfoil at $Re = 4 \cdot 10^6$.

3.3.1 Limitations of Schlinker and Amiet's approach for a rotating blade

Lowson [81] showed that the effect of rotating motion is weak if the ratio of source angular frequency to rotating speed is high (that is, $\omega/\Omega >> 1$). Since for a wind turbine, the rotor speed is a few radians per second, while the frequencies of interest are typically greater than $100\,Hz$, the effect of rotation is weak. In this case, we can describe the rotating motion by a series of translations over an infinitesimal distance, as proposed by Schlinker and Amiet [62]. Blandeau and Joseph [16] validated Schlinker and Amiet method by comparing it with an analytical model that treats the rotating effect exactly, see Figure 3.8. The exact results are obtained using Ffowcs Williams and Hawkings (FWH) equation for a rotating dipole source to calculate the surface pressure fluctuation, while the far field noise is calculated using Amiet's airfoil transfer function. Comparing the two calculations, a domain of validity based on the frequency range is found. The low frequency limit is proposed as:

$$f_{low} = \frac{c_0}{2\pi \bar{r} \sin \theta_{low}}, \tag{3.4}$$

and the high frequency limit is:

$$f_{high} \simeq \frac{3U_x R_T^{0.57}}{2\pi \delta}, \tag{3.5}$$

	δ (m)	R_T	$f_{high}(Hz)$
root	0.086	53.5	350
tip	0.021	348	5111

Table 3.2: Upper frequency limit estimation for 2.3MW wind turbine with reference velocity of $8\,m/s$ at hub. AoA is set at 4°, and $Re = 4 \cdot 10^6$.

where $\bar{r}$ is the distance between rotor center to the segment, θ_{low} is the angle between the horizontal line and the line connecting the hub and the observer, U_x is the chordwise flow velocity, R_T is the ratio of outer-to-inner timescale (also used in APG wall pressure fluctuation model in Section 2.1.2) and δ is the boundary layer thickness.

(a)   (b)
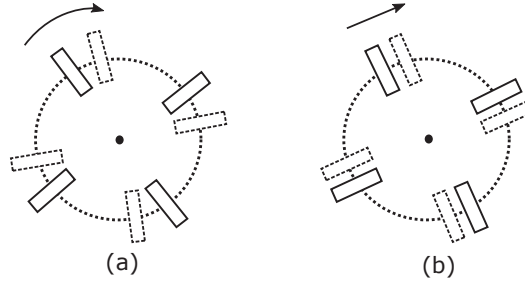
Figure 3.8: Illustration of exact rotor motion and approximated rectilinear motion [16]. (a) Exact FWH based model; (b) rectangular motion approximation.

From Equation (3.4), the highest low limit occurs when the distance $\bar{r}$ is the smallest, that is, the root segment, other segments will have lower low limits. For this particular 2.3 MW wind turbine, the distance between the first segment center to the rotor is $6\,m$, thus the low frequency limits are $15\,Hz$ and $113\,Hz$ for observers located respectively 100 and $1000\,m$ in the downwind direction. The upper frequency limit increases with Reynolds number. The average Reynolds number is around $4 \cdot 10^6$ for the model wind turbine, and the boundary layer related parameters are given in Table 3.2 for the root and tip sections, as well as the frequency limits estimated by Equation (3.5). Calculations are done with XFOIL. We can see for the root segment, the limitation is quite low, however, since most of the sound is produced near the tip region [3], we will calculate our spectra until $5\,kHz$ in the following.

3.3.2 Application to a rotating blade: Doppler effect, blade division and coordinate transfer

Doppler effect

Although the rotating effect is weak for a wind turbine, it can be important for a helicopter rotor. Schlinker and Amiet [62] introduced an expression for the Doppler factor to take into account the rectilinear motion of the source. The Doppler factor

relates the observer frequency ω to the emission frequency ω_e at the source [62, 82]. As shown by Schlinker and Amiet [62] and Sinayoko *et al.* [82], the instantaneous PSD at the observer for an azimuthal blade position β is given by :

$$S_{pp}(\bar{\mathbf{x}}_{\mathbf{0}}, \omega, \beta) = \frac{\omega_e}{\omega} S'_{pp}(\bar{x}, \omega_e, \beta), \tag{3.6}$$

where $\bar{\mathbf{x}}_{\mathbf{0}}$ and $\bar{\mathbf{x}}$ correspond respectively to the observer coordinates in the hub and blade coordinate systems, and $S'_{pp}(\bar{x}, \omega_e, \beta)$ is given by the Equation (2.37) and (2.67). They also derived an expression for the azimuthally averaged spectrum:

$$S_{pp}(\bar{x}_0, \omega) = \frac{1}{2\pi} \int_0^{2\pi} \frac{\omega_e}{\omega} S_{pp}(\bar{x}_0, \omega, \beta) d\beta = \frac{1}{2\pi} \int_0^{2\pi} \left(\frac{\omega_e}{\omega} \right)^2 S'_{pp}(\bar{x}, \omega_e) d\beta. \tag{3.7}$$

Blade division

Another issue related to blade rotation is that the flow is not uniform along the span, with incoming velocity strongly increasing from root to tip, and its chord varying from root to tip. To better describe these spanwise-varying conditions, it is desired to divide the blade into short segments or strips. If the span-wise turbulence correlation length l_y is smaller than the segment span, we can assume that calculated far field power spectrum density of SPL between segments are uncorrelated. As a result, the overall noise radiated by the blade is the logarithmic sum of the contributions from all blade segments. Here, l_y is modeled by Corcos model, that suggests the correlation length decreases with increasing frequency:

$$l_y(\omega) = \frac{b_c U_c}{\omega}, \tag{3.8}$$

where b_c is a constant determined by experiment: 2.1 according to Amiet [41], $1.6 - 1.7$ depending on the inflow velocity for Brooks and Hodgson [71], and 1.47 following Rozenberg *et al.* [67]. Similarly, various values of the convection velocity U_c have been proposed: $U_c = 0.8U$ according to Amiet [41], or $U_c = 0.7U$ following Rozenberg *et al.* [67]. DTU studies [83, 84] suggest a variation of U_c with frequency: $U_c = 0.7U$ for frequencies up to $1000\,Hz$, then decreases to $U_c = 0.4U$ at $2\,kHz$, and remains constant at higher frequencies. In this work, we choose $b_c = 1.47$ and $U_c = 0.7U$.

Besides the span-wise correlation length l_y limitation on the segment length, there is also another requirement to meet, that is the large aspect ratio assumption in Amiet's model. Roger and Moreau [61] suggest that for an airfoil with aspect ratio greater than 3, the simplified formulations can be used without losing accuracy. Thus we keep a constant aspect ratio of 3, and the blade is accordingly divided into 8 segments, as shown in Figure 3.9. To calculate the largest correlation length, which corresponds to the shortest blade span, we assume a wind velocity $U = 10\,m/s$, a rotor speed of $2\,rad/s$, and a lower frequency limit of $50\,Hz$. According to Corcos model, the ratio of correlation length to span is shown in Figure 3.10. We can see that along the blade, the ratio is less than 1, it is to say, when dividing blade this

way, the criteria of span-wise correlation length being less than span is fulfilled. Thus in the following calculations, each blade will be treated as 8 uncorrelated segments, and the total SPL will be calculated as the logarithm summation of 8×3 segments.
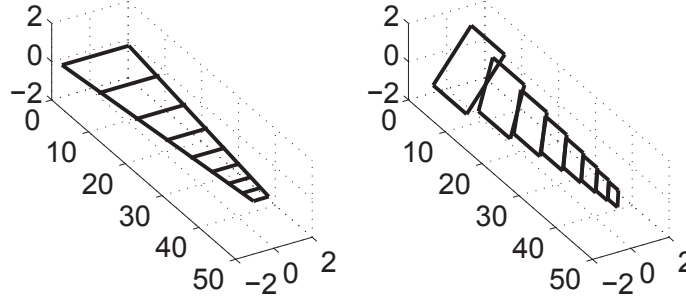
Figure 3.9: Blade division while keeping a constant aspect ratio of 3.
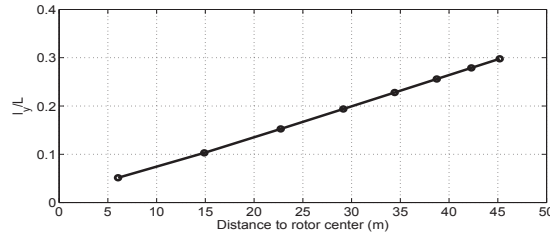
Figure 3.10: Ratio between span-wise correlation length and the span along a blade.

Coordinate transfer

In Amiet's model, the coordinate is based on the plate (source coordinate). For a wind turbine blade, each segment has a different orientation and physical position due to blade twist, blade extension and blade pitch, etc (see the right figure in Figure 3.9). Thus it is necessary to transfer the observer coordinate to the source coordinate, that is, calculate observer position with respect to each segment (source). To do this, we first need to know how the orientation of the segments are modified due to various angles (see Figure 3.11).

- Wing angle β: the angle between vertical axis and the blade axis;

- Blade twist θ_{twist} and pitch θ_{pitch}: the angle between chordline and rotor plane.

The process is illustrated in Figure 3.11. We start with the ground coordinates, where the origin is at wind turbine hub, x is cross-wind direction, y is vertical direction, z is wind direction. In this coordinate system, the receiver location is

(a) Wing angle β (b) Twist and pitch angle
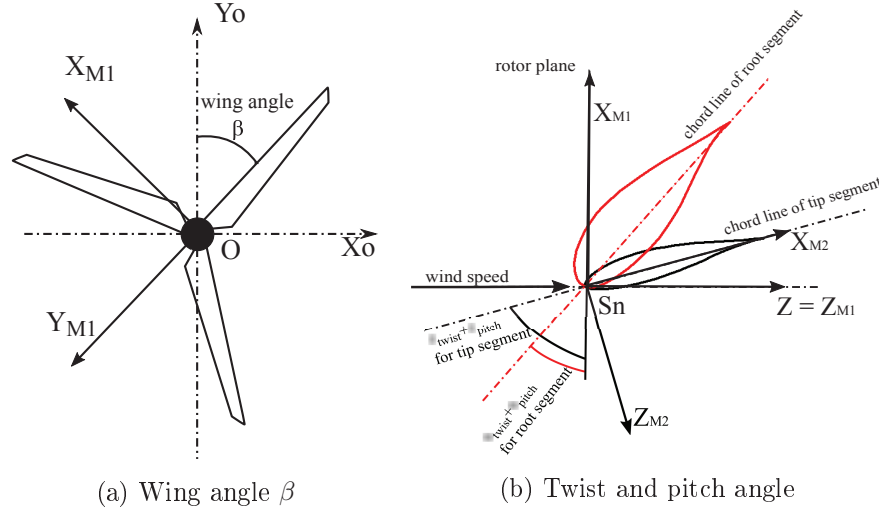
Figure 3.11: Illustration of relative angle during coordinate transfer.

$\vec{OR} = (x_o, y_o, z_o)$, with O is the center of the rotor, R the receiver position. Now to transfer the ground coordinates to the one based on blade position β, see Figure 3.11 (a), we rotate the ground coordinates about the z-axis by an angle $\pi - \beta$. The transfer matrix is:

$$M_1 = \begin{bmatrix} -\cos\beta & \sin\beta & 0 \\ -\sin\beta & -\cos\beta & 0 \\ 0 & 0 & 1 \end{bmatrix}$$

.

Twist and pitch angles vary with segment along a blade, because each segment encounters a different rotating velocity, thus adjusting twist and pitch angles ensure a desired AoA at leading edge. This coordinate transfer is to make sure the system has the same coordinate as Amiet's model requires (x-axis along chord and y-axis along span). Thus, we need to rotate the (x_{M1}, z_{M1}) plane around y_{M1} axis by an angle of $\theta_{twist} + \theta_{pitch}$, see Figure 3.11 (b). The transfer matrix is:

$$M_2 = \begin{bmatrix} \cos(\theta_{twist} + \theta_{pitch}) & 0 & -\sin(\theta_{twist} + \theta_{pitch}) \\ 0 & 1 & 0 \\ \sin(\theta_{twist} + \theta_{pitch}) & 0 & \cos(\theta_{twist} + \theta_{pitch}) \end{bmatrix}$$

.

After these transformations, the receiver is in the local segment system, that is to say, in a system where the origin is in the hub, x_{M2} is in local flow direction, y_{M2} is in span-wise direction and z_{M2} is the normal to the airfoil surface. The last step is a coordinate translation by a value of $d_n = OS_n$, $n = 1..8$ to the local segment, that is, to move the origin of the xyz_{M2} system from the hub to the local segment center. Thus the observer coordinate in the final system is:

$$\begin{bmatrix} x \\ y \\ z \end{bmatrix} = M_2 \cdot M_1 \cdot \begin{bmatrix} x_o \\ y_o \\ z_o \end{bmatrix} + \begin{bmatrix} 0 \\ d \\ 0 \end{bmatrix}$$

We neglected the angle between the wind direction and rotor axis (yaw angle) and the angle between the blade and the rotor plane (cone angle), because we don't have precise information about these angles.

3.3.3 Atmospheric turbulence and wind shear modeling

Monin-Obukhov Similarity Theory (MOST) is used to study the influence of atmospheric turbulence and wind shear on wind turbine noise. This theory applies to the atmospheric surface layer, where surface fluxes are relatively constant, and is valid over a flat and homogeneous ground [85, 86, 87]. The main parameters of the model are the friction velocity u_* and the sensible heat flux H, or equivalently the temperature scale T_*. u_* is defined as:

$$u_* = [(\bar{u'w'})^2 + (\bar{v'w'})^2]^{1/2}, \tag{3.9}$$

where u', v' and w' are the three turbulence velocity components. The root-mean-square of turbulence velocity fluctuation σ_u and turbulence outer length scale L_{outer} can be calculated with given H and u_* for a certain height according to Cheinet [87].

The stability of the atmosphere is then described by the Obukhov length L_* given by [85, 87]:

$$L_* = \bar{T}u_*^2/(\kappa g T_*) = -\frac{\rho_0 C_p \bar{T} u_*^3}{\kappa g H}, \tag{3.10}$$

with $\bar{T}$ the potential temperature, $\kappa = 0.41$ the von Kármán constant, g the gravity acceleration, and C_p the specific heat of dry air. For ordinary calculations, a value of $C_p = 1.0 kJ/Kg \cdot K$ is enough. The atmosphere is unstable when $L_* < 0$ ($H > 0$) and stable when $L_* > 0$ ($H < 0$). When the shear production of turbulence is much larger than the buoyant production, the atmosphere is called neutral and $1/L_* \approx 0$ ($H \approx 0$).

The mean velocity profile as a function of height z can then be obtained using similarity relations [35, 85]:

$$U(z) = \frac{u_*}{\kappa}\left[\ln\left(\frac{z}{z_0}\right) - \psi_u\right], \tag{3.11}$$

where z_0 is the surface roughness length and the functions ψ_u depend on the stability of the atmosphere. In neutral conditions, $\psi_u = 0$ and the classical logarithmic profile is obtained. These velocity profiles are sometimes called Businger-Dyer profiles, here we use a slightly modified version of these profiles given in Reference [35]. Using MOST, it is also possible to predict turbulence parameters that vary with height to represent the inhomogeneity of the atmospheric boundary layers. The von Kármán spectrum of Equation (2.69) is still used, but with height-dependent standard deviation of turbulent velocity fluctuations σ_u and integral length scale Λ.

Case 1: $U(80\,\text{m}) = 6\,m/s$		
$H(W/m^2)$	$u_*(m/s)$	$L_*(m)$
-10	0.29	235
0	0.37	Inf
40	0.42	-168
Case 2: $U(80\,\text{m}) = 8\,m/s$		
$H(W/m^2)$	$u_*(m/s)$	$L_*(m)$
-25	0.38	200
-10	0.46	905
0	0.49	Inf
40	0.53	-348
200	0.58	-92

Table 3.3: Atmospheric parameters derived from MOST for hub height mean velocity corresponding to cases 1 and 2.

Since detailed parameters concerning the atmospheric conditions during the wind turbine noise measurements are not mentioned in Reference [18], we choose realistic parameters found in the literature. The heat flux H typically varies over the range $-50\,\text{W/m}^2$ to $600\,\text{W/m}^2$ during a diurnal cycle [85]. Following Ostashev and Wilson [88], we select a value of $200\,\text{W/m}^2$ for mostly sunny conditions, and $40\,\text{W/m}^2$ for mostly cloudy conditions. For stable conditions, typically occurring at night, values of $-10\,\text{W/m}^2$ and $-25\,\text{W/m}^2$ are chosen for H. Then we deduce the friction velocity from Equation (3.11) so that the mean velocity at hub height is $6\,\text{m/s}$ for case 1 or $8\,\text{m/s}$ for case 2. The results are summarized in Table 3.3. Results for $H = -25\,\text{W/m}^2$ and $200\,\text{W/m}^2$ are not shown for case 1 because they yield $|L_*| < 50\,\text{m}$, and it is generally admitted that MOST is only valid for $|z/L_*| < 1 - 2$ [86]. Let us note that for $H = 200\,\text{W/m}^2$ and $U(80\,\text{m}) = 8\,m/s$, the validity of MOST might be questionable for the highest part of the rotor.

The different possible wind profiles are plotted in Figure 3.12 for cases 1 and 2. The wind shear is clearly stronger in stable conditions compared to neutral or unstable conditions. For case 2, the wind speed increases from 6.2 to $9.5\,\text{m/s}$ between the bottom and top parts of the rotor for $H = -25\,\text{W/m}^2$, while it remains close to $8\,\text{m/s}$ for unstable conditions. The turbulence parameters σ_u and Λ are plotted for case 2 in Figure 3.13. Using expressions given by Cheinet [87], σ_u is independent of height in neutral and unstable conditions, while it increases with height in stable conditions. The integral length scale always increases with height, but in a much quicker way in stable atmospheres. The turbulence level given by von Kármán spectrum will thus be a combination of these two effects, as this level increases with increasing σ_u bu decreases with increasing Λ.

(a) Case 1: $U(80\,\mathrm{m}) = 6\,m/s$.

(b) Case 2: $U(80\,\mathrm{m}) = 8\,m/s$.
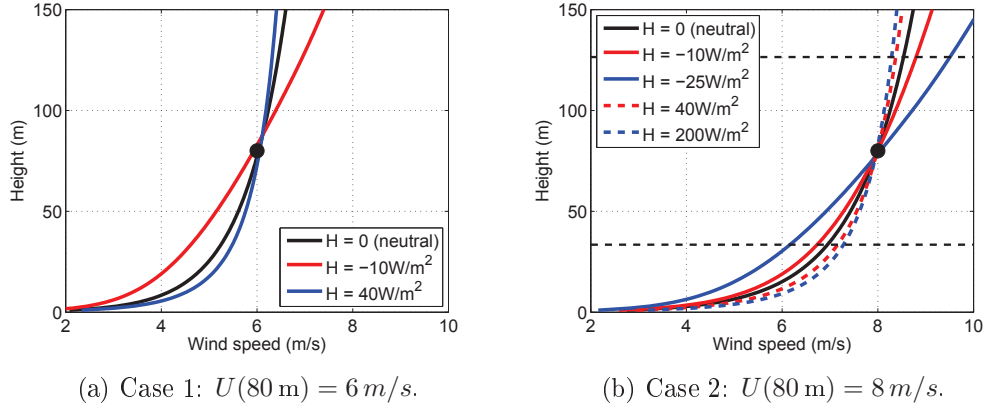
Figure 3.12: Mean wind profiles $U(z)$ for the atmospheric conditions described in Table 3.3. The minimum and maximum rotor heights are shown using black dashed lines.

(a)

(b)
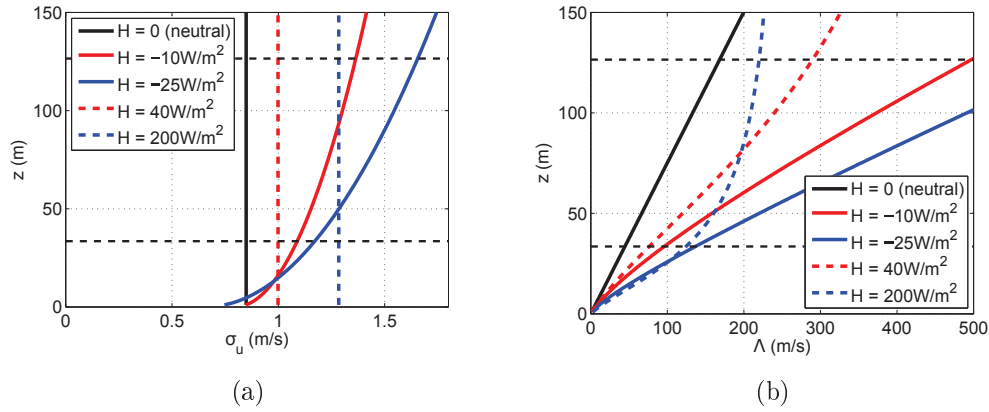
Figure 3.13: (a) Standard deviation of turbulent velocity fluctuations σ_u and (b) integral length scale Λ for a reference velocity of $U(80\,\mathrm{m}) = 8\,m/s$. The minimum and maximum rotor heights are shown using black dashed lines.

3.4   Results and discussions

Amiet's models for turbulent inflow noise and trailing edge noise are applied to a 2.3MW Siemens 2.3-93 wind turbine. Predictions are explained in detail in this section. Comparisons with measurements from Reference [18] for a constant wind profile and no turbulence are given in Section 3.4.1; only trailing edge noise is included in that case. It is followed by the prediction results with atmospheric conditions obtained by MOST theory for turbulent inflow noise and trailing edge noise in Section 3.4.2. At the end, in Section 3.4.3, Amiet's model is compared with BPM semi-empirical model, and the influence of separation noise is emphasized.

3.4.1   Results for a constant wind speed and no atmospheric turbulence

3.4.1.1   Third octave band power spectra and comparison with experiments

Assuming free field conditions, the sound power level SWL is calculated by $SWL = SPL + 10 \log_{10}(4\pi R^2)$, with R the distance from the rotor to the observer. The SWL predictions are compared to the measurements in figures 3.14 and 3.15 for the two cases described in Table 3.1. The observer is located on the ground 100 m downwind, and the spectra are azimuthally averaged as given by Equation (3.7). Using the APG model on the suction side, the predictions agree well at high frequencies, above 200 Hz for case 1 and 1000 Hz for case 2. For both cases, trailing edge noise is dominated by the suction side contribution at lower frequencies, and by the pressure side contribution at higher frequencies. Using the ZPG model on the suction side, the predictions are up to 10 dB lower compared to the APG model predictions, and are lower than measurements over the whole frequency range. At low frequencies, both model predictions underestimate the measurements, which can be attributed to the fact that other noise mechanisms dominate at low frequency.

3.4.1.2   Directivity and amplitude modulation of sound pressure level

The horizontal directivity of overall SPL is plotted in figure 3.16(a) for cases 1 and 2. The maximum levels are obtained upwind and downwind, while the minimum levels are found crosswind, which is in agreement with field measurements close to a wind turbine [3]. This shape can be explained by the directivity of trailing edge noise, coming from the assumption of dipole distribution in Amiet's. This directivity is determined by the orientation of the blade.

Amplitude modulation (here it refers to the normal amplitude modulation) is caused by the the noise source directivity on the rotating blades, and has a frequency of 1/3 the blade rotating frequency for a 3-bladed wind turbine. Subtracting the mean SPL from the SPL at blade azimuthal position β, we can visualize AM in Figure 3.17 for observers in downwind and crosswind direction. The AM is almost identical for cases 1 and 2. The variations are small in the downwind direction, and
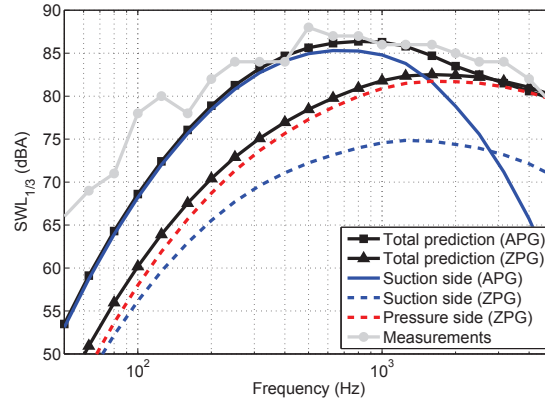
Figure 3.14: Third octave band spectra of sound power level for case 1 ($U = 6\,\mathrm{m/s}$) considering APG or ZPG models of trailing edge noise.
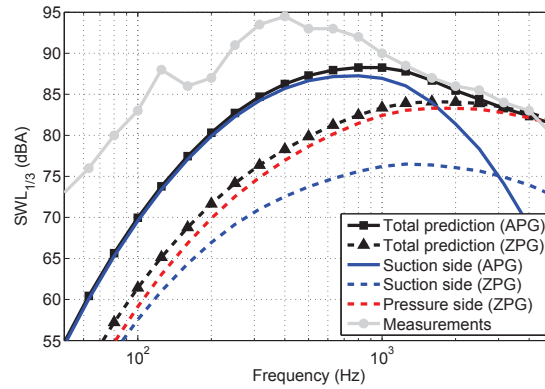
Figure 3.15: Third octave band spectra of sound power level for case 2 ($U = 8\,\mathrm{m/s}$) considering APG or ZPG models of trailing edge noise.
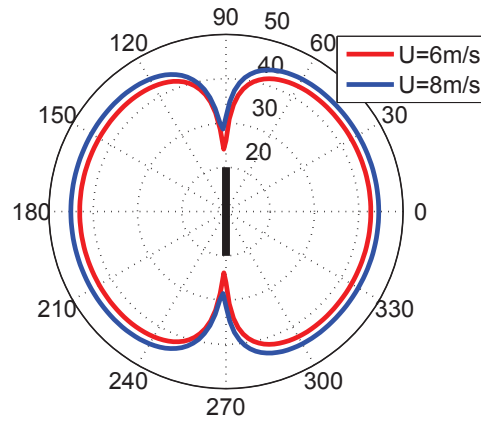
(a) Directivity of overall SPL.
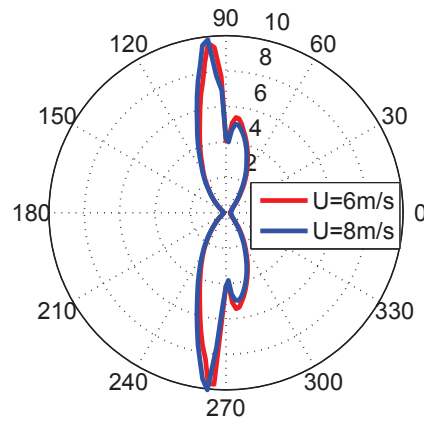
(b) Directivity of amplitude modulation strength.

Figure 3.16: Directivity of (a) overall SPL and (b) amplitude modulation strength. The black line indicates the rotor plane when looking from above, and the wind is coming from the left.

much more important in the crosswind observers. We define the AM strength as
the difference between minimum and maximum values of SPL over blade azimuthal
position β. The AM strength is approximately $4\,\mathrm{dB(A)}$ crosswind and less than
$0.3\,\mathrm{dB(A)}$ downwind. Figure 3.16(b) shows the directivity of AM strength for cases 1
and 2. Large values of AM strength, of up to $10\,\mathrm{dB(A)}$, are found in the vicinity of
the crosswind directions, where the minimum overall SPL values are found according
to Figure 3.16(a). These predictions are in good qualitative agreement with field
measurements [3].
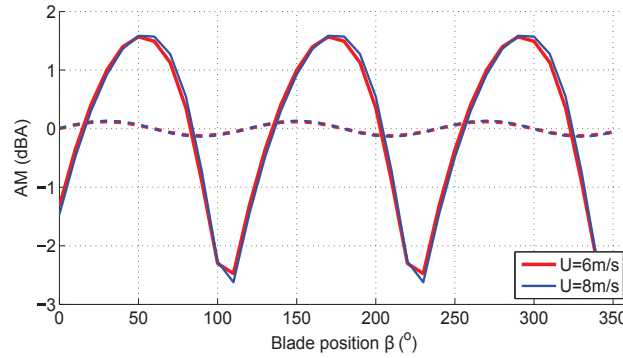
Figure 3.17: Amplitude modulation in the downwind (dashed lines) and cross-wind
(solid lines) directions for cases 1 and 2. The observer is $100\,\mathrm{m}$ away from the wind
turbine, and AM is obtained by subtracting the mean SPL from $\mathrm{SPL}(\beta)$.

3.4.2 Results with wind shear and atmospheric turbulence

3.4.2.1 Effect of wind shear on wind turbine trailing edge noise

The noise radiated by a wind turbine depends on wind profile (wind speed, wind
shear), mostly because an increase in wind speed causes an increase of the AoA seen
by a blade segment. As an example, the variation of AoA over the rotor plane due to
wind shear is plotted in Figure 3.18 for case 2 with $H = -25\,\mathrm{W/m^2}$. The maximum
AoA variation over one rotation is approximately $\pm1.5^o$ for the tip segment. As a
result, the turbulent boundary layer parameters vary with blade azimuthal position
β. For instance, Figure 3.19 shows the variation of the displacement thickness δ_s^*
on the suction side for the different wind profiles corresponding to case 2. The
boundary layer thickness of the tip segment decreases from $\beta = 0$, where the blade
is pointing up to $\beta = 180^o$, where the blade is pointing down. This decrease is
most significant for the stable atmosphere with $H = -25\,\mathrm{W/m^2}$. These changes in
boundary layer parameters cause a significant change in the wall pressure spectra
plotted in Figure 3.20 as a function of β. The spectral peak shifts to higher
frequency when the blade goes from top to down positions, corresponding to a
decrease of AoA from 5.2^o to 2.5^o. These spectral variations due to wind shear are
in good agreement with surface pressure measurements performed in the framework
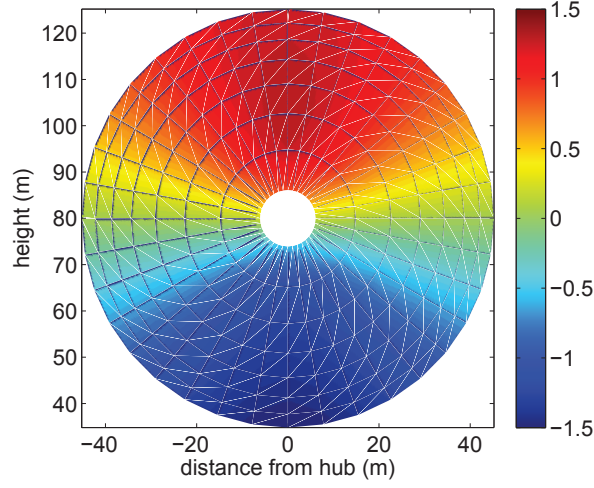
Figure 3.18: AoA variation in degrees due to wind shear for $U(80\,\mathrm{m}) = 8\,m/s$ and $H = -25\,\mathrm{W/m^2}$.
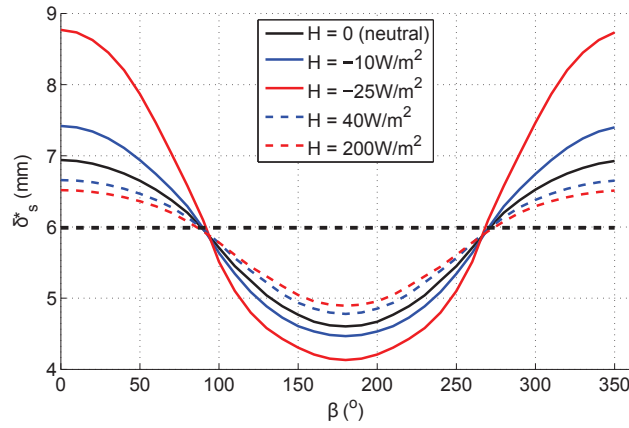
Figure 3.19: Variation of displacement thickness δ_s^* on the suction side as a function of blade azimuthal position β for the tip segment for case 2. The thick dashed line corresponds to the reference value with a constant wind profile.

of the DANAERO project for a similar size wind turbine [17], plotted in Figure 3.21.

This significant effect of wind shear on the emission side is much less pronounced on the receiver side, as can be seen in the sound power level spectra of Figure 3.22 calculated at a receiver 100 m downwind. On the suction side, a SWL increase is observed at high frequencies, of approximately 1 dB(A) at 2 kHz and 3 dB(A) at 4 kHz. However, this increase is not observed on the pressure side, and since pressure side levels dominate above 2 kHz the maximum increase due to wind shear is only 0.4 dB(A) at 2 kHz on the total TEN spectrum.

The fact that level variations due to wind shear are less pronounced on the receiver side (Figure 3.22) compared to the emission side (Figure 3.20) may be explained by the fact that the 3 blades and all the blade segments are considered to calculate the azimuthally-averaged spectra of Figure 3.22, thus variations due to wind shear tend to be averaged out. We must keep in mind that stronger wind shear than those predicted by MOST usually exist in reality, because in practice the terrain might not be flat and homogeneous (topography effects), and because other sources of inhomogeneities such as large-scale turbulence or wakes of other turbines might be present [89, 90, 17].

3.4.2.2 Effect of atmospheric turbulence on wind turbine turbulent inflow noise

Amiet's model for turbulent inflow noise directly depends on the turbulence spectrum Φ_{ww}, as seen in Equation (2.67). It is modeled using a von Kármán spectrum with turbulence parameters σ_u and Λ depending on height or equivalently on the blade azimuthal position β. Figure 3.23 shows how the turbulence spectrum varies with β for the tip segment at 100 Hz. The maximum spectral levels are found for the unstable atmosphere with $H = 200 \, \text{W/m}^2$ during the whole rotation, which can be explained by the relatively high value of σ_u and low value of the turbulent length scale Λ for this case, as seen in Figure 3.13. The same trends are observed for other frequencies.

Figure 3.24 shows the azimuthally-averaged SWL spectra calculated at a receiver 100 m downwind associated with the same atmospheric conditions. As it could be foreseen from Figure 3.23, the maximum levels are obtained for $H = 200 \, \text{W/m}^2$ and the minimum levels for $H = 0$ and $H = 40 \, \text{W/m}^2$. The differences are significant, with up to 2 dB(A) of difference between the various atmospheric conditions. Let us note that the leading edge thickness correction presented in Section 2.2.2 has a negligible effect on the final results. Indeed, integral length scales Λ are much larger than the blade chord c, thus Λ/c in Equation 2.70 is large and SPL_R is small, with a maximum reduction of 0.3 dB obtained for the root segment. Again, as already mentioned previously for trailing edge noise, we must keep in mind that stronger turbulent variations than those predicted by MOST may exist in reality, especially when a wind turbine happens to be in the wake of another turbine [17, 90].
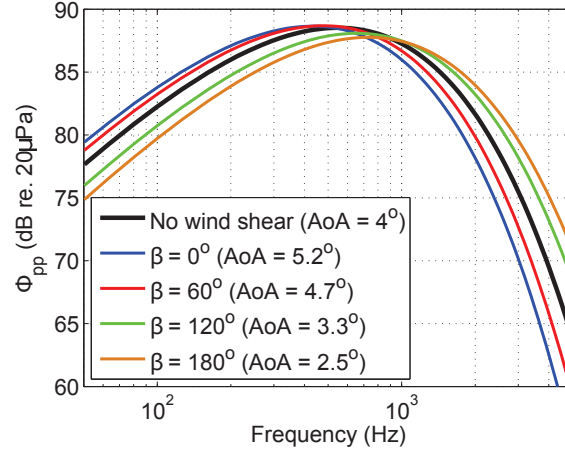
Figure 3.20: Variation of wall pressure spectra Φ_{pp} on the suction side for different blade azimuthal position β for the tip segment, considering case 2 with $H = -25 \, \mathrm{W/m^2}$.
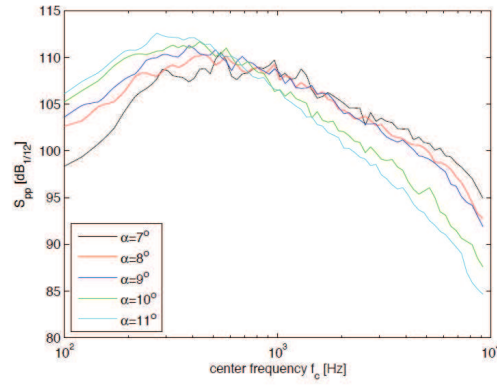
Figure 3.21: Narrow band spectra in dB (1/12th octave) of surface pressure binned on angle of attack measured during DANAERO project. Taken from Madsen [17].
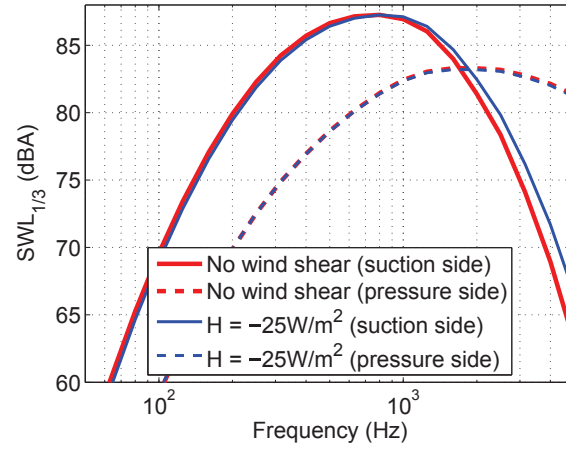
Figure 3.22: Third octave band spectrum of SWL for TEN on pressure and suction side for case 2 with no wind shear (constant wind speed) and with $H = -25\,\mathrm{W/m^2}$.
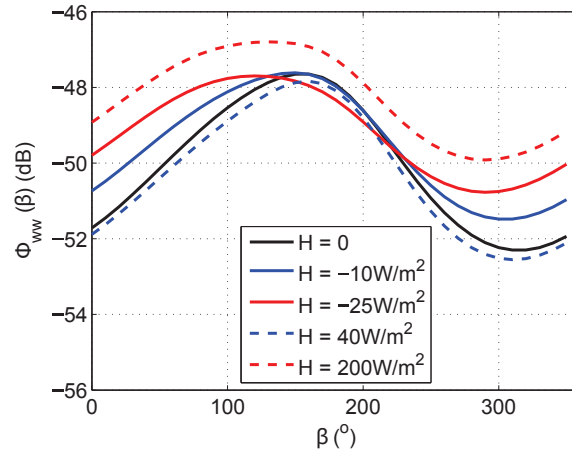
Figure 3.23: Variations of turbulence spectrum Φ_{ww} as a function of blade azimuthal position β for the tip segment at $100\,\mathrm{Hz}$ and for the various atmospheric conditions corresponding to case 2.
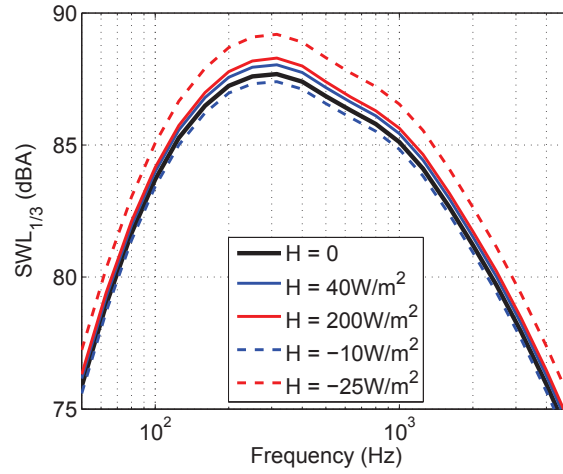
Figure 3.24: Third octave band spectrum of SWL for turbulent inflow noise and for the various atmospheric conditions corresponding to case 2.

3.4.2.3 Combined effect on overall sound power level

The total SWL spectra including both trailing edge noise and turbulent inflow noise are compared to measurements of Reference [18] in Figures 3.25 and 3.26 for cases 1 and 2. We consider here a neutral atmosphere ($H = 0$), which means the turbulent inflow noise levels are relatively low according to Figure 3.24. It appears that turbulent inflow noise is dominant at low frequencies, up to 300 to 500 Hz, while trailing edge noise is dominant at higher frequencies. The agreement between predictions and measurements is now quite satisfactory along the whole frequency band. For case 1, let us note that predictions slightly overestimate the measurements at low frequency, which might indicate that the turbulent inflow noise needs some improvements at these frequencies and/or that the atmospheric turbulence parameters are not well modeled. For case 2, the experimental spectral peak around 400 Hz is not captured by the model, which may be due to some other noise sources such as separation/stall noise.

The horizontal directivities of overall SPL and of AM strength are plotted in Figure 3.27 and Figure 3.28 for a neutral atmosphere ($H = 0$) and for case 2 ($U(80\,\text{m}) = 8\,m/s$). Results are given for trailing edge noise only, turbulent inflow noise only and for the total noise. It appears that the maxima of overall SPL for the 3 curves are found upwind and downwind, and the minima are found crosswind ($90^o \pm 2^o$ and $270^o \pm 2^o$). As already seen in Section 3.4.1, the AM strength is smaller than 1 dB in the upwind and downwind directions, and is maximum close to the crosswind direction, at slightly different directions for the three curves. The AM strength reaches a maximum of 10 dB a little upwind for trailing edge noise, of 9 dB a little downwind for turbulent inflow noise, and of only 4 dB exactly crosswind for the total noise.
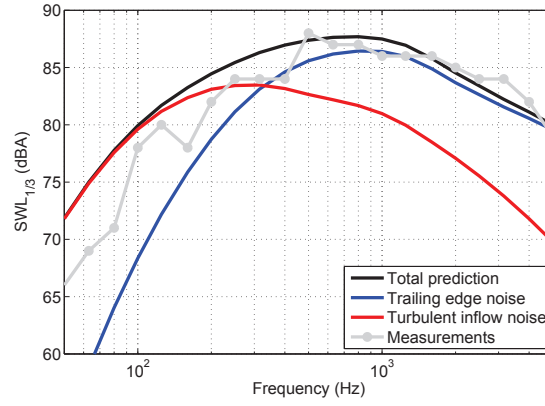
Figure 3.25: Third octave band spectrum of SWL for trailing edge noise and turbulent inflow noise for case 1 and $H = 0$ (neutral atmosphere).
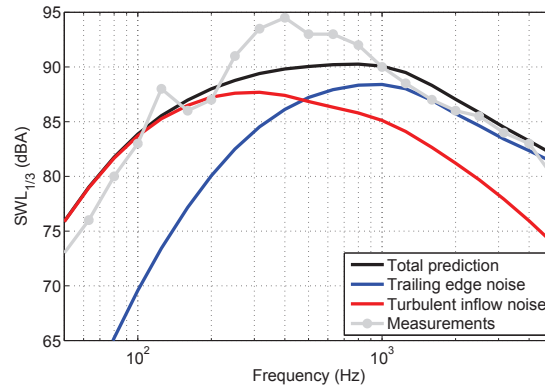
Figure 3.26: Third octave band spectrum of SWL for trailing edge noise and turbulent inflow noise for case 2 and $H = 0$ (neutral atmosphere).
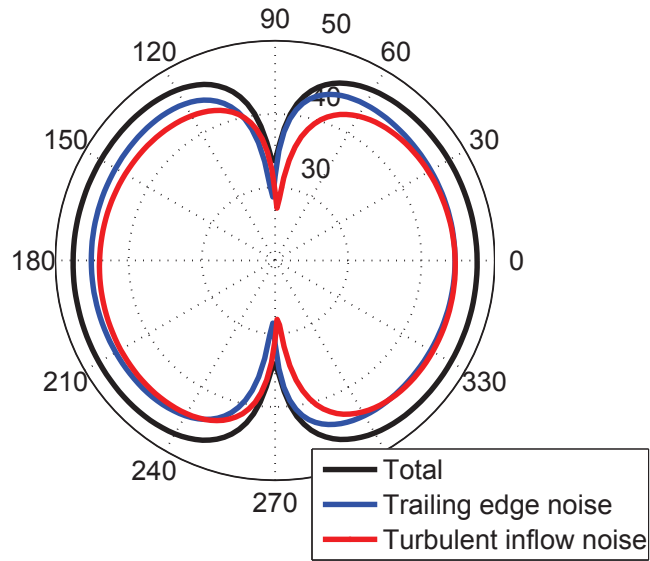
Figure 3.27: Directivity of overall SPL by a receiver at 100 m away from the wind turbine for case 2 with $H = 0$ (neutral atmosphere) when looking from above, the wind is coming from the left.
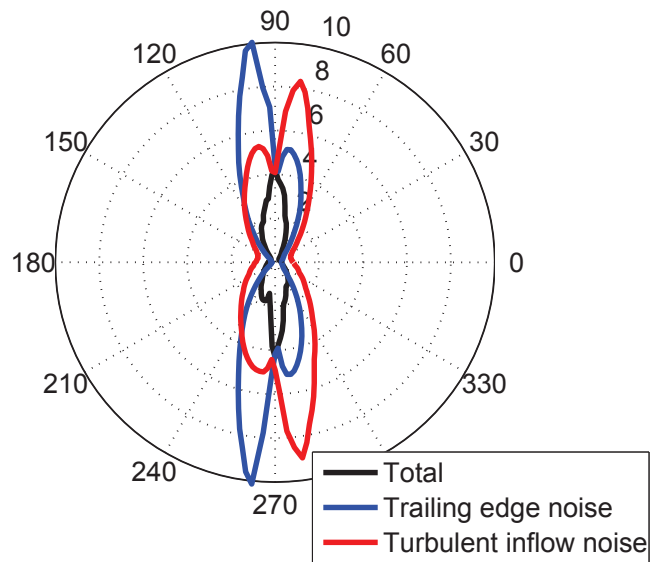
Figure 3.28: Directivity of amplitude modulation by a receiver at 100 m away from the wind turbine for case 2 with $H = 0$ (neutral atmosphere) when looking from above, and the wind is coming from the left.

To explain these differences, let us look first at the directivity of a tip segment in the coordinate system of the blade, as shown in Figure 3.29. The blade is pointing upwards, and the observer is at $100\,m$ away in the downwind direction. Amiet's model predicts that trailing edge noise radiation is maximum towards the leading edge of the blade, while turbulent inflow noise radiation is maximum towards the trailing edge. The normalized directivity are frequency-dependent, with more lobes appearing with increasing frequency. Note that in the low frequency limit a simple dipole shape is retrieved. This directivity pattern, as well as the twisting of the blade schematically represented in Figure 3.9, do explain that the directions where the minima are found are slightly different for the two noise mechanisms.
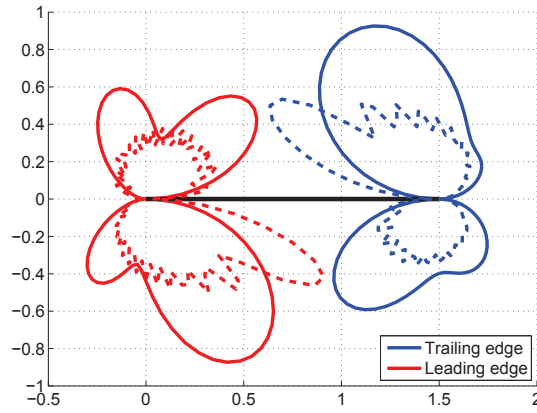
Figure 3.29: Normalized directivity of TE and TI for the tip segment of the blade who is pointing up. Solid lines: $f = 500\,Hz$; dashed lines: $f = 4000\,Hz$.

To better understand the directivity of AM strength, it is also useful to look at the variation of SPL as a function of blade azimuthal position β shown in Figure 3.30 for directions 270° and 278°. At 270°, exactly crosswind, trailing edge noise and turbulent inflow noise variations are in phase and their levels are comparable, which explains that the total noise follows the same trend with similar AM for the three curves. At 278°, slightly downwind, the situation is quite different with both mechanisms having out of phase variations and turbulent inflow noise levels being close to their minimum values. As a result, the total noise mostly follows the trailing edge noise variations and its AM strength is only $3\,\text{dB(A)}$, much smaller than the $9\,\text{dB(A)}$ obtained for turbulent inflow noise.

3.4.3   Comparisons with semi-empirical BPM model

A currently widely used semi-empirical model by Brooks *et al.* [1] (BPM model) is also used to predict the trailing edge noise and separation noise for the same model WT, and for these two cases. In the BPM model, the only input parameters are AoA, and the displacement thickness δ^* on both suction and pressure sides.
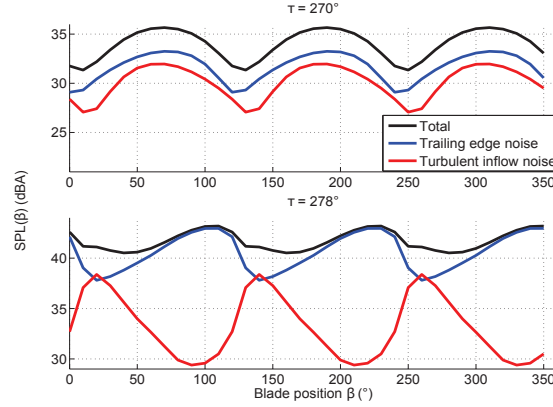
Figure 3.30: Amplitude modulation for trailing edge noise, turbulent inflow noise and for the overall noise at an horizontal angle of 270° (top) and of 278° (bottom) with respect to the wind direction, for case 2 and $H = 0$.

First, Amiet's predictions are compared with the ones by BPM model using the boundary layer parameters calculated with XFOIL for the same NACA 63-415 airfoil. Default AoA is 4° for all cases, and pitch angle is assumed to be zero. From Figure 3.31, we can see for both cases that the separation noise (SN) is not negligible even though the AoA is small. The separation noise peak appears at around $500 - 600\,Hz$. With consideration of SN, for case 1, the total SPL (TEN + SN) is a little higher than the measurements; while for case 2, the total SPL is still lower than the measurements, but the results are closer. If we compare the TEN calculated by Amiet's and BPM model, we can see that BPM model underestimate the results more at low frequencies, while at high frequencies, both models give similar results.

In Leloudas' report, the pitch angle is set as 3° and -2° for cases 1 and 2 respectively, which corresponds to an AoA of 1° for case 1 and 6° for case 2 in our calculations. In Figure 2.16 of Chapter 2, we saw that according to BPM model, separation noise might become dominant for AoA greater than 5°. Therefore, we launch the BPM model again, by considering the separation noise and trailing edge noise with pitch effect; the results are shown in Figure 3.32. We can see that for case 2, the separation noise predicted by BPM model has now a peak close to 400-500 Hz. The sum of trailing edge noise and separation noise agrees well with the measurements higher than 200 Hz for AoA = 6°. On the other hand, for case 1, since the pitch angle leads to a smaller AoA, the separation noise is less likely to be visible in the measured spectrum.

Second, comparisons are for total SWL (trailing edge noise + turbulent inflow noise) between our results by Amiet's model (in blue) and predictions by
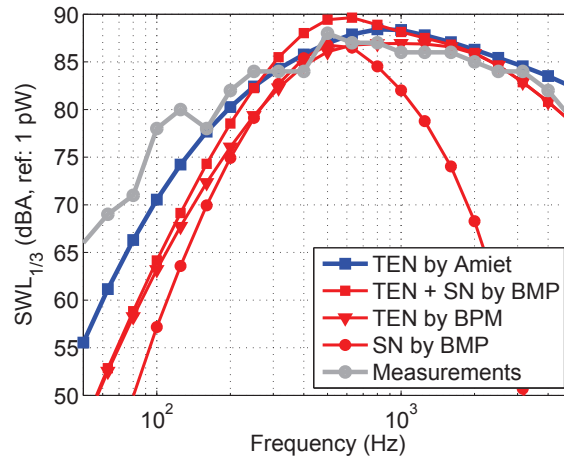
(a) Reference velocity $U_{ref} = 6\,m/s$.
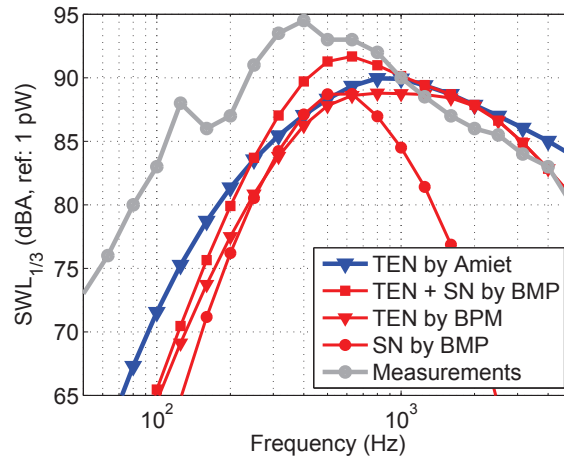
(b) Reference velocity $U_{ref} = 8\,m/s$.

Figure 3.31: SWL predicted by Amiet's model for trailing edge noise, and by semi-empirical model for trailing edge noise and separation noise. Observer is located at $100\,m$ downwind direction.
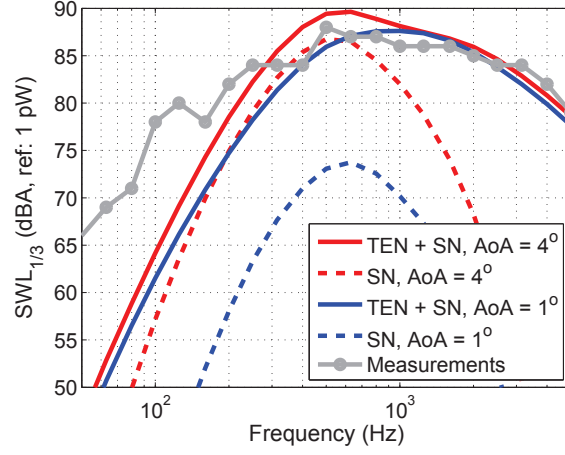
(a) Reference velocity $U_{ref} = 6\,m/s$, pitch angle is 3°, corresponding to AoA of 1°.
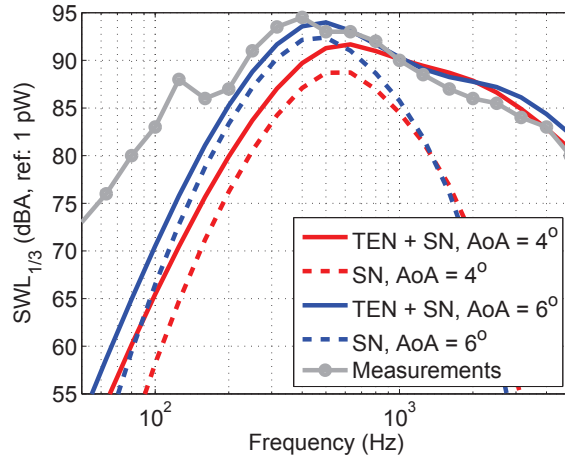
(b) Reference velocity $U_{ref} = 8\,m/s$, pitch angle is -2°, corresponding to AoA of 6°.

Figure 3.32: Third octave band spectrum of SWL predicted by semi-empirical model for trailing edge noise and separation noise. Solid lines: with pitch effect; dashed lines: with default AoA of 4°; symbols: measurements from [18]. Observer is located at $100\,m$ downwind direction.

Leloudas [18] with BPM model (in red), as shown in Figure 3.33, for cases 1 and 2 respectively. Note that the AoA and airfoil type are not given explicitly by Leloudas, thus his boundary layer parameters are likely to be different from ours. We can observe similar results as in Figure 3.32 for case 2 that BPM model could capture the spectral peak at around 400Hz due to separation noise. Thus Leloudas' results agree better with measurements than ours for case 2. However, for case 1, our predictions are in better agreement with the measurements for the whole spectrum expect below 100 Hz. Figure 3.34 shows the comparisons for trailing edge noise and turbulent inflow noise separately for case 1. The results are quite different between the two models. In Leloudas' results, turbulent inflow noise is modeled with a modified Amiet's model by Lowson [91]. This model is formed with a high frequency range expression and a low frequency range expression. There are discrepancies between the turbulent inflow noise calculations by Lowson's modified model and Amiet's original model predictions. This may also be due to the different atmospheric turbulence parameters used, for example, turbulence intensity, turbulence integral length scale, since those values are not given in Leloudas' report.
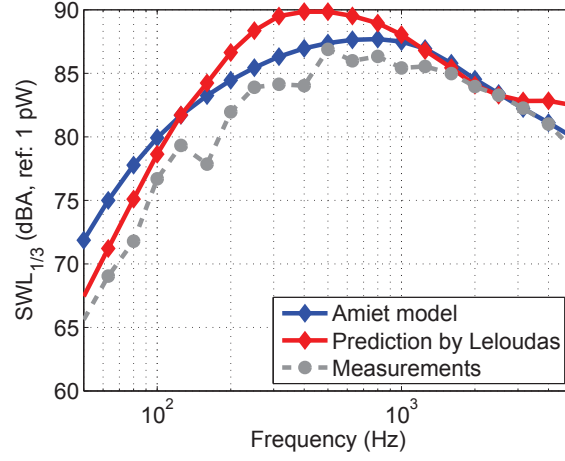
(a) Reference velocity $U_{ref} = 6\,m/s$, pitch angle is 3°, corresponding to AoA of 1°.
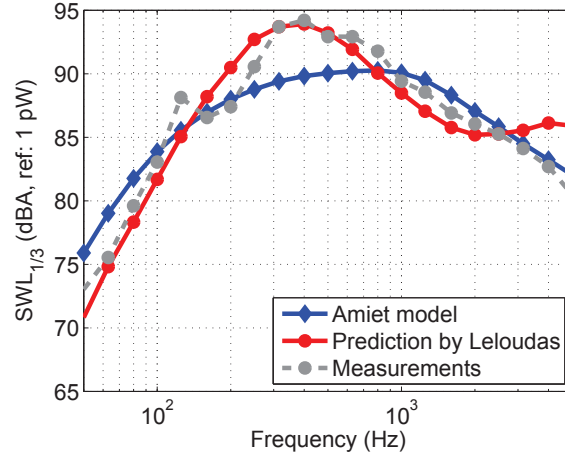
(b) Reference velocity $U_{ref} = 8\,m/s$, pitch angle is -2°, corresponding to AoA of 6°.

Figure 3.33: Third octave band spectrum of SWL predictions by Leloudas [18] using BPM model (red line), our calculations using Amiet's model (blue line) and measurements from [18].
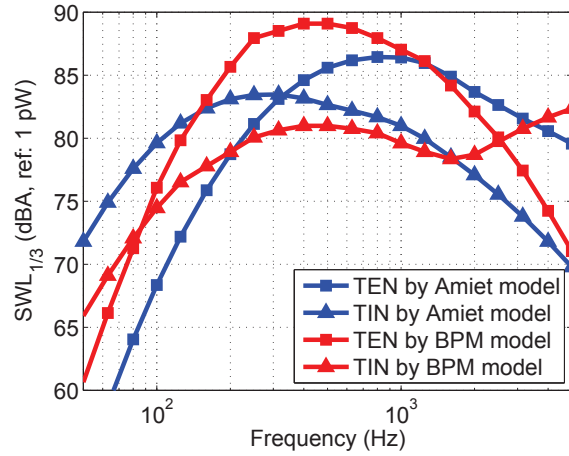
Figure 3.34: Third octave band spectrum of SWL for trailing edge noise and turbulent inflow noise. Blue lines: our predictions using Amiet's model; red lines: Leloudas calculations using BPM model.

3.5 Conclusions

Amiet's model for trailing edge noise and turbulent inflow noise are applied on a full size 2.3 MW wind turbine. We took into account rotation and Doppler effects using Schlinker and Amiet approach, and showed it is valid for the frequency range of interest. First validations are performed with simple cases where the wind speed is constant and no turbulent inflow noise is considered. Model predictions are compared to results from the literature for a 93 m-diameter 2.3 MW wind turbine. The sound power level predictions are in good agreement with measurements at high frequencies when the APG model is used, but underestimate them at low frequencies. The predictions of directivity and amplitude modulation are also in agreement with results from the literature for an observer close to a wind turbine, with maximum SPL and minimum AM strength downwind and upwind, while minimum SPL and maximum AM strength are found in crosswind directions.

Then we took into account wind shear and turbulence effects using the Monin-Obukhov similarity theory that is valid in the atmospheric surface layer over flat and homogeneous ground. On the one hand, we showed that wind shear causes variations of angle of attack that are largest in stable conditions (typically at night). Although the angle of attack variations due to wind shear produce a significant change in the wall pressure spectra at some blade segments, the increase in the trailing edge noise spectra at the far field receiver is almost negligible. On the other hand, turbulent inflow noise does vary significantly depending on atmospheric conditions. When both mechanisms are considered, SWL spectra are in much better agreement with measurements, with turbulent inflow noise dominating at

low frequency (below 400 Hz approximately). Directivities of overall SPL and AM are similar for both mechanisms and for the total noise, with an AM strength that reaches at most $4\,dB(A)$ for the total noise, compared to up to $10\,dB(A)$ for each mechanism considered individually.

Finally Amiet's model is compared with the semi-empirical BPM model for the constant wind speed cases. The semi-empirical model is able to predict separation noise. For case 2 ($U_{ref} = 8\,m/s$), when we consider the pitch angle configuration, the AoA increases which in turn leads to an increase of separation noise. This explains the measured spectral peak at around 400 Hz for case 2, and brings BPM results (both with our own boundary layer parameters and Leloudas' parameters) closer to the measurements. However for case 1 ($U_{ref} = 6\,m/s$), since the pitch angle configuration led to a decrease of AoA, there is no spectral peak observed in the measurement. In this case, our predictions are in better agreement with measurements than the BPM results. Thus we can suggest that Amiet's models are good candidates for wind turbine noise prediction, except that the separation noise is missing.

Several perspectives can be mentioned to improve the source model. It would be important to model separation/stall noise, that occurs when the AoA reaches large values. Recent studies have shown that this noise mechanism is a good candidate for explaining the enhanced amplitude modulation observed in the field [89]. Also, the effects of stronger wind shear and larger turbulence fluctuations could be studied, which would require to consider field measurements or theoretical tools that are more advanced than MOST.

Wind turbine noise propagation over a long distance

Contents

4.1   Introduction

The noise generated from the source is characterized by the noise emission level, while the noise received by an observer or a microphone is called noise immission level. These two quantities may be different in terms of magnitude and spectrum properties. These differences appear during the noise propagation. Wind turbine noise propagation in the atmosphere is influenced by many factors, such as refraction by vertical sound speed gradients, scattering by turbulence, reflection by the terrain (shape, impedance, etc) and atmospheric absorption. Prediction of sound propagation in the atmosphere can be a really challenging problem considering all these factors. In this chapter, we will focus mainly on the effect of ground reflection, atmospheric refraction and absorption, as well as the influence of these factors on the noise immission level. Also, we will check the validity of the point source

approximation that is commonly used in wind turbine noise immission models.

In Section 4.2, we present two propagation models that will be used in this chapter: an analytical model for sound propagation over an impedance ground and a parabolic equation method that takes into account the inhomogeneity of the atmosphere. The coupling between the source model and the parabolic equation code is not straightforward; it is detailed and validated in Section 4.3. Finally, in Section 4.4 the influence of ground reflection and meteorological effects is discussed and the validity of point source approximation is assessed.

4.2   Review of existing models

4.2.1   Analytical model for sound propagation over an impedance ground

Image source model

Like a light beam, a sound wave will be reflected when it encounters a ground. The total immission level is then the sum of a direct wave and a reflected wave, as shown in Figure 4.1. The image source model computes the total noise level by considering the sum of the two wave contributions. The main advantage of this model is that it is fast and simple to implement. On the other hand, the shortcomings are: it considers a specular reflection only (flat terrain); the variation of wind shear thus the effective vertical sound speed cannot be included.
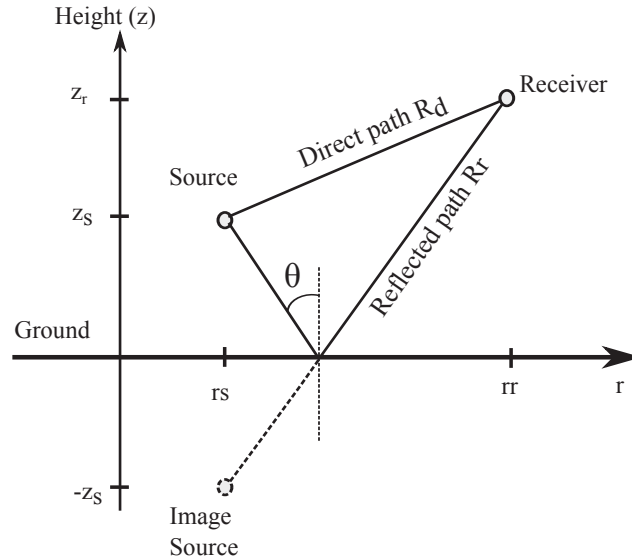
Figure 4.1: Illustration of the image source model with direct and reflected paths.

If we write the complex pressure amplitude at a receiver as [92, 35]:

$$p_c = S\left(\frac{\exp(ikR_d)}{R_d} + Q\frac{\exp(ikR_r)}{R_r}\right), \tag{4.1}$$

with S the amplitude of the complex pressure p_c, then it can be shown that the relative sound pressure level ΔL has the form [35]:

$$\Delta L = 10\log_{10}\left|\frac{p_c}{p_{FF}}\right|^2 = 10\log_{10}\left|1 + Q\frac{R_d}{R_r}\exp(ikR_r - ikR_d)\right|^2, \tag{4.2}$$

where R_d and R_r are the distances of the direct and reflected path respectively, Q is the spherical-wave reflection coefficient, and $p_{FF} = S\exp(ikR_d)/R_d$ is the free-field pressure. Q is defined as [35]:

$$Q = 1 - 2\frac{k}{Z}\frac{R_r}{\exp(ikR_r)}\int_0^\infty \exp(-\frac{qk}{Z})\frac{\exp(ik\sqrt{r^2 + (z_r + z_s + iq)^2})}{\sqrt{r^2 + (z_r + z_s + iq)^2}}\,dq, \tag{4.3}$$

with Z the normalized ground impedance, and z_r and z_s the receiver and source heights respectively. In practice, if we have $R_r \gg z_r + z_s$, then Equation (4.3) can be simplified as [92, 35]:

$$Q = R_p + (1 - R_p)F(d), \tag{4.4}$$

where R_p is the plane-wave reflection coefficient given by:

$$R_p = \frac{Z\cos(\theta) - 1}{Z\cos(\theta) + 1}, \tag{4.5}$$

θ is the reflection angle as shown in Figure 4.1, and $F(d)$ is the boundary loss factor given by:

$$F(d) = 1 + id\sqrt{\pi}\exp(-d^2)\operatorname{erfc}(-id), \tag{4.6}$$

with d the numerical distance defined as:

$$d = \sqrt{\frac{ikR_r}{2}}\left(\frac{1}{Z} + \cos(\theta)\right). \tag{4.7}$$

Approximating spherical wave reflection coefficient Q using Equation (4.4) is validated in Figure 4.2. The source height is 80 m, observer height is 2 m, and the propagation distance is 500 m, thus $R_r = 500\,m \gg z_r + z_s = 80\,m$. Ground is grassland with $\sigma_e = 200kPa\cdot s\cdot m^{-2}$. The relative SPL calculated by Equation (4.3) and (4.4) are almost identical.

Q depends on the normalized ground impedance Z. There exists many models for estimating ground impedance Z [93, 94, 95]. In this study, we will use an empirical model proposed by Delany and Bazley [93] that considers a single parameter σ_e, the effective flow resistivity. For a rigid ground, there is no energy lost when the sound wave is reflected, thus σ_e is infinite, while for a typical grassland, σ_e has a value of $200kPa \cdot s \cdot m^{-2}$. Spherical-wave reflection coefficient Q varies with frequency, this means the reflected wave can be a reinforcement or a subtraction
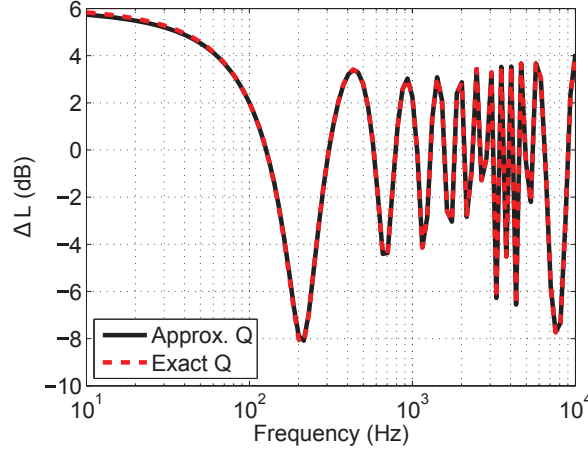
Figure 4.2: Validation of spherical wave reflection coefficient approximation. Source height is 80 m, observer height is 2 m, and the propagation distance is 500 m.

to the direct wave at the receiver depending on the acoustic wavelength and the distance of R_d and R_r. When the direct and reflected wave are out of phase, an interference dip is present in the spectrum.

Examples of ΔL for a receiver located at 2 m height, 1000 m away from the source are shown in Figure 4.3. In (a), 3 source heights are considered for a typical grassland ground. We can see that the number of interference dips increases with source height. In (b), the source height is fixed at 80 m, and grounds with various σ_e are compared which also has an influence on the interference dips.

Atmospheric absorption model

Atmospheric absorption is due to the dissipative process during the wave propagation. Energy loss leads to a decrease of the amplitude of the wave. The strength of absorption depends on frequency, temperature and the humidity of the atmosphere. If we include a small imaginary term ik_i in the wave number k, the complex acoustic pressure becomes:

$$p_a = S \frac{e^{ikr}}{r} e^{-k_i r}. \tag{4.8}$$

The factor $\exp(-k_i r)$ represents the exponential decrease of the amplitude with distance r [35]. If we use expression $k_c = k + ik_i$ to replace k in Equation (4.1), we have:

$$p_a = S \left[\frac{e^{ikR_d} \cdot e^{-k_i R_d}}{R_d} + Q \frac{e^{ikR_r} \cdot e^{-k_i R_r}}{R_r} \right]. \tag{4.9}$$

If we assume $R_r \simeq R_d$, then the decreasing component $e^{k_i R_d} \simeq e^{k_i R_r}$, we have:

$$p_a \simeq e^{-ikR_d} S \left[\frac{e^{ikR_d}}{R_d} + Q \frac{e^{ikR_r}}{R_r} \right] = e^{-ikR_d} p_c. \tag{4.10}$$
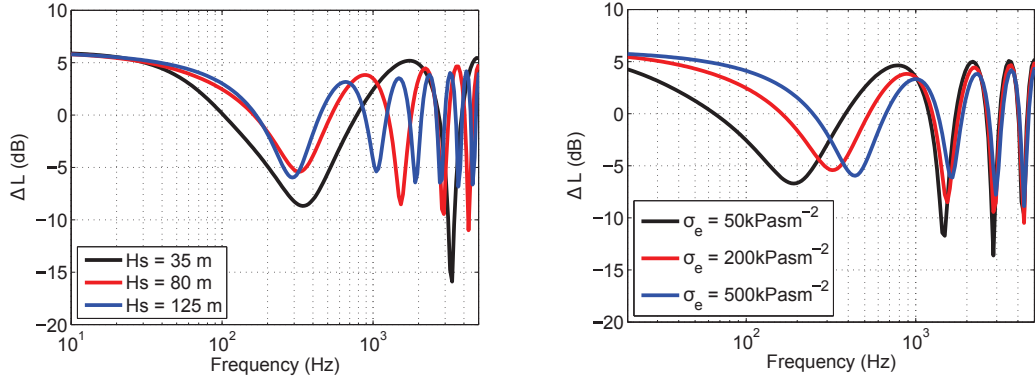
(a) Spectrum of ΔL for various source heights over a typical grassland.

(b) Spectrum of relative SPL ΔL for various types of ground; source height is 80 m.

Figure 4.3: Examples of narrowband spectrum of relative sound pressure level ΔL for (a) various source-observer locations and for (b) various ground types using the Delany-Bazley model.

Expressed in dB scale, we have [35]:

$$SPL = SWL - 10\log_{10}(4\pi R_d^2) - \alpha R_d + \Delta L, \quad (4.11)$$

where $SWL - 10\log_{10}(4\pi R_d^2)$ corresponds to the SPL in the free field, and α is called the atmospheric absorption coefficient (in dB/m). It can be estimated by the International Standard ISO 9613-1:1993 with the information of temperature and air humidity [35]. Atmospheric absorption is more pronounced at high frequency range, and for longer source-receiver distance. An example of absorption coefficient as a function of frequency is shown in Figure 4.4, with temperature of $20\,C^o$ and air humidity of 80 %. Note that we do not include the absorption due to clouds. Baudoin *et al.* [96] showed that the cloud absorption can be several orders of magnitude greater than standard absorption.

4.2.2 Parabolic equation method for sound propagation in an in-homogeneous atmosphere

4.2.2.1 Parabolic approximation of the Helmholtz equation

We start with 2D Helmholtz equation reduced from the 3D equation by axial symmetry assumption [35, 97]:

$$\left[\frac{\partial^2}{\partial x^2} + \left(\frac{\partial}{\partial z^2} + k^2\right)\right] q_c = 0, \quad (4.12)$$

where $q_c = p_c\sqrt{x}$ links the quantity q_c and the complex pressure p_c. x is along the propagation direction, and z along the vertical direction. The wavenumber k is
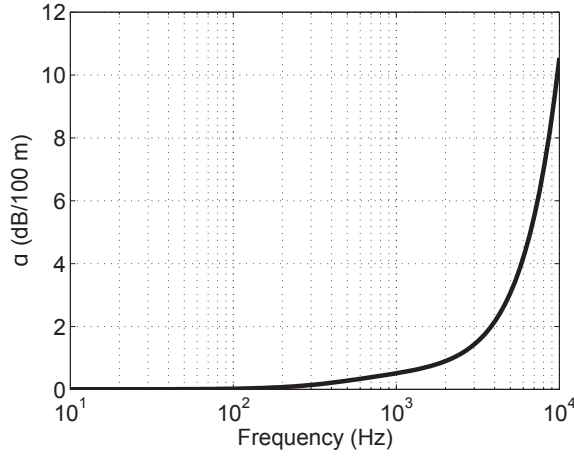
Figure 4.4: Atmospheric absorption coefficient α for temperature of $20\,C^o$ and air humidity of $80\,\%$.

allowed to vary with z to account for sound speed vertical gradients. We sometimes write $k^2 = k_a^2 n^2$ [98], where $n = c_0/c(z)$ is the index of refraction and k_a is a reference value of k, or a value at the ground surface [35, 97]. If we define the operator H_c as:

$$H_c = \left(\frac{\partial}{\partial z^2} + k^2 \right),$$
(4.13)

then Equation (4.12) becomes:

$$\left(\frac{\partial}{\partial x} + i\sqrt{H_c} \right) \left(\frac{\partial}{\partial x} - i\sqrt{H_c} \right) q_c = 0.$$
(4.14)

Here we consider only the outgoing wave, thus:

$$\left(\frac{\partial}{\partial x} - i\sqrt{H_c} \right) q_c = 0.$$
(4.15)

We define

$$s = \frac{1}{k_a^2} \left(\frac{\partial^2}{\partial z^2} + k^2 \right) - 1,$$
(4.16)

thus

$$\sqrt{H_c} = k_a \sqrt{\frac{1}{k_a^2} \left(\frac{\partial^2}{\partial z^2} + k^2 \right) - 1 + 1} = k_a\sqrt{s+1}.$$
(4.17)

Substituting it into Equation (4.15), we have:

$$\frac{\partial q_c}{\partial x} = ik_a\sqrt{1+s}q_c.$$
(4.18)

We seek solutions of q_c in the form:

$$q_c(x,z) = \psi(x,z)\exp(ik_a x),$$
(4.19)

In expression (4.19), the exponential term represents a plane wave oscillation, which varies much faster than $\psi(x, z)$. Substituting expression (4.19) into Equation (4.18), we obtain:

$$\frac{\partial \psi}{\partial x} = ik_a \left(\sqrt{1+s} - 1 \right) \psi. \tag{4.20}$$

If we approximate the square-root operator by the 1st order Taylor expansion:

$$\sqrt{1+s} \simeq 1 + s/2, \tag{4.21}$$

we have:

$$\frac{\partial \psi}{\partial x} = \frac{1}{2} ik_a s\psi = \frac{i}{2k_a} \left[\frac{\partial^2}{\partial^2 z} + (k^2 - k_a^2) \right] \psi. \tag{4.22}$$

Equation (4.22) is called the narrow-angle parabolic equation, because it is accurate only at small elevation angles (about 10°). A more accurate expression is proposed by Gilbert and White [99] using a Padé (1,1) approximation:

$$\sqrt{1+s} \simeq \frac{1 + \frac{3}{4}s}{1 + \frac{1}{4}s}. \tag{4.23}$$

With this approximation, a corresponding wide-angle parabolic equation (WAPE) is written as:

$$(1 + \frac{1}{4}s)\frac{\partial \psi}{\partial x} = \frac{1}{2} ik_a s\psi. \tag{4.24}$$

This expression is now valid up to an elevation angle of $30 - 40^o$ [98].
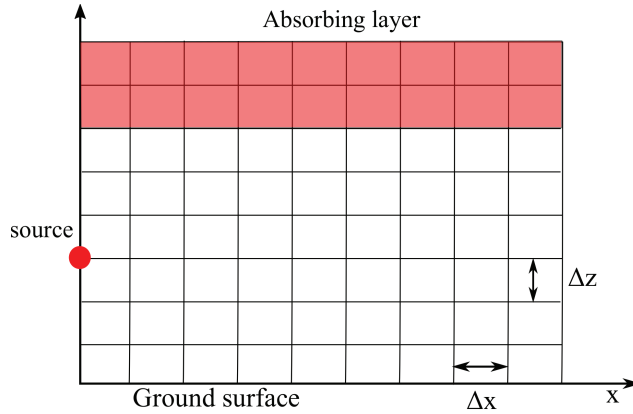
Figure 4.5: Illustration of calculation domain for PE method. Horizontal spacing is Δx and vertical spacing is Δz. Ground surface is at $z = 0$, and propagation direction is along x.

4.2.2.2 Numerical solution

A calculation domain is illustrated in Figure 4.5. Narrow-angle and wide-angle parabolic equations can be solved numerically by approximating the partial differential terms $\partial \psi / \partial x$ and $\partial^2 \psi / \partial z^2$ with appropriate numerical schemes [99]. We can

re-write the narrow-angle parabolic equation (4.22) as:

$$\frac{\partial \psi}{\partial x} = \alpha_p \frac{\partial^2 \psi}{\partial z^2} + \beta_p \psi, \tag{4.25}$$

with $\alpha_p = 1/2i/k_a$ and $\beta_p = 1/2i(k^2 - k_a^2)/k_a$. If the 2nd order differential term $\partial^2 \psi / \partial z^2$ is approximated by central differential formula as [99]:

$$(\frac{\partial^2 \psi}{\partial z^2})_{z_j} = \frac{\psi_{j+1} - 2\psi_j + \psi_{j-1}}{(\Delta z)^2}, \tag{4.26}$$

where $z_j = j\Delta z$ represents the vertical grid with the grid index $j - 1, j, j + 1$ etc. Then the Equation (4.25) can be written in matrix form as:

$$\frac{\partial}{\partial x} \vec{\psi} = (\gamma T + D)\vec{\psi}, \tag{4.27}$$

with $\vec{\psi}$ is the vertical grid vector, T and D are matrix given in [99]. The integration of Equation (4.27) from x to $x + \Delta x$ in the propagation direction gives:

$$\vec{\psi}(x + \Delta x) - \vec{\psi}(x) = (\gamma T + D) \int_{x}^{x+\Delta x} \vec{\psi} \, dx. \tag{4.28}$$

The Crank Nicholson approximation is now used to replace the integral in Equation (4.28) by $[\vec{\psi}(x + \Delta x) + \vec{\psi}(x)]\Delta x/2$. Thus Equation (4.28) becomes:

$$M_b \vec{\psi}(x + \Delta x) = M_a \vec{\psi}(x), \tag{4.29}$$

where M_a and M_b are given as [99]

$$M_a = 1 + \frac{1}{2}\Delta x (\gamma T + D)$$
$$M_b = 1 - \frac{1}{2}\Delta x (\gamma T + D). \tag{4.30}$$

For wide-angle parabolic equation (4.24), a similar form as expression (4.29) can be found [99], with:

$$M_a = 1 + \frac{1}{2}\Delta x (\gamma T + D) + \frac{\gamma T + D}{2ik_a}$$
$$M_b = 1 - \frac{1}{2}\Delta x (\gamma T + D) + \frac{\gamma T + D}{2ik_a}. \tag{4.31}$$

This method is called the Crank-Nicholson PE (CNPE) method. It is 2nd order accurate and implicit since a tridiagonal matrix needs to be inverted at each step. If higher elevation angles are needed in the calculation, it is possible to use the Split-step Padé method of order n, introduced by Collins [100] and detailed by Dragna [98]. In the rest of this Chapter, only the wide-angle parabolic equation will be considered. It will simply be referred to as PE.

4.2.2.3 Boundary conditions on the ground and on the top

On the ground surface, the boundary condition is:

$$\frac{\partial p_c}{\partial z}|_{z=0} + ik_a B p_c = 0, \tag{4.32}$$

where $B = 1/Z$ with Z the normalized impedance. The same relationship holds for ψ too, thus we have $\frac{\partial \psi}{\partial z}$ at horizontal step $n\Delta x$ written as:

$$\frac{\partial \psi}{\partial z}|_{z=0}(n\Delta x) + ik_a B \psi(n\Delta x) = 0, \quad n = 1, 2, 3... \tag{4.33}$$

A second order approximation for ψ is preferable for wide-angle parabolic equation. A fictious point $\psi_0(n\Delta x)$ at $z = -\Delta z$ is introduced for a 2nd order centered scheme. The expression is given in [98] as:

$$\frac{\psi_2 - \psi_0}{2\Delta z} + ik_a B \psi_1 = 0, \tag{4.34}$$

which gives the value of ψ_0. This modifies the first line of matrix given in Equation (4.31).

For the upper limit of the grid, an artificial absorbing layer is applied to avoid the back reflection of the sound waves. The way to add this layer is to damp the wave number k by adding an imaginary term. There is no unique form for this imaginary term [99]. In this study, we use the expression given in the form:

$$\exp\left[-\frac{1}{C_\alpha}\left(\frac{z - z_\alpha}{z_{max} - z}\right)^2\right], \tag{4.35}$$

with C_α a coefficient determined empirically, z_α the starting height of the absorbing layer and z_{max} the maximum height of the calculation domain.

4.2.2.4 Starting fields

Analytical starters

The parabolic equation at step x_{j+1} is solved with the known values of $\psi(x_j)$. Thus initial values of $\psi(x_0)$ that represent a monopole source are required. However, the exact expression for monopole source is not suitable because:

1. it diverges at the source;

2. it radiates energy at large elevation angles (angles between the horizontal direction and the wave propagation direction) that are outside the range where the PE method is accurate [35].

Thus a spatial Gauss function is used for the starting field for narrow-angle parabolic equation [101, 99]:

$$q_c(0, z) = \sqrt{ik_a} \exp(-\frac{1}{2}k_a^2 z^2). \tag{4.36}$$

As for the wide-angle parabolic equation, a higher order starting field is preferred. The expression is given in [35] as:

$$q_c(0, z) = \sqrt{ik_a}(A_0 + A_2 k_a^2 z^2) \exp(-\frac{k_a^2 z^2}{3}), \tag{4.37}$$

with $A_0 = 1.3717$, $A_2 = -0.3701$.

Numerical starters

Another way to find the starting field is called the back-propagation method, first proposed by Collins and Westwood [102]. The idea is (see Figure 4.6)

1. to calculate the analytical starter (initial starter) at a certain distance from the source for a homogeneous atmosphere using Amiet's source model;

2. back-propagate the starter by PE method till the source to obtain the 'source-starter'; (Note that it requires some modification of signs for using the PE method in a backwards propagation direction)

3. to forward propagate the 'source-starter' using classic PE method for an in-homogeneous atmosphere. This method can be used when the source is not a monopole (more complex directivity).

It is needed to note that during back-propagation, the ground is always chosen as rigid, to maintain a stable calculation. To validate this approach, the relative sound pressure level ΔL for a monopole source is calculated with the 2nd order analytical starter given by Equation (4.37) and with the back-propagation method. It is compared to the analytical solution given by Equation 4.2 in Figures 4.7 to 4.10 in the vertical and horizontal directions, and for rigid and impedance grounds. For the back-propagation case, the initial starter is set 100 m away from the source using the analytical solution of Equation 4.2. In the vertical direction, we can see that the two starters give relatively close results compared to the analytical solution until around 200 m height. In the horizontal direction, after about 150 m propagation distance, the back-propagation method gives slightly better results, but the two starters remain in good agreement with the analytical solution. The back-propagation method remains accurate with an impedance ground even though a rigid ground is used during the back-propagation phase.
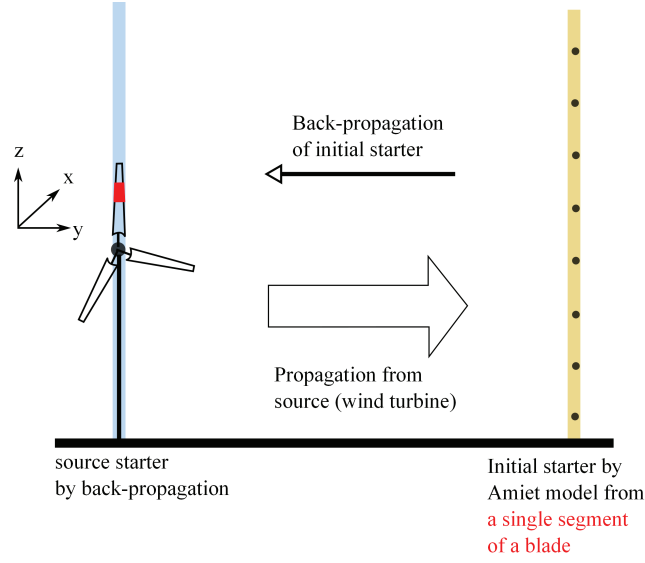
Figure 4.6: Illustration of the back-propagation method to obtain the initial starter due to a single segment of a blade (in red).

4.3 Coupling of wind turbine source model with parabolic equation code

4.3.1 Coupling procedure

We studied two ways to couple the Amiet's source model to the PE code. The first one is to calculate the starting field from the whole wind turbine at geometric near field (typically $100\,\text{m}$), then propagate it to the far field (see Figure 4.11 (a)). This way is rather fast to do, since we need to perform only one PE calculation per frequency. However this method leads to errors because it assumes phase correlations between segments, which is in contradiction with the model presented in Chapter 3. The 2nd way is to use the back-propagation technique explained before for each segment of each blade (see Figure 4.11 (b)). One PE calculation is performed for each segment individually, then all contributions are summed up at the receiver location. This makes the complete calculation quite computationally intensive. Also, each PE calculation is performed in a slightly different two-dimensional plane, thus it is strictly exact only at the chosen observer location.

To couple the PE method to Amiet's source model, it is essential to find the starting field. For the specific application of wind turbine noise propagation, we intend to use results of S_{pp} from Amiet's model to deduce the starter field q_c. It is possible to obtain the magnitude of this 2D variable q_c as:

$$q_c = p_c\sqrt{x} = \sqrt{S_{pp}} \cdot \sqrt{x}. \tag{4.38}$$

(a) Source at 2 m height. (b) Source at 80 m height.
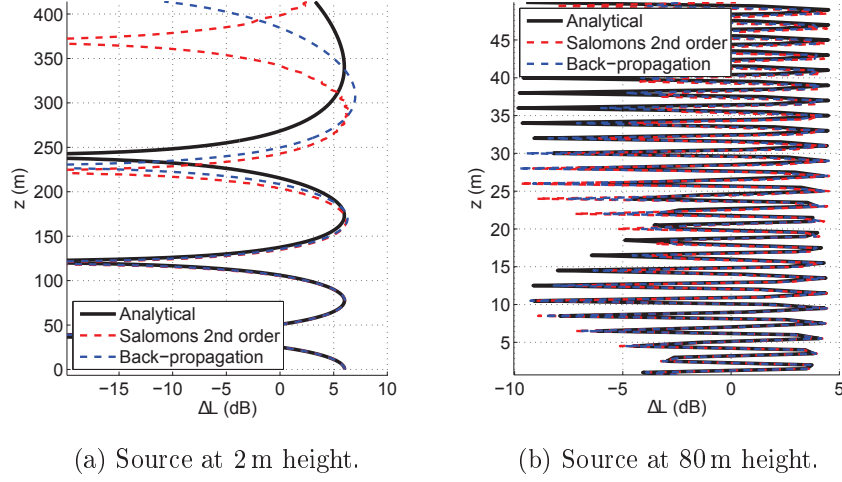
Figure 4.7: Relative sound pressure level for a monopole source calculated with different starting fields and compared to the analytical solution. Source height is (a) 2 m, (b) 80 m. Receiver is 300 m away from the source. Frequency is 340 Hz, and ground is rigid.
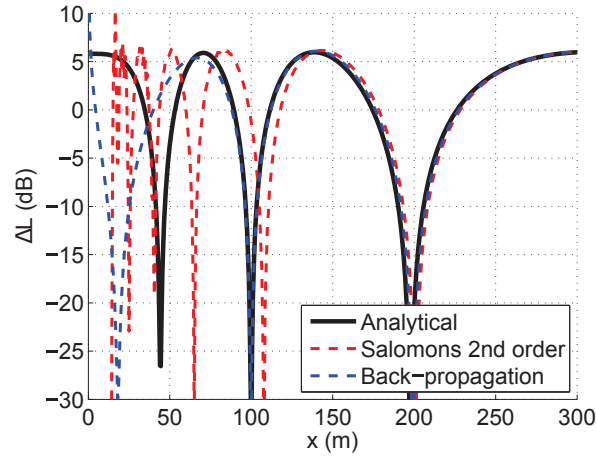
Figure 4.8: Relative sound pressure level for a monopole source calculated with different starting fields and compared to the analytical solution. Source height is 80 m, receiver height is 2 m. Frequency is 340 Hz, and ground is rigid.

(a) Source at 2 m height.

(b) Source at 80 m height.
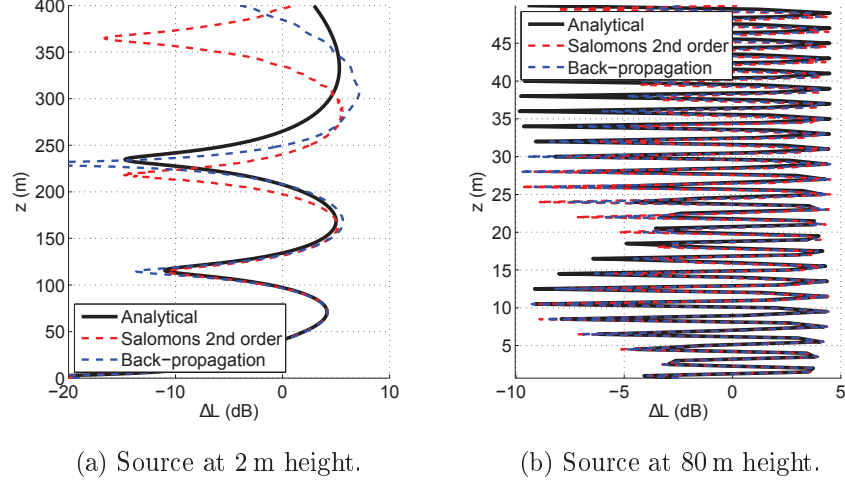
Figure 4.9: Relative sound pressure level for a monopole source calculated with different starting fields and compared to the analytical solution. Source height is (a) 2 m, (b) 80 m. Receiver is 300 m away from the source. Frequency is 340 Hz, and a grass ground is considered with $\sigma_e = 200 kPa \cdot sm^{-2}$.
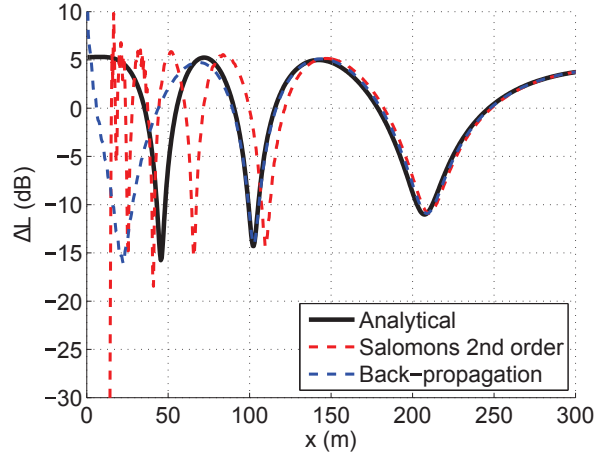
Figure 4.10: Relative sound pressure level for a monopole source calculated with different starting fields and compared to the analytical solution. Source height is 80 m, receiver heigth is 2 m. Frequency is 340 Hz, and a grass ground is considered with $\sigma_e = 200 kPa \cdot sm^{-2}$.

(a) Only one PE calculation.

(b) One PE calculation for each segment.

Figure 4.11: Illustration of the two methods considered for the coupling between source and propagation models.

Third octave band central frequency (Hz)	100	125	160	200	250	315	400
Number of narrow band calculations	1	1	1	2	2	3	4
Third octave band central frequency (Hz)	500	630	800	1000	1250	1600	2000
Number of narrow band calculations	4	4	5	5	5	6	6

Table 4.1: Number of narrowband calculations per third octave band.

We assume the sources along the blades are uncorrelated, however, we need to account for the geometric phase differences due to the differences of each segment-receiver distance R_{str}. To recover this phase information, we introduce a correction term by multiplying the 2D complex starting field q_c by $e^{ikR_{str}}$. Then the corrected q_c with the phase information for each segment is back-propagated to the wind turbine. Finally all the sources are propagated forward using classical PE method to an observer, and the received total SPL is simply the sum of all the contributions. We must emphasize that since for each segment, the propagation distance and direction are different, this method is strictly valid only at one receiver location. However, we will show in the following that it remains accurate over a large range of distances.

In the following sections, all the PE calculations are done for 49 frequencies (see Table 4.1) in order to obtain the 1/3 octave band spectrum between 100 Hz and 2000 Hz. The size of the domain is 1000 m along x and 500 m along z, with $\Delta x = \Delta z \simeq \lambda/10$.

4.3.2   Validations against analytical propagation model for a homogeneous atmosphere

The PE method coupled with Amiet's model is validated with analytical model in this section. The back-propagation distance is set as 100 m for all cases. Validations are first done for 3 tip segments under homogeneous atmospheric condition for rigid

and impedance grounds respectively, and then for the whole wind turbine with rigid ground.

4.3.2.1 Validations with 3 tip segments against analytical model

Homogeneous atmosphere with rigid ground

In this part, the validation is done considering only 3 tip segments, with blade parameter $\beta = 0^o$, meaning one blade is pointing upwards. Ground is rigid ($\sigma_e = \infty$). In Figure 4.12, the narrow band spectra are compared for an observer at (a) 2 m and (b) 10 m height. In both cases, the propagation distances are 1000 m from the wind turbine in the downwind direction. The PE results capture well the interference dips for the whole frequency range considered, although the magnitude is less than the analytical solution due to numerical errors. Small over-predictions can also be observed for certain frequencies, but they remain low (1 - 2 dB).

(a) Observer at 2 m height.   (b) Observer at 10 m height.

Figure 4.12: Narrow band spectra comparisons between analytical solution and PE results for observers located 1000 m away in the downwind direction, at (a) 2 m height and (b) 10 m height. Blade position parameter $\beta = 0^o$.

Figures 4.13 and 4.14 show the overall SPL (OASPL) as a function of receiver height and of propagation distance respectively. For both directions, there are about 1 dB overestimation by PE results. In the horizontal direction, results for observers at two different heights are shown. When the propagation distance is larger than the back-propagation distance, the predicted OASPL follows the analytical results with an overestimation less than 1 dB. Figure 4.14 shows that PE results are valid for a large range of distances between 200 m and 1000 m.
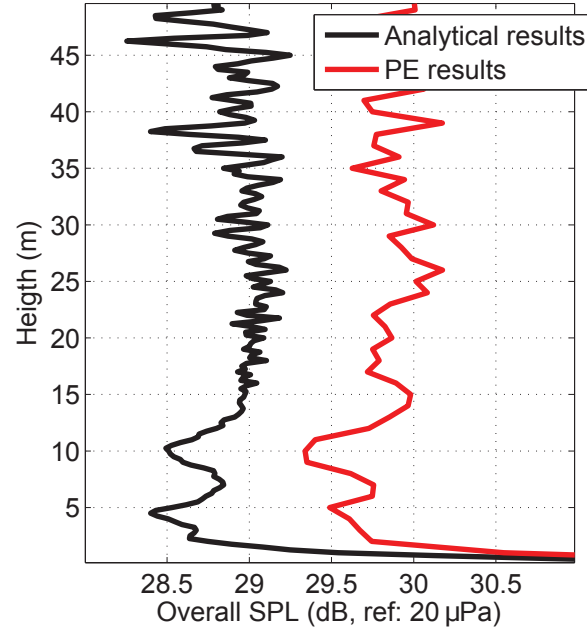
Figure 4.13: Overall SPL as a function of height. Observer is 1000 m away in the downwind direction. Blade position parameter $\beta = 0^o$.
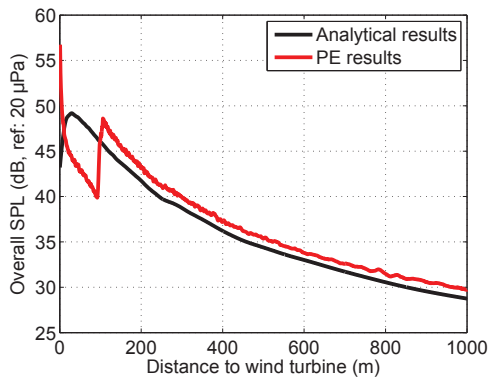
(a) Observer at 2 m height.
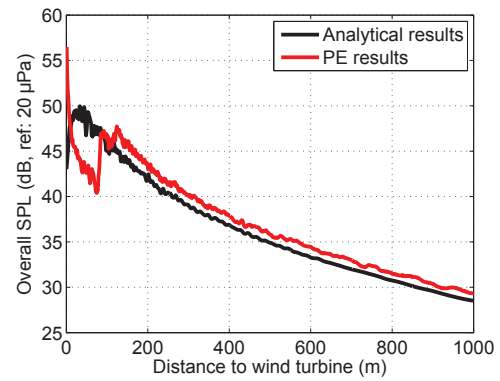
(b) Observer at 10 m height.

Figure 4.14: Overall SPL as a function of propagation distance (in the downwind direction) for a height of (a) 2 m height and (b) 10 m height. Blade position parameter $\beta = 0^o$.
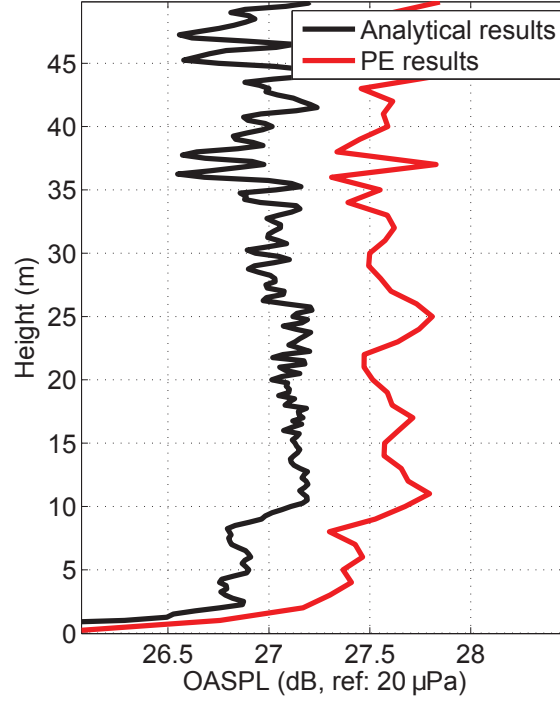
Figure 4.15: Comparison of overall SPL as a function of height for an impedance ground with $\sigma_e = 200kPasm^{-2}$ between analytical solution and PE results. Observer is 1000 m away in the downwind direction. Blade position parameter $\beta = 0^o$.

Homogeneous atmosphere with an impedance ground

Validations with an impedance ground are shown in this section considering again 3 tip segments and blade position $\beta = 0^o$. The ground type is grassland with $\sigma_e = 200\,kPa \cdot sm^{-2}$. Figure 4.15 shows the OASPL predicted by the analytical and PE models as a function of the receiver height at a propagation distance $R = 1000\,m$. The error between the two models is around 0.5-1 dB. In Figure 4.16, OASPL is plotted against propagation distance for an observer at 2 m height. It is clearly seen that when the propagation distance increases, the errors between analytical results and PE results decrease. The narrowband spectra plotted in Figure 4.17 explain this trend and show that even at 200 m and 500 m, PE predictions remain quite accurate.
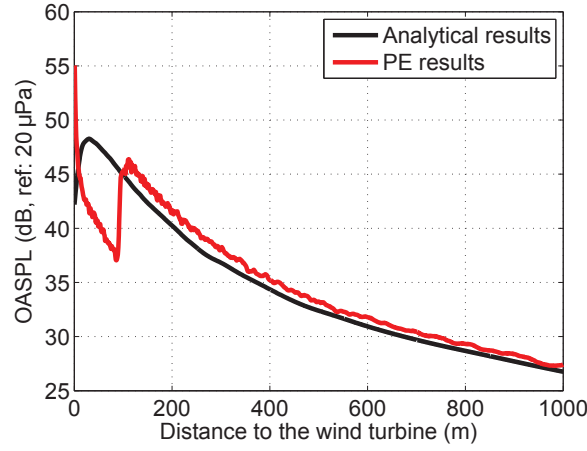
Figure 4.16: Comparison of overall SPL as a function of propagation distance for an impedance ground with $\sigma_e = 200 kPasm^{-2}$ between analytical solution and PE results. Observer is at 2 m height in the downwind direction. Blade position parameter $\beta = 0^o$.

4.3.2.2   Validations for the whole wind turbine over a rigid ground

Noise radiation along a blade

Field measurements show that most of wind turbine noise is generated near the tip part of a blade [3]. This is because near the root region, the relative velocity met by the blade is very small. When doing the propagation calculations, each source is propagated separately in order to maintain the phase information. This makes the whole calculation very heavy on a PC. One calculation over the whole frequency range takes about 3 hours. Thus the calculation with all 24 segments for a complete blade rotation (10 blade positions) along one propagation direction will take approximately 720 hours (30 days). In order to reduce the calculation time, the contribution of each segment to the total SPL is studied using the analytical model. The results are shown in Figure 4.18. We can see that the results with only the last 5 segments are really close to the full results (with 0.1-0.2 dB difference). Thus all the results shown below are calculated with the 5 outer segments only.

Figure 4.19 shows the comparisons of narrow band spectrum for a receiver located 1000 m away downwind, at (a) 2 m height and (b) 10 m height. When the observer is at 2 m height, a maximum overestimation of 1 dB is observed in the low frequency range (between 100 Hz to 800 Hz), while for an observer at 10 m height, the agreement is quite satisfying over the whole frequency range considered.

Figure 4.20 shows the OASPL calculated with analytical and PE models as a function of height. As in Figure 4.13 using the 3 tip segments, an overestimation of
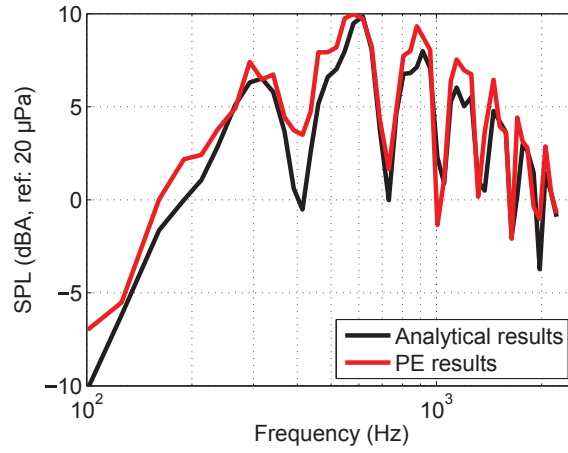
(a) Propagation distance R = 200 m.
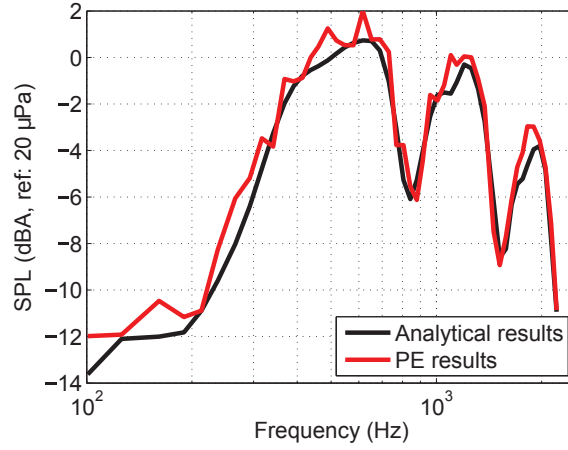
(b) Propagation distance R = 500 m.
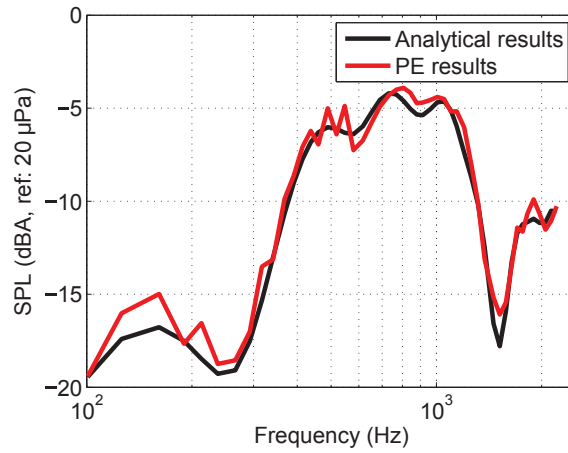
(c) Propagation distance R = 1000 m.

Figure 4.17: Narrowband spectrum comparisons between analytical results and PE results, for an observer at 2 m height, and for propagation distances of (a) 200 m, (b) 500 m and (c) 1000 m.
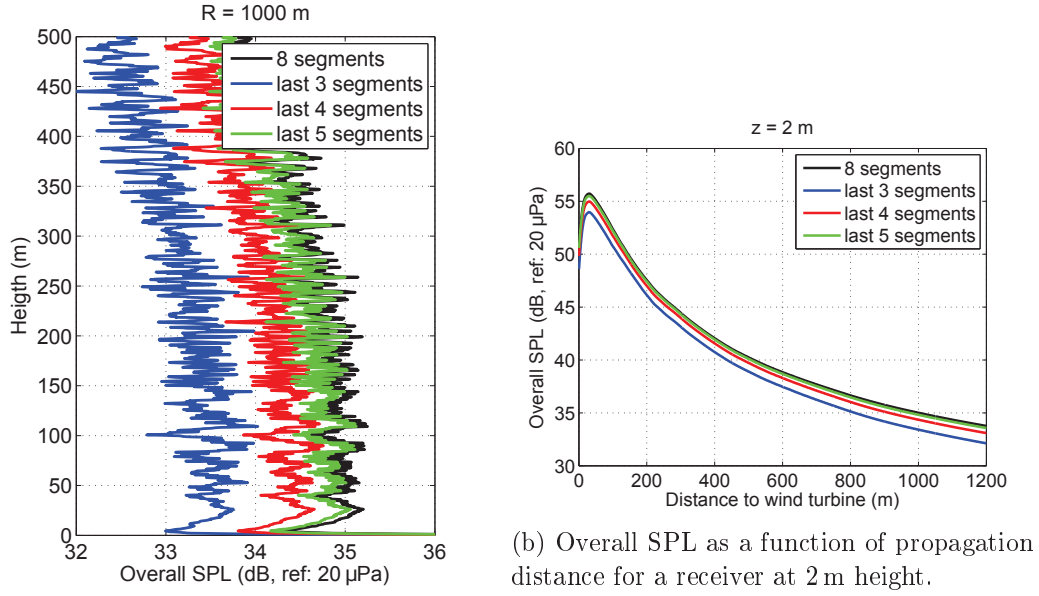
(a) Overall SPL as a function of height for a receiver at 1000 m in the downwind direction.

(b) Overall SPL as a function of propagation distance for a receiver at 2 m height.

Figure 4.18: Analytical results of OASPL from different segments contributions. Ground is considered as rigid.

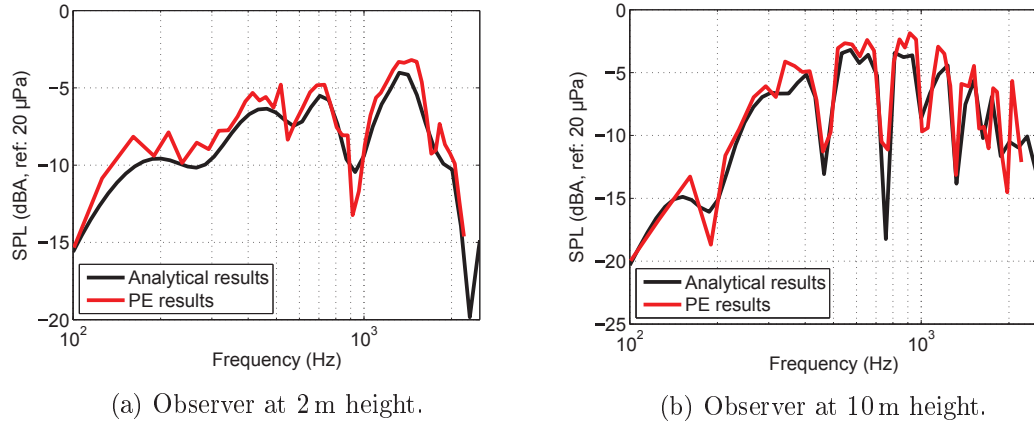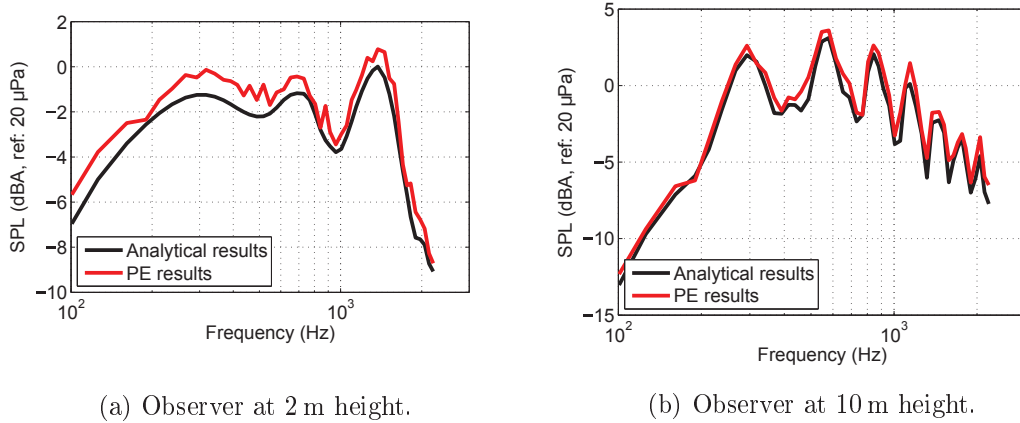(a) Observer at 2 m height.

(b) Observer at 10 m height.

Figure 4.19: Narrow band spectra comparisons between analytical solution and PE results for observers located in 1000 m away in the downwind direction, at (a) 2 m height and (b) 10 m height. Only the 5 outer segments of each blade are considered and the ground is rigid. Blade position parameter $\beta = 0^{o}$.
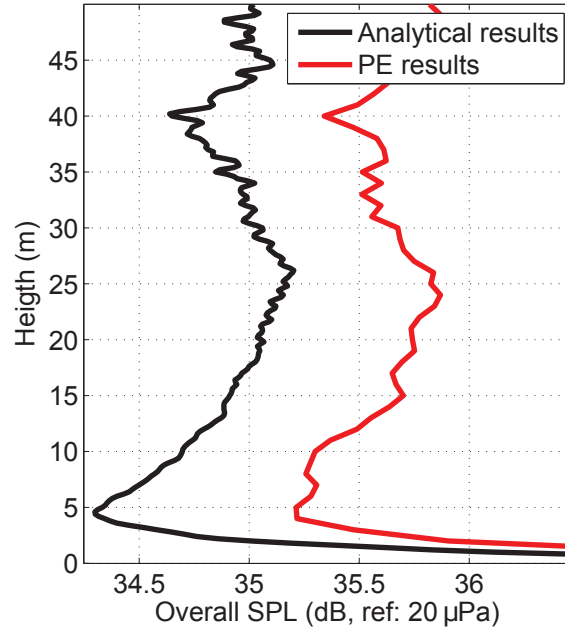
Figure 4.20: Overall SPL as a function of height. Observer is 1000 m away in the downwind direction. Only the 5 outer segments of each blade are considered and the ground is rigid. Blade position parameter $\beta = 0^o$.

1 dB is observed for all heights. In Figure 4.21, the OASPL is plotted as a function of propagation distance for two observer heights. The overestimation at 1000 m for the two observer heights is smaller than 1 dB. This is in agreement with the spectra plotted in Figure 4.19.

4.4 Results and discussions

4.4.1 Effect of ground reflection and atmospheric absorption

As explained before, sound wave is reflected when impeaching a ground surface. The immission level measured at a receiver is different than that measured in free field due to the influence of the reflected wave contribution. In this section, effects of ground reflection and atmospheric absorption on the SPL spectrum, amplitude modulation and the directivity are studied using the analytical model with a uniform wind profile of 8 m/s. Since a uniform wind profile is used, only trailing edge noise is considered. Receiver is located at 1.5 m height above ground for all distances, air temperature is set at 20^oC and the humidity at 80%.

Figure 4.22 shows the results of SPL spectrum for 4 receivers located at different distances in the downwind direction with consideration of ground reflection only

(a) Observer at 2 m height.

(b) Observer at 10 m height.
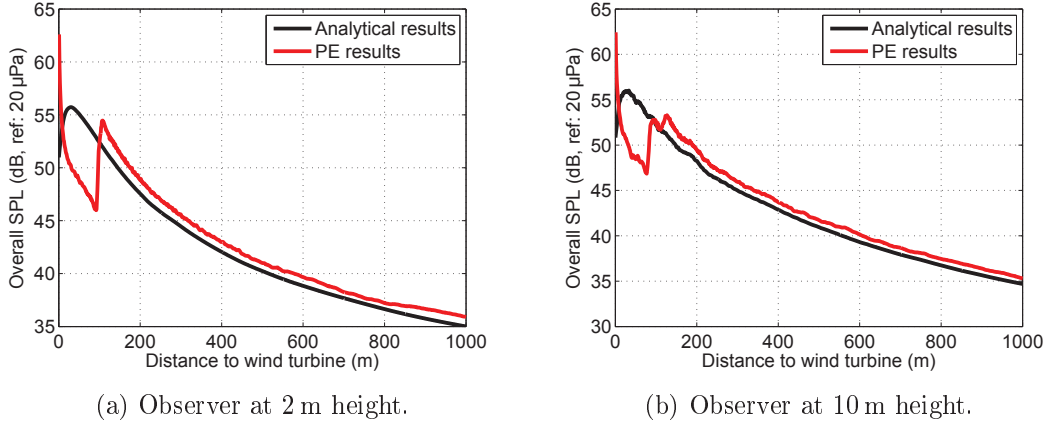
Figure 4.21: Overall SPL as a function of propagation distance (in the downwind direction) for a height of (a) 2 m height and (b) 10 m height. Only the 5 outer segments of each blade are considered and the ground is rigid. Blade position parameter $\beta = 0^o$.

(solid line), and the ground reflection and atmospheric absorption (dashed line). A typical grass ground with $\sigma_e = 200 kPa \cdot s \cdot m^{-2}$ is assumed. The results are the sum of all the segment contributions, thus the interference dips are much less pronounced as for only one segment in Figure 4.3. However, it is still clear that these less pronounced interference dips are shifted from around 80 Hz for $R = 100\,m$ to 300 Hz for $R = 1000\,m$. This shift is due to the fact that when the observer is further, the length difference between the direct wave path and reflected wave path is smaller, thus the destructive interference occurs at a smaller wavelength, meaning higher wave frequency. The dashed lines show that the atmospheric absorption is more pronounced at higher frequency and at a longer propagation distance.

Figure 4.23 shows the OASPL as a function propagation distance, considering (a) only ground reflection, (b) only atmospheric absorption, (c) the two effects. Ground reflection increases the overall SPL for all distances, due to the reflected wave contributions, while atmospheric absorption has a monotonic decreasing effect on the overall SPL. Combining the effects, when the observer is close to the wind turbine, ground reflection plays the main role, and the immission level is higher than in the free field; while when the observer is far from the wind turbine, immission level is lower than in the free field because the atmospheric absorption is dominant.

Figure 4.24 shows that a more rigid ground (with higher σ_e value) leads to a lower overall SPL at R = 1000 m, which seems at first counter intuitive. To explain this phenomenon, we plot the third octave band spectrum for the same σ_e values at R = 1000 m in Figure 4.25, and corresponding relative sound pressure level for a point source at 80 m height is already shown Figure 4.3(b). We can see clearly
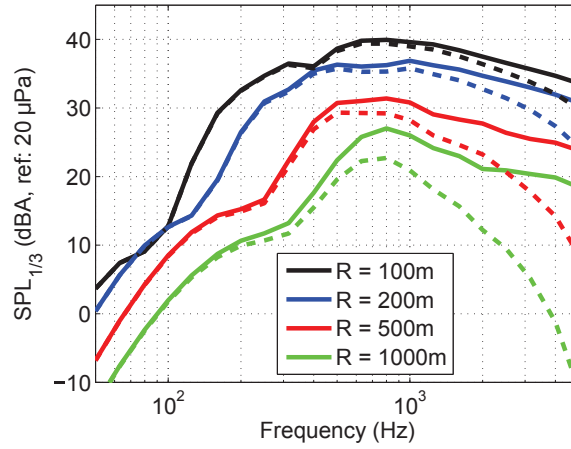
Figure 4.22: 1/3 octave band SPL spectrum for receivers located in downwind direction at different distances. Wind speed is 8 m/s. Solid lines: results with ground reflection only; dashed lines: results with ground reflection and atmospheric absorption.

that for a more rigid ground, the first interference dip occurs at higher frequency, which tends to reduce the total SPL more significantly when summing up all the frequency bands.

Figures 4.26- 4.27 show the effect of ground reflection and atmospheric absorption on the directivities of SPL and amplitude modulation strength. Observer is at 1000 m away from the wind turbine. In agreement with the results of Figure 4.24, at this distance in the downwind direction, the overall SPL with ground reflection and atmospheric absorption is around 5 dB lower than that of free field. For other observer directions, the similar reduction on the overall SPL due to ground reflection and atmosphere absorption are also observed. On the other hand, for amplitude modulation, the ground reflection and atmospheric absorption play no significant role for all directions τ.

The amplitude modulation strength for $\tau = 0^o, 45^o, 90^o$, and 105° as a function of source-receiver distance is shown in Figure 4.28. It is seen that when sound is propagating along downwind directions (0° and 45°), the strength of amplitude modulation increases with increasing distance but remains lower than 1 dB; while in the crosswind directions (90° and 105°), the strength tends to decrease with increasing distance.

To gain a little more understanding on the increase of amplitude modulation strength when considering ground reflection and atmospheric absorption, a spectrum of amplitude modulation strength is plotted in Figure 4.29 for a receiver at 1000 m in the crosswind direction. It shows large frequency variations when ground reflection and atmospheric absorption are taken into account, while for a free field,
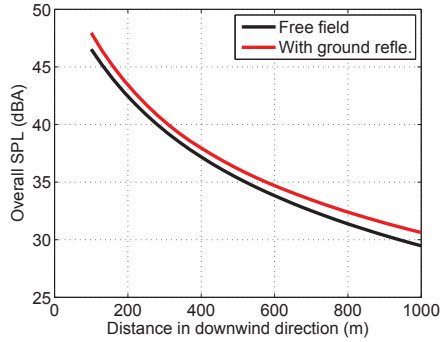
(a) Overall SPL considering ground reflection only.
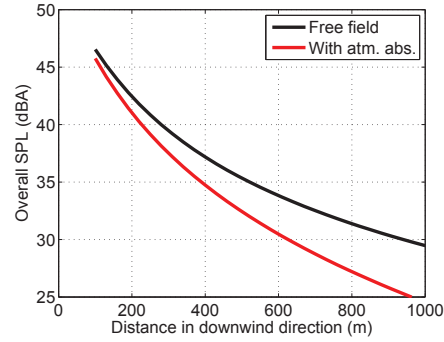
(b) Overall SPL considering atmospheric absorption only.
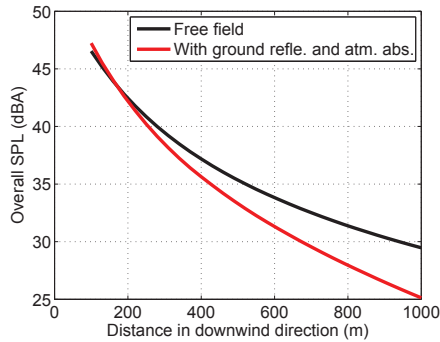
(c) Overall SPL considering both ground reflection and atmospheric absorption.

Figure 4.23: Overall SPL considering different effects. Observer is at 1.5 m height. Reference wind speed is 8 m/s. A grass ground is assumed.
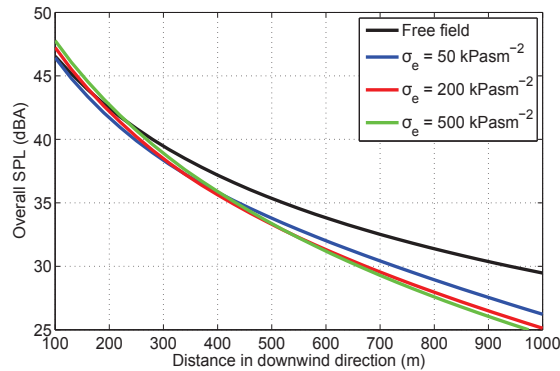
Figure 4.24: Overall SPL with respect to the propagation distance in downwind direction, for different fluid resistivity. Both ground reflection and atmospheric absorption are considered.
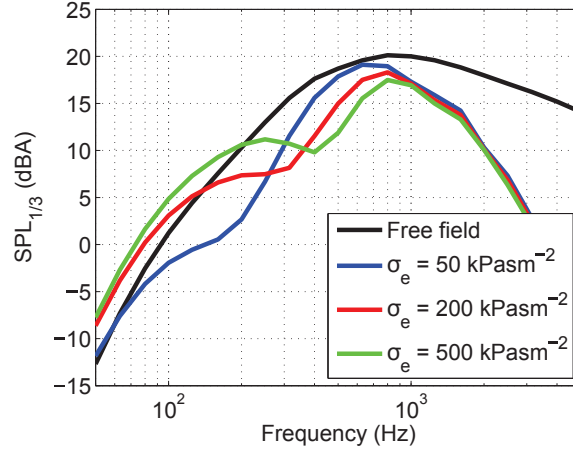
Figure 4.25: SPL spectrum for different fluid resistivity for an observer at R = 1000 m from the wind turbine.
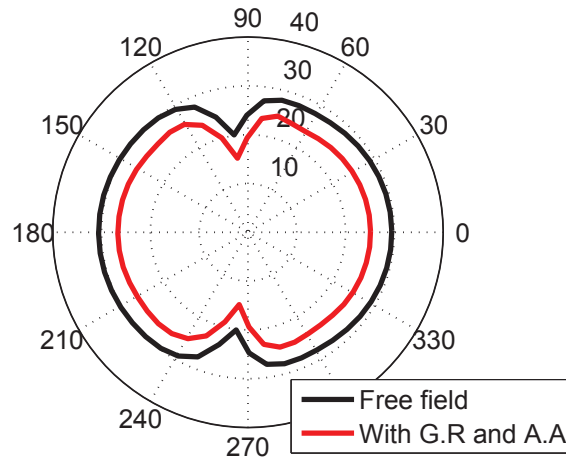
Figure 4.26: Directivity of overall SPL for free field and for a grassland with consideration of ground reflection and atmosphere absorption. Observer distance is 1000 from the wind turbine. $\sigma_e = 200 kPa \cdot s \cdot m^{-2}$.
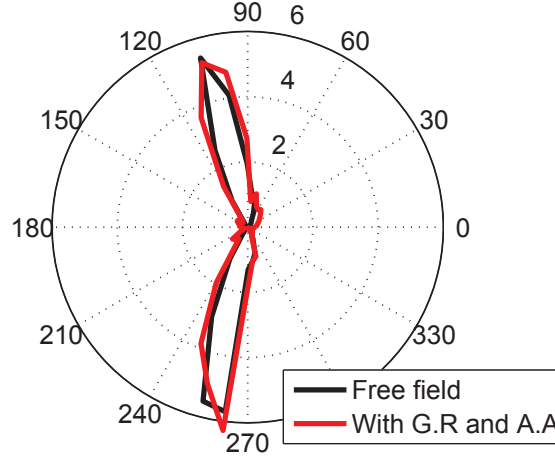
Figure 4.27: Directivity of amplitude modulation strength for free field and for a grassland with consideration of ground reflection and atmosphere absorption. Observer distance is 1000 from the wind turbine. $\sigma_e = 200 kPa \cdot s \cdot m^{-2}$.

the spectrum is quite smooth. If we focus on the third octave band 2000 Hz, by looking at the spectra of the blade positions that produce maximum and minimum SPL in Figure 4.30, the cause of the 10 dB amplitude modulation peak is seen to be the ground interference dip at this frequency. It is necessary to notice that for different frequencies, the blade positions for maximum and minimum SPL are not necessarily the same, thus the overall amplitude modulation strength is not simply the logarithm summation of the spectrum in Figure 4.29.

4.4.2   Meteorological effects on sound propagation in far field

In this part, we consider the propagation under inhomogeneous atmosphere conditions. Wind shear and atmospheric turbulence are considered in the source models as explained in Chapter 3, and only refraction effects due to wind shear are included in the propagation model. Atmospheric absorption is neglected here, although it could be included as in the analytical model. The wind profile with reference velocity $U = 8\,m/s$ and heat flux $H = -25W/m^2$ are chosen for the calculations. The effective wind speed profile is used for PE calculation: $c_{eff}(z) = c(z) + U(z) \cdot \cos\tau$, with $c(z)$ the sound speed, $U(z)$ the vertical wind profile and τ the ground azimuthal angle. Note that we ignore the temperature variation, thus $c(z) = c_0$. The effect of vertical temperature gradients was seen to be small in the PE calculations of Cotté et al. [103]. Grass ground with $\sigma_e = 200 kPa \cdot sm^{-2}$ is assumed. The initial starter calculated by Amiet's model is set at 100 m away from the wind turbine. Both trailing edge noise and turbulent inflow noise are considered.
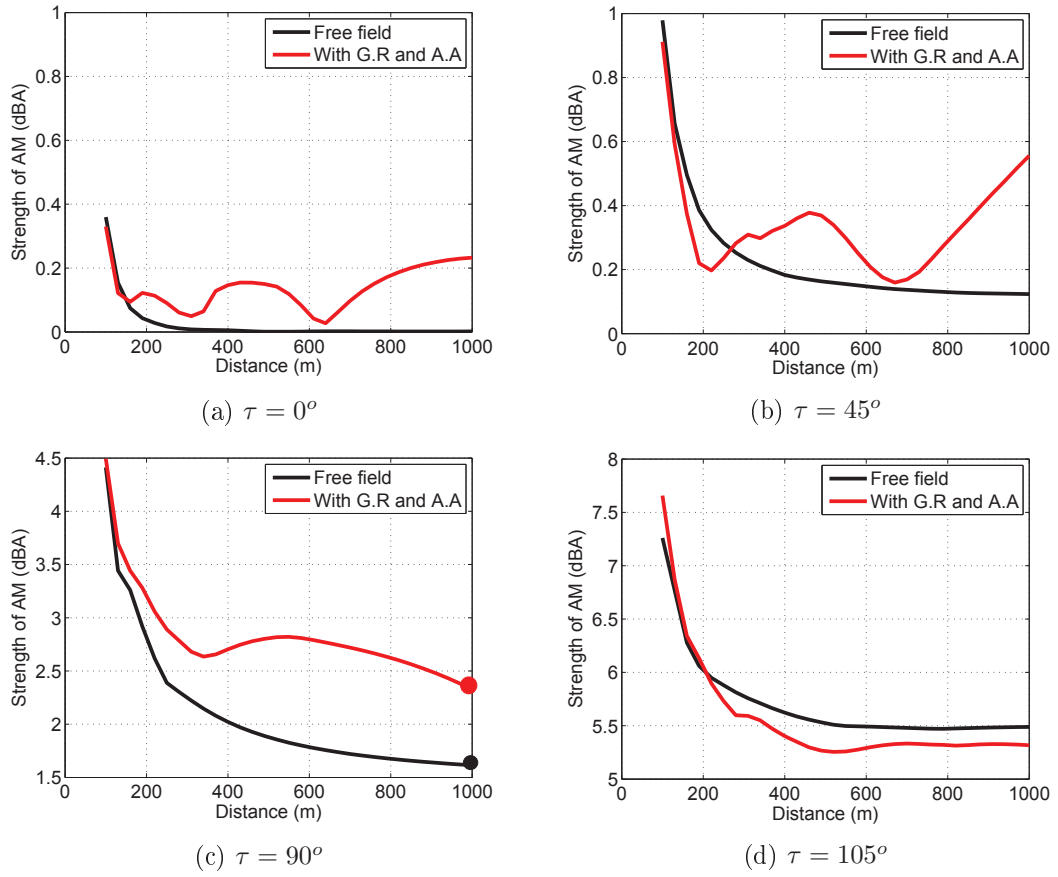
Figure 4.28: Amplitude modulation strength with respect to propagation distance for observer direction $\tau = 0^o, 45^o, 90^o$ and 105°. $\sigma_e = 200 kPa \cdot s \cdot m^{-2}$.
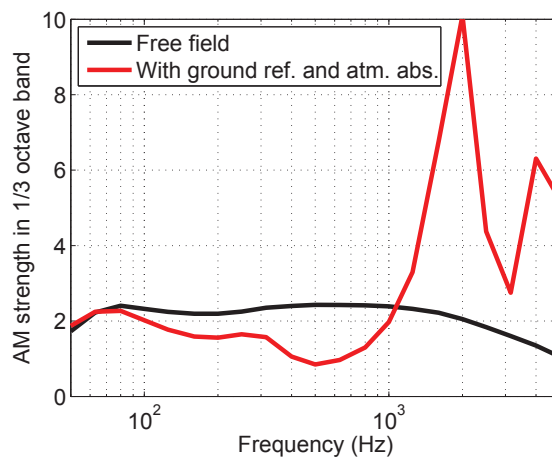
Figure 4.29: Spectrum of amplitude modulation strength. Observer is at $1000\,\mathrm{m}$ crosswind direction, $\sigma_e = 200 kPa \cdot s \cdot m^{-2}$.
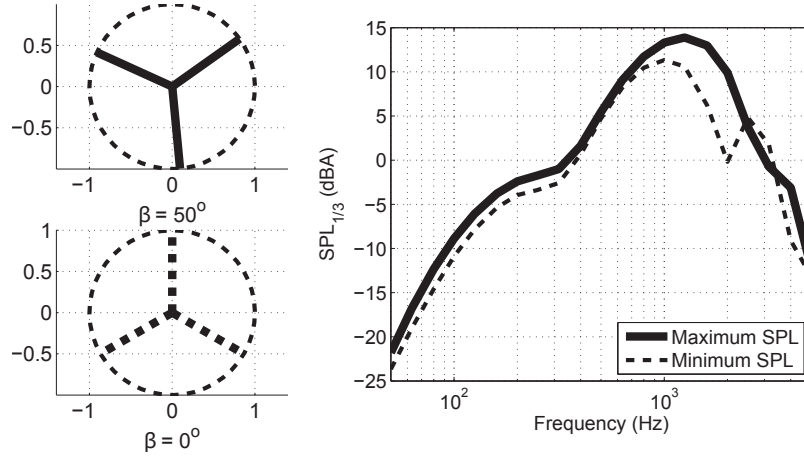
Figure 4.30: Spectra of two blade positions where the maximum and the minimum SPL level are observed for the third octave centered at f = 2000 Hz. Blade rotates clockwise. Observer is at 1000 m crosswind direction. Upper left: blade position when the maximum SPL is produced; lower left: blade position when the minimum SPL is produced.

We first plot in Figure 4.31 the color map in downwind, crosswind and upwind directions. Note that in the crosswind direction the atmosphere is homogeneous ($\cos\tau = 0$). Remember also that in this direction, the SWL is smaller than in downwind and upwind directions as shown in Figures 3.16 (a) and 3.27 in Chapter 3. In the upwind direction, when the propagation distance is larger than around 700 m, a shadow zone is clearly seen. The height of the shadow zone increases along with propagation distance.

We then look at the narrowband and the third octave band spectrum shown in Figures 4.32 and 4.33. The results are averaged over one complete blade rotation. The observer is at 500 and 1000 m away from the wind turbine, at 2 m height, in downwind, crosswind and upwind directions. We note that the first interference dip shifts a little along with the propagation angle. The peak frequency is not the same for the 3 spectra. In the upwind direction, when the observer is at 1000 m away from the wind turbine, the spectral level is really small compared to the other two; this is due to the fact that the observer is in the acoustic shadow zone, formed by the refraction of sound waves during the propagation. On the other hand, the observer at 500 m is not in the acoustic shadow zone, and the highest spectral levels are found in the upwind direction above 500 Hz.

Figure 4.34 shows the OASPL as a function of height for receivers at 1000 m distance in different directions. Really close to the ground, in the upwind direction, the received SPL is the lowest, due to the shadow zone effect. Along with the increase

(a) Downwind direction.

(b) Crosswind direction.
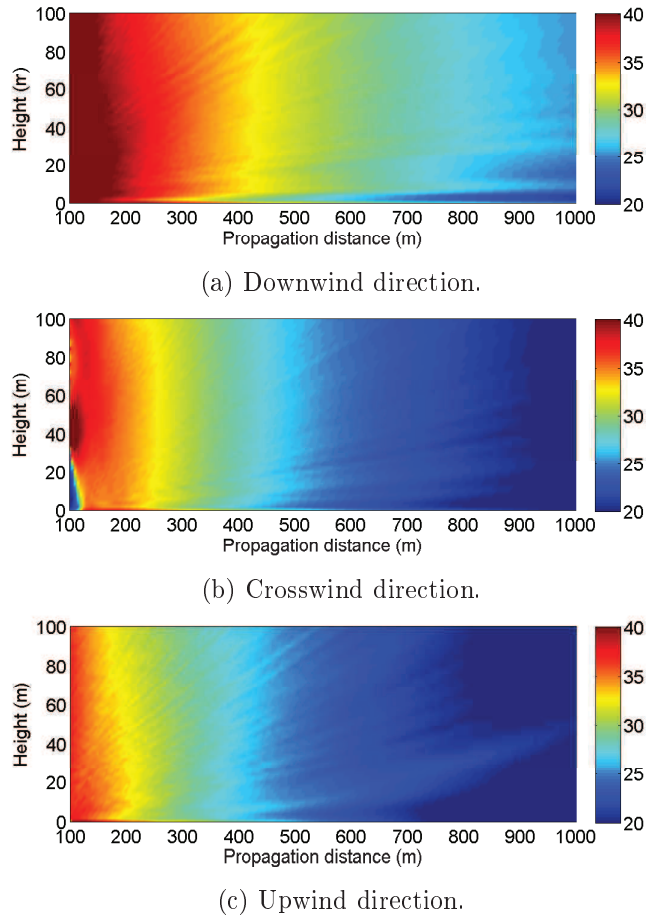
(c) Upwind direction.

Figure 4.31: Color maps of the overall SPL (dBA) in the propagation domain in downwind, crosswind and upwind directions respectively.

(a) Observer at R = 500 m z = 2 m.

(b) Observer at R = 1000 m z = 2 m.
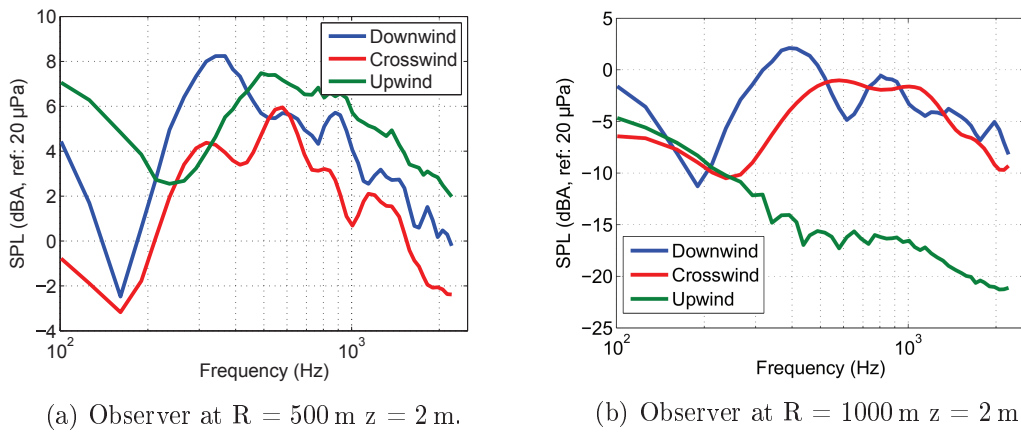
Figure 4.32: Narrowband SPL spectra averaged over blade position β in downwind, crosswind and upwind directions.

(a) Observer at R = 500 m z = 2 m.   (b) Observer at R = 1000 m z = 2 m.
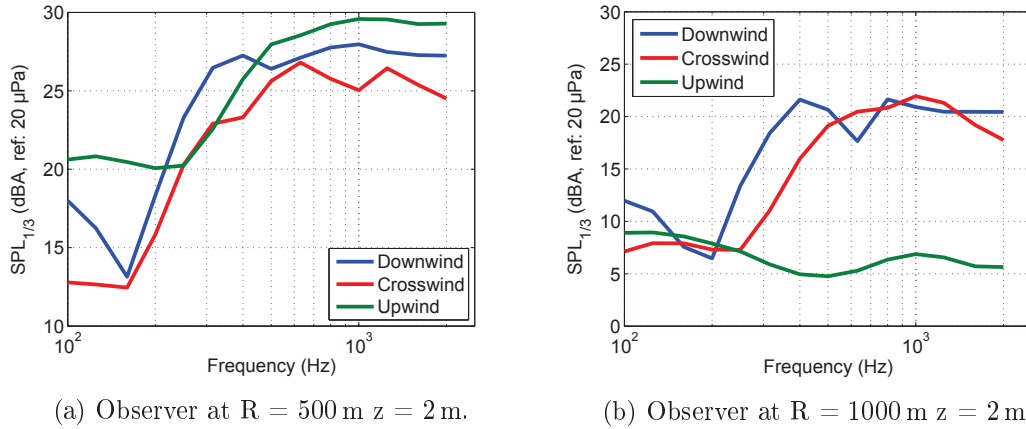
Figure 4.33: Third octave band SPL spectra averaged over blade position β in downwind, crosswind and upwind directions.

of height, the SPL in the upwind direction increases while remaining around 1 dB less than that in the downwind direction till around 35 m height. In the crosswind direction, the SPL is around 4-6 dB lower than in the other directions. This is in agreement with the SPL directivity plot shown in Chapter 3. Figure 4.35 shows the OASPL as a function of propagation distance for a receiver at 2 m height and 10 m height. In general, in all 3 directions, the SPL decreases with increasing distance. A more rapid decrease is observed in the upwind direction for an observer height of 2 m when the distance is greater than 800 m due to the shadow zone effect. The presence of the shadow zone is less evident at a height of 10 m. The SPL in the crosswind direction is always the lowest, except when the receiver enters the shadow zone for a height of 2 m.
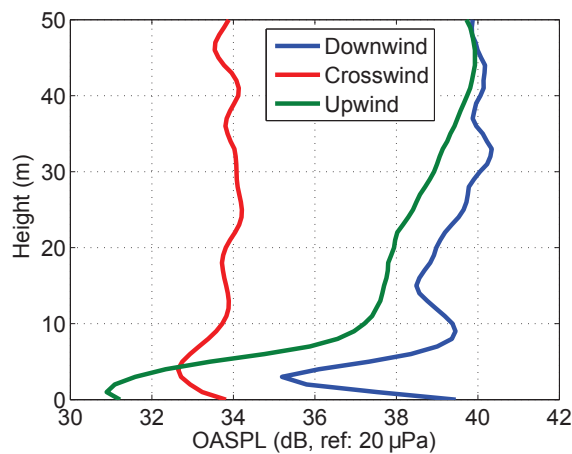
Figure 4.34: Overall SPL (averaged over blade position β) as a function of height for an observer located 1000 m away in downwind, crosswind and upwind directions.
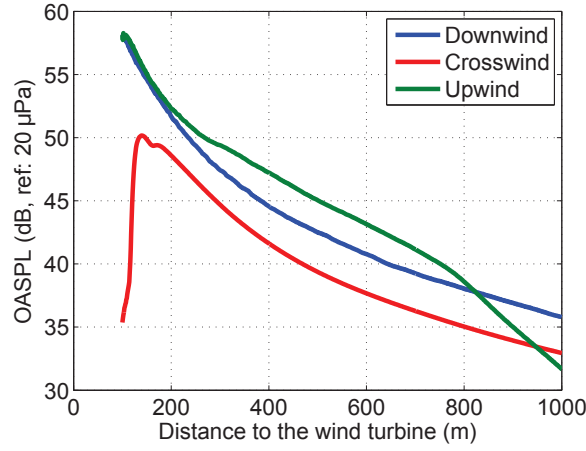
(a) Observer height z = 2 m.
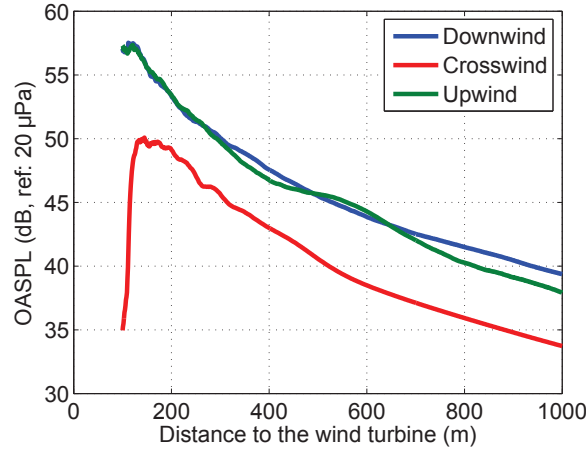
(b) Observer height z = 10 m.

Figure 4.35: Overall SPL (averaged over blade position β) as a function of observer distance in downwind, crosswind and upwind directions. (a) Observer height is 2 m; (b) observer height is 10 m.

4.4.3 Point source approximation

Wind turbine noise is an extended noise source, given the fact that the rotor diameter can be as large as 100 meters. But if the source-receiver distance is much larger than the rotor diameter, wind turbine noise may be modeled by a point source, and the calculation is greatly simplified. The validity of the point source approximation is studied in this section by using analytical propagation model and PE method respectively. The point source calculation is performed as:

1. Calculate the free field sound pressure level SPL_{FF} of the whole wind turbine;

2. Deduce SWL by $SWL = SPL_{FF} + 10 \log 10(4\pi r'^2)$ with r' the reference dis-

tance between the rotor and the observer;

3. Calculate the immission SPL level at far field as: $SPL_{far} = SWL - 10\log 10(4\pi r^2) + \Delta L - \alpha r$, with r the distance between the rotor and the far field observer. The relative SPL ΔL is calculated by analytical propagation model and PE method respectively.

4.4.3.1   Point source approximation by analytical model

We consider here the analytical model, so only ground reflection and atmospheric absorption are included. The reference temperature is 20^oC, and air humidity is 80%. Observer height is 2 m for all calculations in this section and Section 4.4.3.2. The narrow band spectra of SPL for extended source and point source calculations are compared in Figure 4.36 for various source-receiver distance in the downwind direction. This figure shows that there are many interference dips using a point source, while the extended source spectrum is quite smooth, as already noticed by Heutschi [10]. This is because the geometrical positions of the source and receiver are unique for a point source, while for the extended source, the distance between receiver and each segment are different. Thus the interference dips for each source (segment)-receiver distance occur at different frequencies when using the extended source, as previously shown in figure 4(a). As a result, the overall SPL is smoothed out by the compensations when summing up all the frequencies. At a larger distance, for example R = 1000 m, the 2 spectra almost overlap for frequency less than 1kHz, and the first interference dips appear at the same frequency. This is because when the receiver is far, the distance differences between source (segment)-receiver are small, so even for an extended source, the first interference dip occurs at almost the same frequency. However at higher frequencies, there are still some interference dips in the point source spectrum that are not observed for the extended source. Similar results are observed for other directions.

The overall SPL and the strength of AM are plotted with respect to propagation distance in Figures 4.37 and 4.38 considering an extended source and a point source. The AM for a point source is obtained considering that SPL_{FF} (and thus SWL) depends on the blade position β. We can see in Figure 4.37 that there are no significant discrepancies even at short propagation distance. Thus the point source approximation is good simplification for overall immission level prediction. However, Figure 4.38 shows that the point source calculations overestimate the amplitude modulation strength in all the tested ground azimuthal directions. Close to crosswind direction, for $\tau = 90^o$ and 105°, the increases are significant.

4.4.3.2   Point source approximation by PE method

Point source approximation is now examined using PE method, thus the atmospheric refraction is taken into account. Atmospheric absorption is also taken into account in this stage, to be in consistent with Section 4.4.3.1. The wind profile is

(a) R = 100 m

(b) R = 200 m

(c) R = 500 m

(d) R = 1000 m
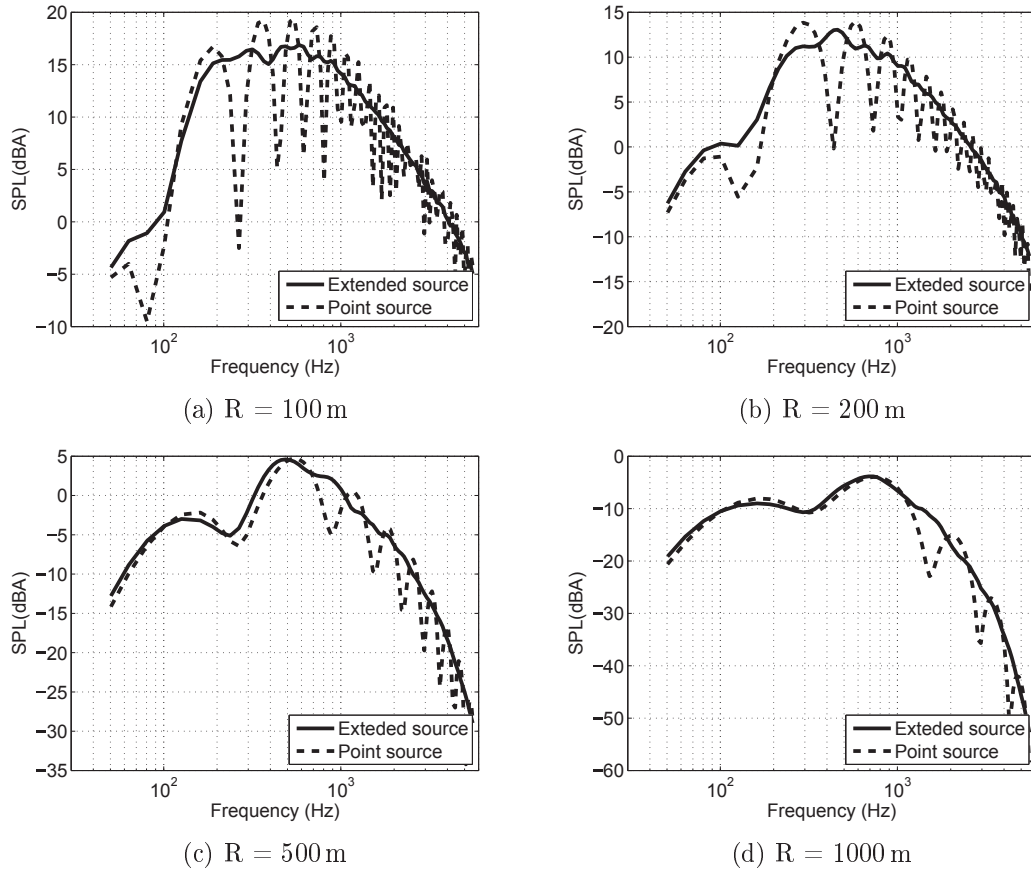
Figure 4.36: Narrowband SPL for point source and extended source calculations at different source-receiver distance in the downwind direction. Solid lines: extended source; dashed line: point source.
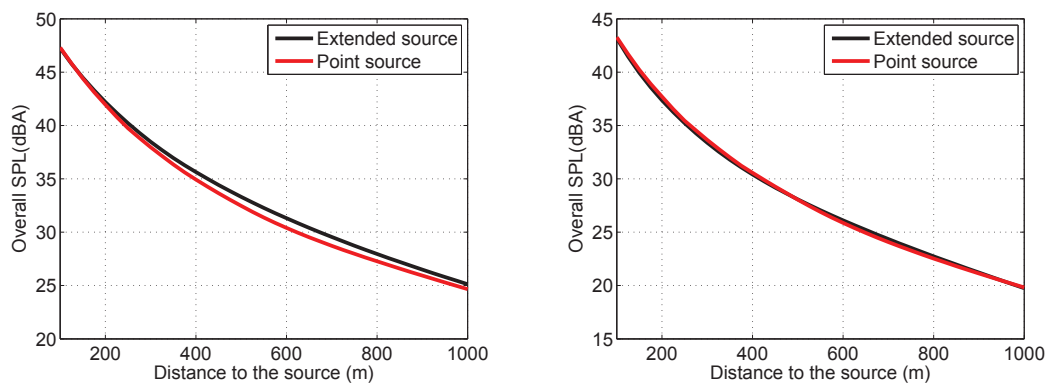
Figure 4.37: Overall SPL with respect to observer distance in (a) downwind direction, (b) crosswind direction.
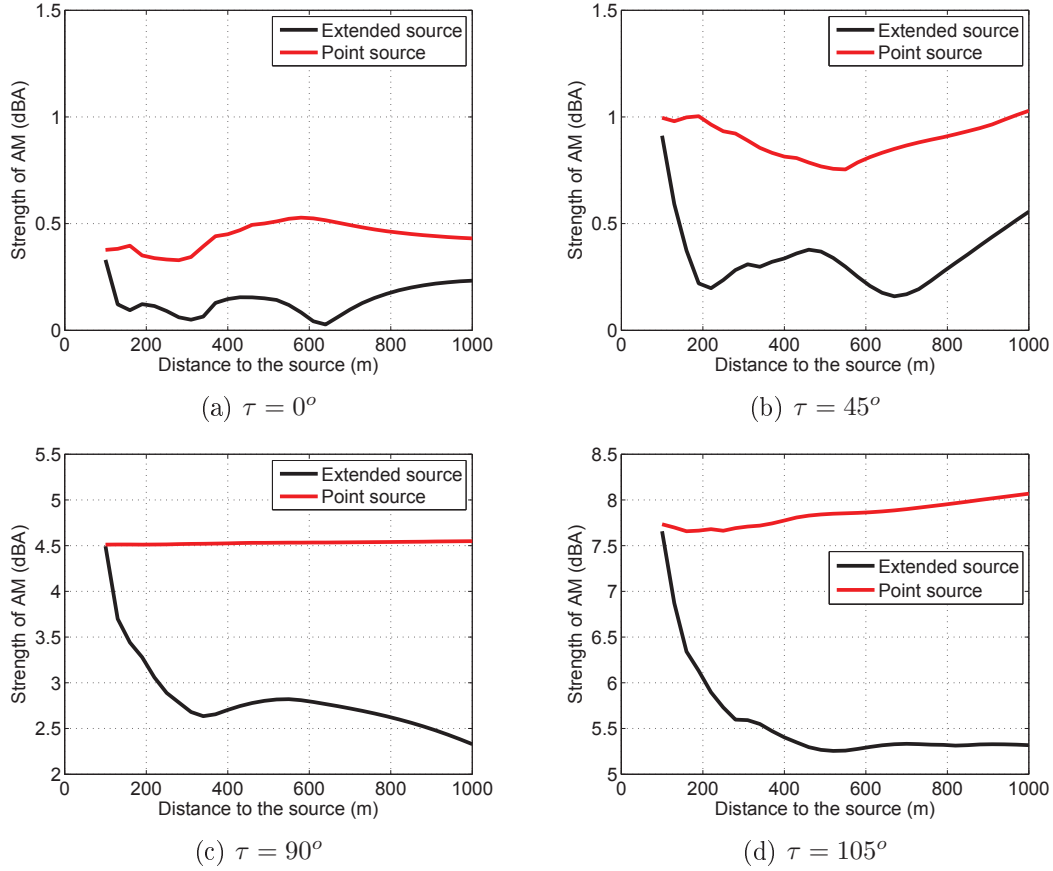
Figure 4.38: Amplitude modulation strength for extended source and point source calculations at different observer directions.

the same as in Section 4.4.2. Grassland with $\sigma_e = 200kPasm^{-2}$ is assumed. The spectra for observers at 200 m, 500 m and 1000 m away from the wind turbine in the downwind and upwind directions are shown in Figure 4.39. In all cases the observer height is fixed at 2 m. As seen in the previous section for homogeneous conditions, the point source spectra contain large interference dips, while the extended source spectra are quite smooth. What is different is that in the upwind direction, point source and extended source calculations do not converge anymore at long distances when atmospheric refraction is considered. In (f), both spectra decrease fast at high frequencies because of the shadow zone effect, but for extended source, this effect is averaged over all the segments. Therefore the decrease is less rapid than in the point source case.

Figure 4.40 shows the OASPL as a function of propagation distance in the downwind and upwind directions, for point source and the extended source calculations. In the downwind direction, the point source approximation results are higher than the extended source calculations for distances greater than 300 m. At a distance

(a) R = 200 m, downwind direction.

(b) R = 200 m, upwind direction.

(c) R = 500 m, downwind direction.

(d) R = 500 m, upwind direction.

(e) R = 1000 m, downwind direction.

(f) R = 1000 m, upwind direction.
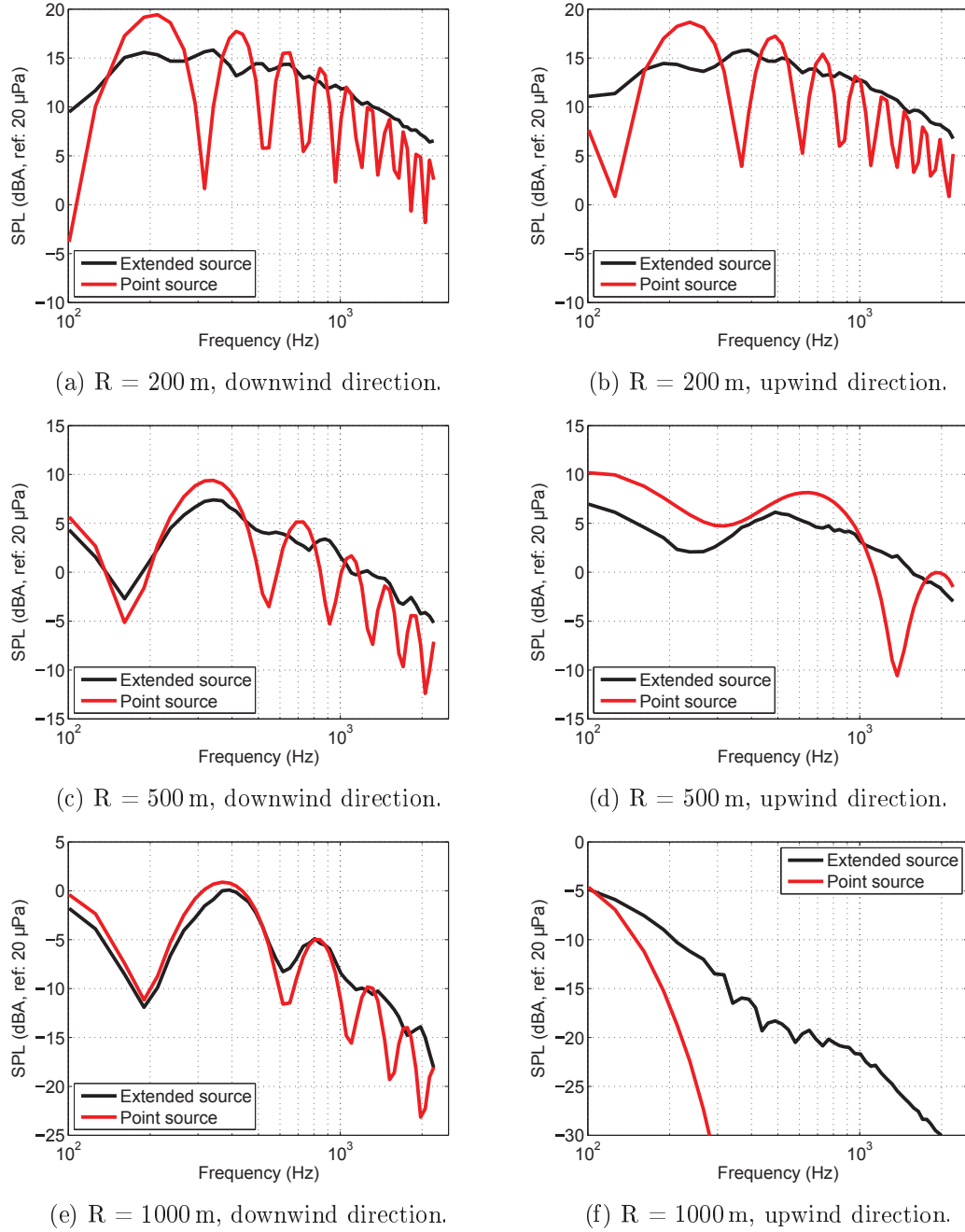
Figure 4.39: Narrowband spectra comparisons between extended source and point source approximation for various observer locations. Atmospheric refraction and absorption are taken into account.

of 1000 m, this overestimation is around 3 dB. However, in the upwind direction, the point source results strongly underestimate the levels in the shadow zone for distances greater than 700 m approximately. This underestimation reaches almost

10 dB at 1000 m. The shadow zone effect in the upwind direction is clear seen again in Figure 4.41. This big discrepancy in the shadow zone region is due to the fact that for extended source calculation, the relative positions between each segment and the unique observer are different, thus the interference dips appear in the spectra at different frequencies, which compensate the OASPL.

(a) Downwind direction   (b) Upwind direction
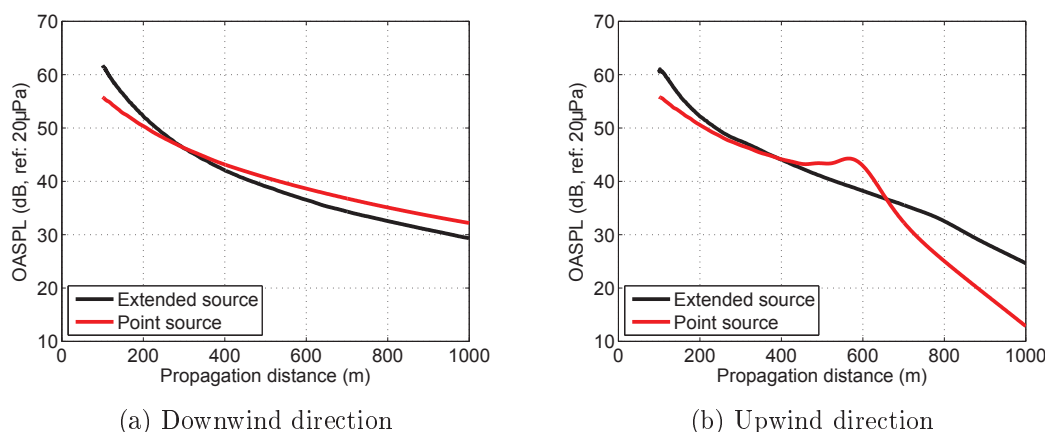
Figure 4.40: OASPL with respect to observer distance in (a) downwind direction, (b) crosswind direction. Observer height is 2 m. Atmospheric refraction and absorption are taken into account.

Thus we can conclude that the point source approximation for wind turbine noise calculation is not accurate when vertical wind shear (which leads to atmospheric refraction) is considered. However, we only considered one wind speed profile that corresponds to stable atmospheric conditions in this section. The point source approximation might give better accuracy in unstable and neutral conditions during which wind shear is less pronounced.

4.5   Conclusions

In this chapter, Amiet's theory is coupled with different propagation models to study the noise immission level in the far field. First, an analytical model for the acoustic radiation of a monopole source over an impedance ground is presented. The effect of atmospheric absorption is also included. Second, a parabolic equation code that takes into account refraction effects is considered. A back-propagation method is used to obtain the starting field for the PE calculation. The coupling method is validated in a homogeneous atmosphere over a rigid ground and an impedance ground against the analytical results. The agreements are generally good both for the noise spectra and the overall sound pressure levels for all the validation cases, with an average overestimation of 1 dB for the overall levels in both vertical and horizontal directions.

(a) Downwind direction
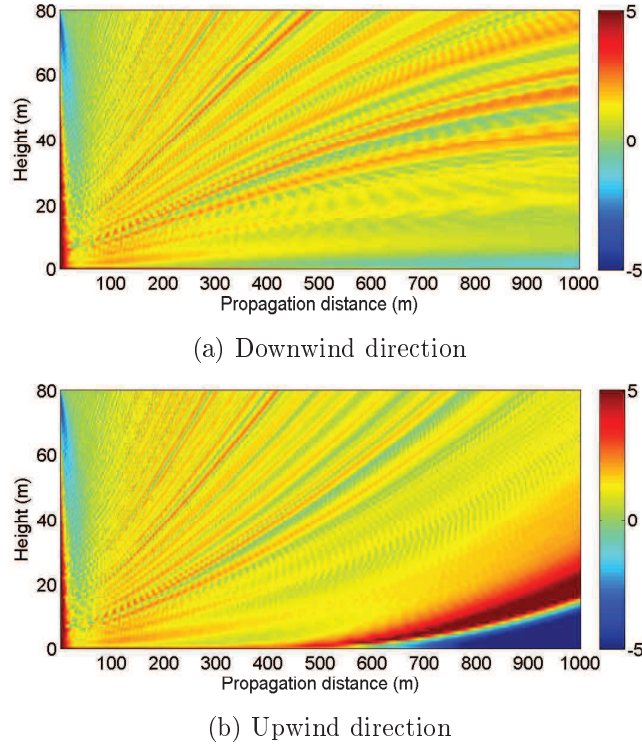
(b) Upwind direction

Figure 4.41: Color map of ΔL in the calculation domain for (a) downwind and (b) upwind direction with point source assumption. Atmospheric refraction and absorption are taken into account.

Using the analytical model, we showed that the immission level is reduced at large distance mainly due to atmospheric absorption. Ground reflection modifies the shape of the noise spectrum. The amplitude modulation strength is increased when considering a grassland with atmospheric absorption. When an inhomogeneous atmosphere is considered in the PE calculations (with $U = 8\,m/s$ and $H = -25\,W/m^2$), the atmospheric refraction effect can be seen clearly in the upwind direction as a shadow zone forms close to the ground surface.

The point source assumption for wind turbine noise is studied at the end of the chapter. Using the analytical propagation model, the assumption is valid for predicting the overall immission level, but it overestimates the amplitude modulation strength, and cannot account for the frequency dependence of ground effects. If we consider the atmospheric refraction due to wind shear, the point source approximation is no longer valid for the overall immission level. The spectra for point source and extended source calculations are different even at long distances.

Conclusions and perspectives

This PhD work aims at proposing a prediction model for wind turbine noise, based on a better understanding of the different noise source mechanisms and atmospheric propagation phenomena. The main achievements are the adaptation of Amiet's analytical model to a full size wind turbine with rotating blades, as well as the coupling of the source models to a parabolic equation propagation code, which makes possible the prediction of noise immission level at far field in a refractive atmosphere.

First, Amiet's models for turbulent inflow noise and trailing edge noise are studied and presented in details. For turbulent inflow noise model, an empirical thickness correction proposed by Roger & Moreau is introduced in order to take into account the influence of airfoil thickness. However, prediction results show that under real atmospheric turbulence conditions, this correction has little effect since the turbulence integral length scale in the atmosphere is much larger than the thickness of the turbine blade. For trailing edge noise, the key parameter to model is the wall pressure fluctuation spectrum. A model for an adverse pressure gradient flow is used instead of the original model suggested by Amiet. This new model by Rozenberg *et al.* is based on a scaling method with empirical corrections. The validations against measurements show a great improvement compared to earlier models that consider a zero pressure gradient flow.

Amiet's source models are then applied on a 2.3MW wind turbine. We took into account the rotation effects using Schlinker and Amiet approach, and showed this approach is valid in the frequency range of interest for wind turbine noise. First, SPL level predictions of trailing edge noise are compared against measurements for a constant wind profile. The agreement is good at high frequencies, but the predictions are too small at low frequencies. Second, this underestimation is corrected when turbulent inflow noise is also taken into account by considering vertical wind shear and atmospheric turbulence using Monin-Obukhov similarity theory. Wind shear causes large variations of AoA at blade leading edge, which significantly modifies the wall pressure spectra. However, it does not significantly change the total SPL spectrum at the receiver. On the other hand, the atmospheric turbulence has an important influence on the turbulent inflow noise. Features of directivity and amplitude modulation are also captured by the model. Finally, predictions by Amiet's models are compared with BPM semi-empirical model. The latter is able to predict separation noise. BPM predictions including separation

noise are in better agreement with measurements than Amiet's predictions for one test case, but overestimate the measured levels for the other test case.

The Amiet's models are finally coupled with an analytical propagation model and a numerical model based on the parabolic approximation. The analytical propagation considers the effect of ground reflection and atmospheric absorption. The ground effect modifies the shape of the spectrum, while the atmospheric absorption greatly reduces the noise level. With parabolic equation method, atmospheric refraction due to vertical wind shear is included. Shadow zone effect is clearly seen in the upwind direction, while in the downwind direction, a reinforcement on the noise level is also observed. The point source assumption is studied at the end. Results show that this approximation must be used with care in a refractive atmosphere. The overall sound pressure levels can be off by several decibels even at relatively long distances from the wind turbine.

Some perspectives can be mentioned:

- Besides turbulent inflow noise and trailing edge noise, separation/stall noise is also an important wind turbine noise source. The physical mechanism is still not well understood. On the one hand, there are few wind tunnel measurements of stall noise; on the other hand, the circumstances under which stall occurs in a wind farm need to be studied. It is of interest to perform wind tunnel measurements with a rotating airfoil, to study the dynamic stall and measure the associated noise. The goal would be to propose a more realistic model than BPM's semi-empirical model for separation noise that is based on static measurements. We have performed preliminary dynamic stall measurements in a return wind tunnel at ENSTA as explained in Appendix C. Also, direct noise simulations of this phenomenon could be performed using Code_Safari, developed at EDF R&D [60].

- A time domain formulation proposed by Farassat is another approach to study wind turbine noise. It has been applied by some research groups [27]. It will enable us to predict AM at the receiver, and at the same time to make sound synthesis possible.

- In this thesis, only a limited number of atmospheric conditions have been tested based on MOST. It will be interesting to study more realistic weather conditions, for instance using data from SIRTA, a meteorological observatory located not far from ENSTA. At SIRTA, temperature, wind speed & direction, atmospheric turbulence are measured using equipments such as anemometer, wind lidar throughout the year. Although it might not be the same conditions as in real wind farms, we could have access to more extreme atmospheric conditions than those predicted by MOST.

- Wind turbine noise prediction is subjected to the variation of atmospheric conditions, such as wind speed, wind direction, temperature variations, etc. It

would be interesting to study the variability of the noise level due to the change of atmospheric conditions, as this may help developers to better design a wind farm. A preliminary study using a Monte-Carlo approach has been presented at the last wind turbine noise conference [104].

- Parabolic equation method for sound propagation can include more information, such as terrain shape, turbulence scattering [56]. The linearized Euler equation method is also able to calculate the sound propagation. Parabolic equation method includes the wind shear indirectly using the effective sound speed approximation, while the linearized Euler equation method can directly integrate the wind shear in the calculations.

Second order correction term and sub-critical gusts for Amiet's model

In this appendix, airfoil transfer functions for the second order correction term due to the finite chord are given for trailing edge noise and turbulent inflow noise. The expressions for sub-critical gusts are also given in the following.

A.1 Second order correction term for trailing edge noise

As explained in Chapter 2, the chord of a real airfoil is not semi-infinite for the leading edge, thus the boundary condition as in Eq. (2.12) is no longer fulfilled for $x < -2b$ (or $\bar{x} < -2$). A correction term on induced pressure for $x < -2b$ is given by Roger and Moreau [45]:

$$
\begin{aligned}
P_2(\mathbf{x}, 0) \simeq & \ \frac{(1+i)e^{-4i\bar{\kappa}}}{2\sqrt{\pi}(1/\chi - 1)\bar{K}_c} \frac{1 - \Theta^2}{\sqrt{\bar{K}_c/\chi + M\bar{\mu} + \bar{\kappa}}} e^{i(M\bar{\mu} - \bar{\kappa})\bar{x}} \\
& \cdot \left\{ i[\bar{K}_c + M\bar{\mu} - \bar{\kappa}]\{F(\bar{x})\}^c + \left(\frac{\partial \{F(\bar{x})\}}{\partial \bar{x}}^c \right) \right\},
\end{aligned} \tag{A.1}
$$

with

$$
\Theta = \sqrt{\frac{\bar{K}_x + M\bar{\mu} + \bar{\kappa}}{\bar{K}_c + M\bar{\mu} + \bar{\kappa}}}, \quad \{F(\bar{x})\} = e^{2i\bar{\kappa}(\bar{x}+2)}\{1 - (1+i)E^*[2\bar{\kappa}(\bar{x}+2)]\}, \tag{A.2}
$$

and $\{-\}^c$ stands for that the term inside the brackets has to be corrected by a factor $\varepsilon = (1 + \frac{1}{4\bar{\mu}})^{-1/2}$.

The corresponding airfoil transfer function for the trailing edge noise 2nd order correction term is:

$$
\mathscr{L}_2 \simeq H \left\{ [e^{4i\bar{\kappa}}(1 - (1+i)E^*(4\bar{\kappa}))]^c - e^{2iD} + i[D + \bar{K}_c + M\bar{\mu} - \bar{\kappa}]G \right\}, \tag{A.3}
$$

with

$$
C = \bar{K}_c - \bar{\mu}(x_1/S_0 - M), \quad D = \bar{\kappa} - \bar{\mu}x_1/S_0, \quad H = \frac{(1+i)e^{-4i\bar{\kappa}}(1 - \Theta_1^2)}{2\sqrt{\pi}(1/\chi - 1)\bar{K}_c\sqrt{B}} \tag{A.4}
$$

$$
\begin{aligned}
G &= (1+\varepsilon)e^{i(2\bar\kappa+D)}\frac{sin(D-2\bar\kappa)}{D-2\bar\kappa}+(1-\varepsilon)e^{i-2\bar\kappa+D}\frac{sin(D+2\bar\kappa)}{D+2\bar\kappa}\\
&= +\frac{(1+\varepsilon)(1-i)}{2(D-2\bar\kappa)}e^{4i\bar\kappa}E^*[4\bar\kappa]-\frac{(1-\varepsilon)(1+i)}{2(D+2\bar\kappa)}e^{-4i\bar\kappa}E^*[4\bar\kappa]\\
&= +\frac{e^{2iD}}{2}\sqrt{\frac{2\bar\kappa}{D}}E^*(2D)\left[\frac{(1-\varepsilon)(1+i)}{2(D+2\bar\kappa)}-\frac{(1+\varepsilon)(1-i)}{2(D-2\bar\kappa)}\right].
\end{aligned} \tag{A.5}
$$

If we take into account this second order term, the airfoil transfer function used in Equation (2.35) and (2.66) should be replaced by $\mathscr{L}=\mathscr{L}_1+\mathscr{L}_2$.

A.2   Airfoil transfer function for sub-critical gusts of trailing edge noise

The sub-critical gusts ($\bar\kappa^2<0$) are essentially evanescent under the infinite span assumption. However, they will contribute to the radiated sound field due to the finite span. The main term and the leading edge back-scattering term of induced pressure fluctuation for sub-critical gusts are detailed by Roger and Moreau[45] as:

$$
P_1'(\mathbf{x},0)=-e^{-i\bar K_c\bar x/\chi}\{1-\Phi^o[(-i\{\bar K_c/\chi+M\bar\mu-i\bar\kappa'\}\bar x)^{1/2}]\}, \tag{A.6}
$$

$$
\begin{aligned}
P_2'(\mathbf{x},0) &\simeq \frac{1+i}{2\sqrt\pi(1/\chi-1)\bar K_c}\cdot\frac{1-\Theta'^2}{\sqrt{\bar K_c/\chi+M\bar m u-i\bar\kappa'}}e^{i(M\bar m u-i\bar\kappa')\bar x}\\
&\qquad \left[i\left\{\bar K_c+M\bar\mu-i\bar\kappa'\right\}F'(\bar x)+\frac{\partial F'(\bar x)}{\partial\bar x}\right],
\end{aligned} \tag{A.7}
$$

with

$$
\bar\kappa'=\sqrt{\left(\frac{\bar K_y}{\beta}^2-\bar\mu^2\right)},\quad \Theta'=\sqrt{\frac{\bar K_x+M\bar\mu-i\bar\kappa'}{\bar K_c+M\bar\mu-i\bar\kappa'}},
$$

$$
\Phi^o(\sqrt{ix})=\sqrt x e^{i\pi/4}E*(x),F'(\bar x)=1-\mathrm{erfc}(\sqrt{2\bar\kappa'(\bar x+2)}),
$$

where $\mathrm{erfc}(x)$ is the complementary complex error function.

Roger and Moreau[45] gave the expressions for the corresponding airfoil transfer function with sub-critical gusts as:

$$
\begin{aligned}
\mathscr{L}' &= \mathscr{L}_1'+\mathscr{L}_2'\\
&= \int_{-2}^{0}[f_1'(\bar y_1)+f_2'(\bar y_1)]e^{-iC\bar x}\,d\bar x,
\end{aligned} \tag{A.8}
$$

where

$$
\mathscr{L}_1'=-\frac{e^{2iC}}{iC}\left\{e^{-2iC}\sqrt{\frac{A_1'}{\bar\mu x_1/S_0-i\bar\kappa'}}\Phi^o\sqrt{2i(\bar\mu x_1/S_0-i\bar\kappa')}-\Phi^o\sqrt{2iA_1'}+1\right\}, \tag{A.9}
$$

$$\mathscr{L}_2' = \frac{e^{-2iD'}}{D'} H' \{ A' [e^{2iD'(1-erfc(\sqrt{4\bar{\kappa}'}))-1}]$$

$$+ \sqrt{2\bar{\kappa}'} \left(\bar{K}_c + \bar{\mu}(M - x_1/S_0) \right) \frac{\Phi^o \sqrt{-2iD'}}{-iD'} \}, \qquad (A.10)$$

and

$$A_1' = \bar{K}_x + \bar{\mu}M - i\bar{\kappa}', \quad A' = \bar{K}_c + \bar{\mu}M - i\bar{\kappa}'$$

$$H' = \frac{(1+i)(1-\Theta_1'^2)}{2\sqrt{\pi}(1/\chi - 1)\bar{K}_c \sqrt{A_1'}}, \quad D' = \bar{\mu}x_1/S_0 \qquad (A.11)$$

These expressions are used to obtain the results in Section 2.1.3.

A.3 Second order correction term for turbulent inflow noise

As for the trailing edge noise, a 2nd order correction term of induced pressure fluctuation at trailing edge can be introduced in order to fulfill the Kutta condition. The expression is given by Rozenberg [73]:

$$p_2(x, y, 0, t) = \frac{\rho_0 w_0 U}{\sqrt{2\pi(\bar{K}_x + \beta^2)}} e^{i\left[(M^2 \frac{\bar{k}}{\beta^2} - \kappa)\bar{x} - \pi/4 + \omega t - K_y y \right]} \left[1 - (1+i)E^*(2\bar{\kappa}(2-\bar{x})) \right],$$
$$(A.12)$$

and the corresponding airfoil transfer function for the turbulent inflow noise 2nd correction term is:

$$\mathscr{L}_2(\vec{x}_i, K_x, K_y) \simeq \frac{e^{i\Theta_2}}{\Theta_1 \pi \sqrt{2\pi(\bar{K}_1 + \beta^2\bar{\kappa})}} \{ i(1 - e^{-2i\Theta_1})$$

$$+ (1 - i) \left[E^*(4\bar{\kappa}) - \sqrt{\frac{2\bar{\kappa}}{\Theta_3}} e^{-i2\Theta_1} E^*(2\Theta_3) \right] \}, \quad (A.13)$$

with $\Theta_1 = \bar{\kappa} - \bar{\mu}x_1/S_0$, $\Theta_2 = \bar{\mu}(M - x_1/S_0) - \pi/4$ and $\Theta_3 = \bar{\kappa} + \bar{\mu}x_1/S_0$.

A.4 Airfoil transfer function for turbulent inflow noise with sub-critical gusts

For sub-critical gusts, airfoil transfer functions for the 1st order and 2nd order induced pressure fluctuation term are written as [73, 74]:

$$\mathscr{L}_1'(\vec{x}_i, K_x, K_y) = \frac{1}{\pi} \sqrt{\frac{2}{(\beta^2\bar{\kappa}' + \bar{K}_1) \cdot \Theta_1}} E * [2\Theta_1'] e^{i\Theta_2} \qquad (A.14)$$

and

$$\mathscr{L}_2(\vec{x}_i, K_x, K_y) \simeq \frac{e^{i\Theta_2}}{\Theta_1 \pi \sqrt{2\pi(\bar{K}_1 + \beta^2\bar{\kappa}')}} \{ i(1 - e^{-2i\Theta_1'} - erf(\sqrt{-4\bar{\kappa}'}))$$

$$- \frac{2e^{-i2\Theta_1'}}{1+i} \sqrt{\frac{\bar{\kappa}'}{\Theta_3'}} \Phi^o(2i\Theta_3') \}, \qquad (A.15)$$

with $\Theta_1' = i\bar{\kappa}' - \bar{\mu}x_1/S_0$, $\Theta_3 = i\bar{\kappa}' + \bar{\mu}x_1/S_0$.

Monin-Obukhov similarity theory

B.1 Main parameters of Monin-Obukhov similarity theory

Monin-Obukhov similarity theory (MOST) describes mean and turbulent parts of wind speed and temperature in the surface layer as a function of the dimensionless height parameter L_{MO} [105]. The main assumptions and limitations are [87]:

- MOST applies in the atmospheric surface layer, in which surface fluxes are relatively constant: this layer can be $200\,\mathrm{m}$ thick under unstable conditions, but may be considerably thinner under very stable conditions (highly intermittent turbulence);

- the surface must be flat and homogeneous: fetch effects, mountainous or coastal environments are not described;

- wind turning with heights and low-levels inversions (changes in the signs of the gradients) are not accounted for;

- MOST is valid in an ensemble-average sense.

The Monin-Obukhov length scale L_{MO} is defined as [87, 35]:

$$L_{MO} = -\frac{\overline{\theta}u_*^3}{\kappa g \overline{(w'\theta')_s}},$$ (B.1)

where $\overline{\theta}$ is the mean part of the temperature potential, u_* is the friction velocity defined by the 3 components of turbulent velocity fluctuation u', v', w' as:

$$u_*^2 = \left[\overline{(u'w')_s}^2 + \overline{(v'w')_s}^2 \right]^{1/2},$$ (B.2)

κ is the von Kárman constant, g is the gravity acceleration, and finally $\overline{w'\theta'}$ is the vertical kinematic heat flux, with the subscription 's' standing for the value evaluated on the ground. The heat flux $\overline{w'\theta'}$ is also a measure of atmospheric stability, thus L_{MO}^{-1} can be seen as an index of atmospheric stability. The atmosphere is called stable if $L_{MO}^{-1} > 0$; unstable is $L_{MO}^{-1} < 0$ and neutral if $L_{MO}^{-1} \simeq 0$. In practice, MOST is consider valid for $-2 < z/L_{MO} < 1$ [106]. One can also express L_{MO} as a function of the sensible heat flux $H = \rho_0 C_p w' T'$ as:

$$L_{MO} = -\frac{\rho_0 C_p \overline{\theta} u_*^3}{\kappa g H},$$ (B.3)

with C_p the dry air heat capacity, and usually $C_p = 1004 J/Kg/K$.

Typical values

- Cheinet [87] states that heat flux $H = 200 - 600 \; W/m^2$ on fair-weather days and $-100 \, W/m^2$ on clear nigths;

- Ostashev *et al.* [88] suggest that for summer weather at midlatitudes, H is between $-50 \, W/m^2$ and $600 \, W/m^2$. More specifically, for mostly sunny day, $H = 200 \, W/m^2$ and for cloudy day, $H = 40 \, W/m^2$.

B.2 Businger-Dyer profiles

The similarity relations yield the following dimensionless wind speed and temperature derivatives [107, 106]:

$$\phi_w = \frac{\kappa z}{u_*} \frac{d\bar{u}}{dz}, \qquad \phi_t = \frac{\kappa z}{u_*} \frac{d\bar{\theta}}{dz}. \tag{B.4}$$

Then the Businer-Dyer relations are given as [35]:

$$\phi_w = \begin{cases} (1 - 16z/L_{MO})^{-1/4} & \text{for} \quad L_{MO}^{-1} < 0 \quad \text{(unstable atmosphere)}, \\ (1 + 5z/L_{MO}) & \text{for} \quad L_{MO}^{-1} > 0 \quad \text{(neutral and stable atmosphere)}, \end{cases} \tag{B.5}$$

and

$$\phi_t = \begin{cases} (1 - 16z/L_{MO})^{-1/2} & \text{for} \quad L_{MO}^{-1} < 0 \quad \text{(unstable atmosphere)}, \\ (1 + 5z/L_{MO}) & \text{for} \quad L_{MO}^{-1} > 0 \quad \text{(neutral and stable atmosphere)}, \end{cases} \tag{B.6}$$

By integrating equations (B.4) from height z_0 to an arbitrary height z, using equations (B.5) and (B.6), the mean wind speed and temperature profiles can be obtained:

$$\bar{u}(z) = \frac{u_*}{\kappa} \left[\ln \left(\frac{z}{z_0} \right) - \psi_w \right], \tag{B.7a}$$

$$\bar{\theta}(z) = \theta_0 + \frac{\theta_*}{\kappa} \left[\ln \left(\frac{z}{z_0} \right) - \psi_t \right], \tag{B.7b}$$

with θ_0 the temperature at height z_0 and $\theta_* = -\overline{(w'\theta')}_s/u_*$. For an unstable atmosphere:

$$\psi_w = 2 \ln \left(\frac{1+x}{2} \right) + \ln \left(\frac{1+x^2}{2} \right) - 2 \arctan x + \frac{\pi}{2}, \tag{B.8a}$$

$$\psi_t = 2 \ln \left(\frac{1+x^2}{2} \right), \tag{B.8b}$$

with $x = (1 - 16z/L_{MO})^{1/4}$. For a stable atmosphere ($L_{MO}^{-1} > 0$), while $z/L_{MO} \leq 0.5$ [35]:

$$\psi_w = \psi_t = -5z/L_{MO}, \tag{B.9}$$

while $z/L_{MO} > 0.5$:

$$\psi_w = \psi_t = -7\ln\left(z/L_{MO}\right) - \frac{4.25}{z/L_{MO}} + \frac{0.5}{(z/L_{MO})^2} - 0.852. \tag{B.10}$$

Note that the expressions of ϕ_w and ϕ_t are based on experimental campaigns, slightly different expressions exist in the literature.

B.3 Atmospheric turbulence modeling

In this study, we focus on velocity fluctuations that are required in the turbulent inflow noise model. Although temperature fluctuations can play a role on acoustic scattering during wave propagation, Cheinet [87] points that the velocity fluctuations largely dominate while the temperature fluctuations could only contribute for very low winds.

Standard deviations

Under unstable conditions ($L_{MO} \leq 0$), Cheinet [87] gives the following empirical relationship for the wind variance :

$$\sigma_u^2(z, u_*, F_T) = u_*^2 \left[\alpha_1 + \frac{1}{|L_{MO}|}\left(\alpha_2 z_i + \alpha_3 z\right)\right]^{2/3}, \tag{B.11}$$

with z_i the mixed layer height (set to $1000\,\mathrm{m}$), $\alpha_1 = 5.2$, $\alpha_2 = 0.52$, $\alpha_3 = 0$ in the surface layer ($z \leq 0.1z_i$) and $F_T = (\overline{w'\theta'})_s$. These values fit Wilson's results [108] of $\sigma_u^2 = 3.0u_*^2$ for purely shear-driven turbulence (neutral conditions), and $\sigma_u^2 = 0.35w'^2$ for pure buoyancy turbulence.

Under stable conditions ($L_{MO} > 0$), the empirical relationship given by Cheinet [87] for the wind variance is:

$$\sigma_u^2(z, u_*, F_T) = u^{*2}\left[1.73 + 3.3\left(\frac{z}{L_*}\right)^{0.5}\right]^2. \tag{B.12}$$

Both expressions yield $\sigma_u^2 = 3.0u^{*2}$ when $L_* \to \infty$ (neutral conditions).

Turbulence outer scales in von Kármán model

The outer scale in the von Kármán model is given by [87]:

$$L_{outer}(z, u_*, F_T) = \left(1.91\frac{\sigma_u^2(z, u_*, F_T)}{C_u^2(z, u_*, F_T)}\right)^{3/2}, \tag{B.13}$$

with C_u^2 the structure parameter of momentum fluctuations parametrized as follows:

$$C_u^2(z, u_*, F_T) = \frac{u_*^2}{z^{2/3}}f_u\left(\frac{z}{L}\right), \tag{B.14}$$

with

$$f_u(\xi) = 3.9 \left(\frac{1-\xi}{1-7\xi} - \xi \right)^{2/3}, \quad \xi \leq 0, \tag{B.15a}$$

$$f_u(\xi) = 3.9 \left(1 + 5\xi \right)^{2/3}, \quad \xi > 0, \tag{B.15b}$$

with $\xi = z/L_{MO}$. Wilson [109] states that $L_{outer} = 1.8\,z$ for purely shear-driven turbulence, and $L_{outer} = 0.23\,z_i$ for pure buoyancy turbulence.

Dynamic stall measurements

In order to study the mechanisms of stall noise, a wind tunnel experiment is designed to measure both static stall and dynamics stall. In the preliminary measurements presented here, only the force coefficients are recorded. Surface pressure measurements are planned in the near future to study the onset and the development of the stall; they will not be included in this appendix.

C.1 Experiment setup

Measurements are performed in the closed return wind tunnel at ENSTA ParisTech (see Figure C.1). The test section is 45 cm x 45 cm, inside which an airfoil is placed that can be turned using a rotating system including an aerodynamic balance (see Figure C.2). The aerodynamic balance is able to measure the lift and drag forces at a relatively high sampling rate. The airfoil is a NACA 0024 of span 41 cm and chord 16.5 cm (see Figure C.3).

Figure C.1: Closed return wind tunnel at ENSTA ParisTech.

For the static stall measurments, the flow velocities (U) are 12.8 m/s and 25.6 m/s, corresponding to chord based Reynolds numbers of $1.4 \cdot 10^5$ and $2.8 \cdot 10^5$ respectively. For the dynamic stall measurements, the flow velocity is around 12.5 $\tilde{}13$ m/s, the oscillation frequencies are from 0.1 Hz to 2.6 Hz, corresponding to reduced frequencies ($\tilde{\omega} = \pi f c / U$) of 0.004 to 0.1.
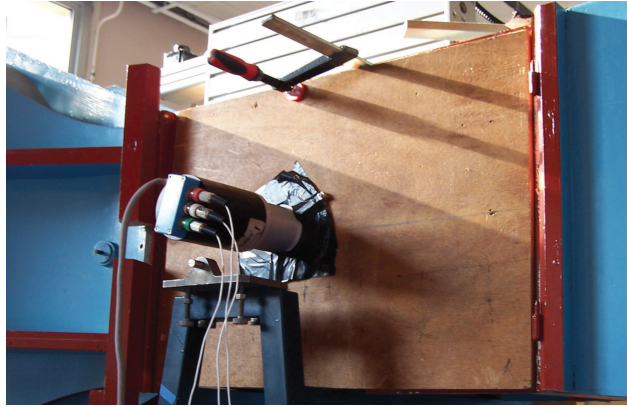
Figure C.2: Rotating system and the aerodynamic balance.
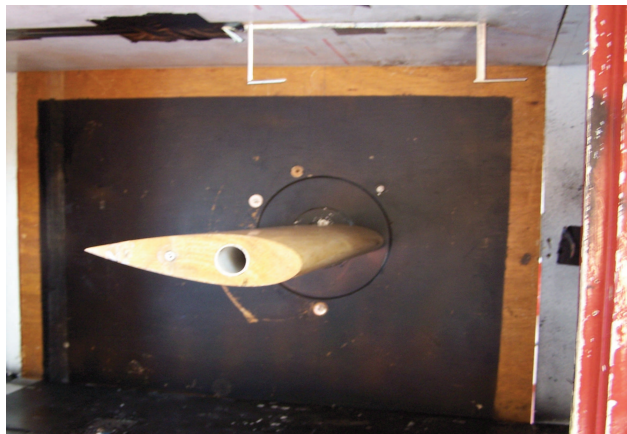
Figure C.3: An NACA 0024 airfoil is mounted in side the wind tunnel.

(a) U $= 12.8\,\mathrm{m/s}$ (b) U $= 25.6\,\mathrm{m/s}$
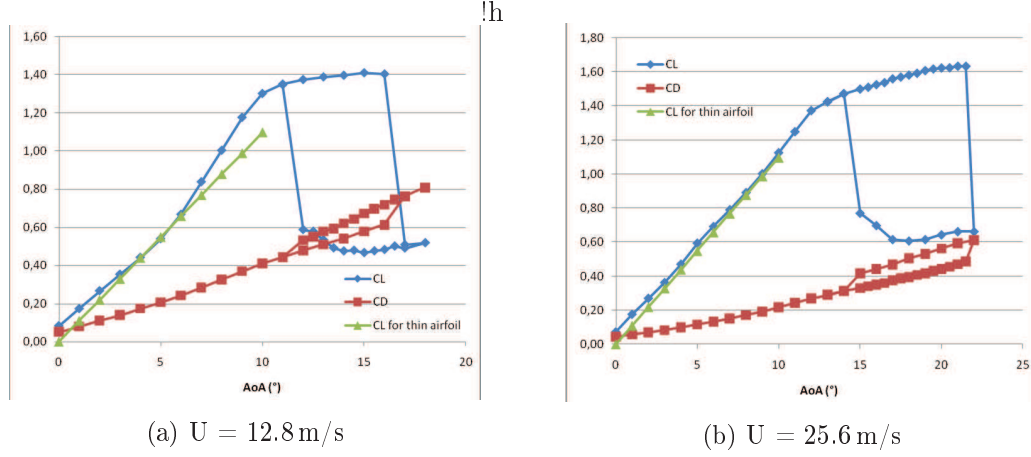
Figure C.4: Static measurements of lift coefficient C_l and drag coefficient C_d for two test velocities.

C.2 Results of static stall measurements

Static measurements are done by varying the AoA α step by step, from 0° to 18°. The lift and drag coefficient C_l, C_d for the two test velocities are plotted in Figure C.4. When AoA is increased, the lift coefficient follows the thin airfoil theory ($C_l = 2\pi\alpha$) for small angles of attack. Static stall occurs around $17 - 18^o$ for U $= 12.8\,\mathrm{m/s}$, and around $21.5 - 22^o$ for U $= 25.6\,\mathrm{m/s}$. Then the angle of attack is decreased step by step and the flow reattaches between $11 - 12^o$ for U $= 12.8\,\mathrm{m/s}$, and between $13 - 14^o$ for U $= 25.6\,\mathrm{m/s}$. This illustrates the phenomenon of flow hysteresis [110].

C.3 Results of dynamic stall measurements

During the dynamic stall measurements, the flow velocity is carefully set the same as for the static stall with the test velocity of $12.8 m/s$. However, a variation between $12.5 - 13\ m/s$ is observed during the oscillation of the airfoil. The tested cases are configured as shown in Table C.1. The results are averaged over 10 cycles for all the cases; for comparison, the static results are also plotted as shown in Figure C.5, some common similarities are observed:

1. At low oscillation frequency, before reaching the stall angle, C_l of dynamic case is smaller than that of static case. The differences decrease with the increase of the oscillation frequency;

2. C_l increases with increasing AoA for all cases till around 12°, then is remains constant especially for the low oscillating frequency cases;

3. During the dynamic stall, C_l drops rapidly, and at the same time, C_d increases a little;

!h

Case	$U(m/s)$	Oscillation frequency (Hz)	Oscillation amplitude (^{o})	Range of AoA (^{o})
1	$12.5 - 13$	0.1	$\alpha(t) = 15^o + 15\sin(\omega t)$	0 - 30
2	$12.5 - 13$	0.3	$\alpha(t) = 15^o + 15\sin(\omega t)$	0 - 30
3	$12.5 - 13$	0.6	$\alpha(t) = 15^o + 15\sin(\omega t)$	0 - 30
4	$12.5 - 13$	1.3	$\alpha(t) = 15^o + 15\sin(\omega t)$	0 - 30
5	$12.5 - 13$	2.6	$\alpha(t) = 15^o + 15\sin(\omega t)$	0 - 30
6	$12.5 - 13$	0.3	$\alpha(t) = 15^o + 10\sin(\omega t)$	5 - 25

Table C.1: Parameters setup for the test cases.

4. The reattachment is clearly captured for low oscillation frequency cases (e.g. cases 1 and 2). Compared to the static case, we can see that the reattachment is delayed due to the oscillation;

5. Due to the rotating motor capacity, when the oscillation frequency is too large (for case 5), the desired AoA range cannot be reached, so the results for case 5 is not trustworthy and thus is not plotted.

Parallel comparisons for C_l and C_d for cases 1-4 are shown in Figure C.7. The test case 5 is not included for the reason mentioned above. From the C_l comparison (Figure C.7.a), the delay of the flow separation and reattachment due to the oscillation frequency is clear seen. At AoA $= 30^o$, for all the cases, C_l value drops to around 0.4. The same phenomenon is also observed for C_d plot: at AoA $= 30^o$, C_d value is around 1.15-1.25.

An other test case with oscillation frequency $f = 0.3\,Hz$, AoA range between $5^o - 25^o$ is also performed to compare with case 2 (see Figure C.8). We can see that dynamics stall angle is influenced by the oscillation range. The results show that a wider oscillating range delays the flow separation; at the same time, it also delays the reattachment.
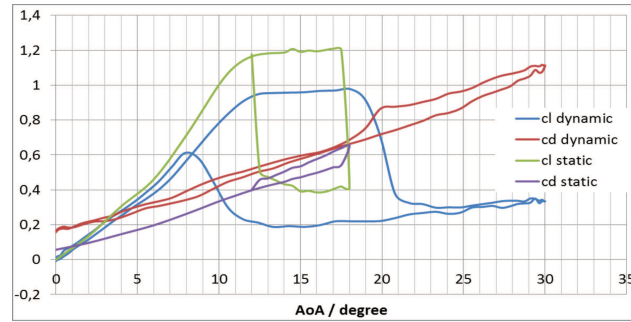
(a) Case 1, f = 0.1 Hz, range of AoA = 0 − 30°.
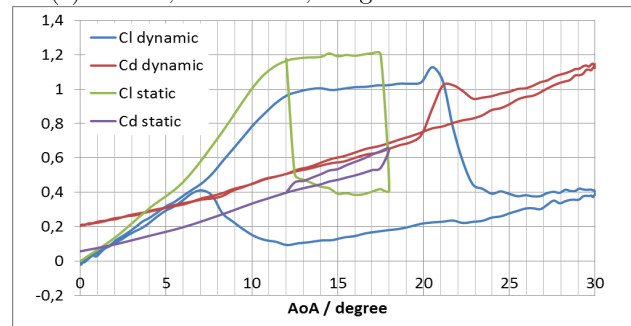
(b) Case 2, f = 0.3 Hz, range of AoA = 0 − 30°.

!h
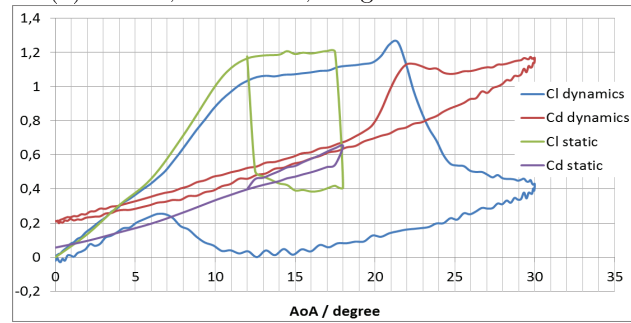
(c) Case 3, f = 0.6 Hz, range of AoA = 0 − 30°.
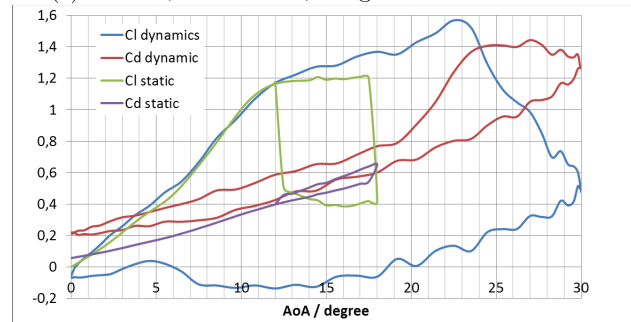
(d) Case 4, f = 1.3 Hz, range of AoA = 5 − 25°.

Figure C.5: Lift and drag coefficients measured for dynamic stall cases compared to static case.
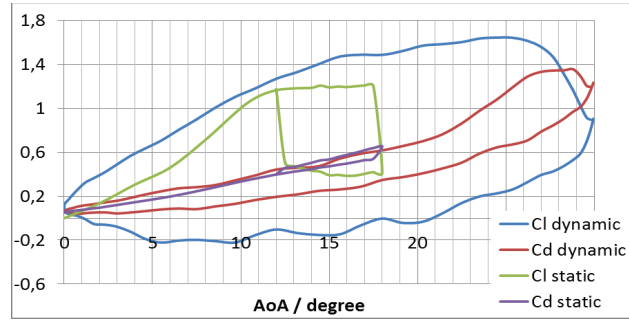
Figure C.6: (Continued) Lift and drag coefficients measured for dynamic stall cases compared to static case. Case 5, f = 2.6 Hz, range of AoA = $0 - 30^o$.
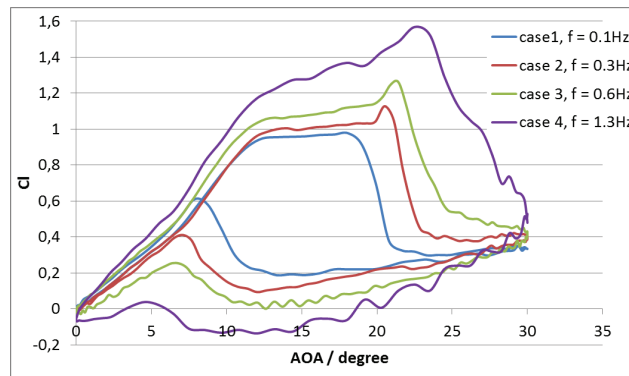
(a) C_l plots for case $1\tilde{4}$.
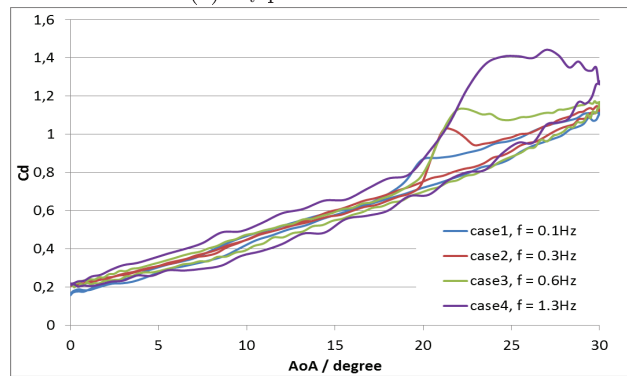
(b) C_d plots for case $1\tilde{4}$.

Figure C.7: Parallel comparisons of lift and drag coefficients measured for dynamic stall cases.
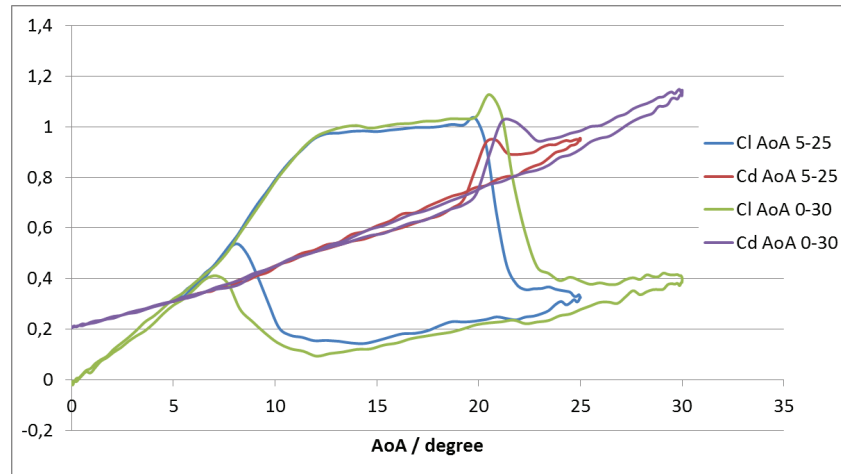
Figure C.8: Lift and drag coefficients for 2 test cases with the same oscillation frequency f = 0.3 Hz, and different oscillation amplitudes.

C.4   Future work on stall noise measurements

In the future, it would be desirable to perform the following measurements to characterize dynamic stall and the associated noise radiation:

- Surface pressure measurements of an airfoil with oscillating motion. Pressure sensor will be mounted on the surface of the test airfoil. This will allow us to study the detachment/reattachment occurrences.

- Direct acoustic measurements. An anechoic wind tunnel facility is needed for these measurements.

Bibliography

[1] T. Brooks, D. Pope, and M. Marcolini, "Airfoil self-noise and prediction," *NASA Reference Publication 1218*, 1989. (Cited on pages vii, viii, 6, 7, 14, 15, 38, 39 and 76.)

[2] S. Oerlemans, P. Sijtsma, and B. M. López, "Location and quantification of noise sources on a wind turbine," *Journal of Sound and Vibration*, vol. 299, 2007. (Cited on pages vii and 7.)

[3] S. Oerlemans and J. G. Schepers, "Prediction of wind turbine noise and validation against experiment," *International Journal of Aeroacoustics*, pp. pp. 555–584, Aug 2009. (Cited on pages vii, 6, 7, 8, 9, 15, 59, 66, 68 and 102.)

[4] H. Moller and C. S. Pedersen, "Low-frequency noise from large wind turbines," *J. Acoust. Soc. Am*, vol. 129, 2011. (Cited on pages vii, 8, 9 and 11.)

[5] W. Zhu, N. Heilskov, W. Shen, and J. Sørensen, "Modeling of aerodynamically generated noise from wind turbines," *Journal of Solar Energy Engineering*, vol. 127, pp. 517–528, 2005. (Cited on pages vii, 6, 9 and 15.)

[6] S. Oerlemans, M. G. Smith, and P. White, "Wind turbine amplitude modulation: Research to improve understanding as to its cause and effect," tech. rep., renewableUK, 2013. (Cited on pages vii, 8 and 10.)

[7] A. L. Rogers, J. F. Manwell, and S. Wright, "Wind turbine acoustic noise," tech. rep., Renewable energy research laboratory, University of Massachusetts, Jan 2006. (Cited on pages vii, 6 and 11.)

[8] J. M. Prospathopoulos and S. G. Voutsinas, "Noise propagation issues in wind energy applications," *American Society of Mechanical Engineers*, vol. 127, 2005. (Cited on pages vii and 12.)

[9] G. van den Berg, "Effects of the wind profile at night on wind turbine sound," *Journal of Sound and Vibration*, vol. 277, 2004. (Cited on pages vii, 10 and 12.)

[10] K. Heutschi, R. Pieren, M. Muller, M. Manyoky, U. W. Hayek, and K. Eggenschwiler, "Auralization of wind turbine noise: propagation filtering and vegetation noise synthesis," *Acta Acustica united with Acustica*, vol. 100, 2014. (Cited on pages vii, 12, 13 and 116.)

[11] S. Riddell, T. Vandervort, J. Esser, and R. Drobietz, "Noise reducer for rotor blade in wind turbine," July 12 2011. US Patent 7,976,276. (Cited on pages vii and 13.)

[12] M. Kamruzzaman, T. Lutz, W. Shen, W. Zhu, M. Hansen, F. Bertagnolio, and H. Madsen, "Validations and improvements of airfoil trailing edge noise prediction models using detailed experimental data," *Wind Energy*, vol. 15, 2012. (Cited on pages viii, xv, 30, 35, 36 and 37.)

[13] R. W. Paterson and R. K. Amiet, "Acoustic radiation and surface pressure characteristics of an airfoil due to incident turbulence," *NASA report, CR-2733*, 1976. (Cited on pages viii, 35, 46 and 47.)

[14] W. Devenport, J. Staubs, and S. Glegg, "Sound radiation from real airfoils in turbulence.," *Journal of Sound and Vibration*, vol. 329, 2010. (Cited on pages viii, 46, 47, 48 and 49.)

[15] J. Jonkman, S. Butterfield, W. Musial, and G. Scott, "Definition of a 5-mw reference wind turbine for offshore system development," tech. rep., National Renewable Energy Laboratory, Feb 2009. (Cited on pages ix, 53, 54 and 55.)

[16] V. P. Blandeau and P. F. Joseph, "Validation of amiet's model for propeller trailing-edge noise," *AIAA Journal*, vol. 49, no. 5, 2011. (Cited on pages ix and 58.)

[17] H. Madsen, A. Fischer, and K. Kragh, "Mechanisms and causes of amplitude modulation and other amplitude modulation of aeroacoustic wind turbine noise," in *Wind Turbine Amplitude Modulation: Research to Improve Understanding as to its Cause and Effect*, RenewableUK, 2013. (Cited on pages x, 70 and 71.)

[18] G. Leloudas, "Optimization of wind turbines with respect to noise," Master's thesis, DTU, 2006. (Cited on pages x, xv, 56, 57, 63, 65, 73, 79, 80 and 81.)

[19] M. Drela and H. Youngren, "Xfoil 6.9 user primer," November 2001. (Cited on pages xv, 30 and 31.)

[20] G. Corbetta, "Wind in power- 2014 european statistics," tech. rep., European wind energy association, Feb 2015. (Cited on page 5.)

[21] J. Moccia, "Wind energy scenarios for 2020," tech. rep., European wind energy association, Jul. 2014. (Cited on page 5.)

[22] Wikipedia, "Wind power in france — wikipedia, the free encyclopedia," 2015. [Online; accessed 27-July-2015]. (Cited on page 5.)

[23] P. Dutilleux and J. Gabriel, "Recommendations for improved acceptance of wind farm projects in france with regard to acoustic noise," tech. rep., DEWI magazin, Feb 2008. (Cited on page 6.)

[24] E. Koppen and K. Fowler, "Ineternational legislation for wind turbine noise euronoise," European Acousitcs Association, 2015. (Cited on page 6.)

[25] M. Bastasch, "Summary of international wind turbine noise regulationsr," tech. rep., Renewable northwest project, Apr, 2011. (Cited on page 6.)

[26] D. J. Alberts, "Addressing wind turbine noise," tech. rep., Lawrence technological university, Jan 2006. (Cited on page 6.)

[27] S. Lee, S. Lee, and S. Lee, "Numerical modeling of wind turbine aerodynamic noise in the time domain," *J. Acoust. Soc. Am.*, vol. 133, no. 2, 2013. (Cited on pages 8, 14 and 124.)

[28] S. L, K. Kim, W. Choi, and S. Lee, "Annoyance caused by amplitude modulation of wind turbine noise," *Noise control engineering journal*, vol. 59, no. 1, 2011. (Cited on page 10.)

[29] H. G. Leventhall, "Low frequency noise and annoyance," *Noise and Health*, vol. 6, 2004. (Cited on page 10.)

[30] D. Siponen, "The assessment of low frequency noise and amplitude modulation of wind turbines wind turbine noise conference," NICE/ Europe, 2011. (Cited on page 10.)

[31] A. N. Salt and T. E. Hullar, "Responses of the ear to low frequency sounds, infrasound and wind turbines," *Hearing research*, vol. 268, 2010. (Cited on page 10.)

[32] K. Bolin, G. Bluhm, G. Eriksson, and M. E. Nilsson, "Infrasound and low frequency noise from wind turbines: exposure and health effects," *Environmental research letters*, vol. 6, 2011. (Cited on page 10.)

[33] T. Evans, J. Cooper, and V. Lenchine, "Infrasound levels near wind farms and in other environments," tech. rep., Environment protection authority and Resonate acoustics, Jan 2013. (Cited on page 10.)

[34] "Wind energy-the facts, wind farms and health," tech. rep., Clean energy council, Jan 2015. (Cited on page 10.)

[35] E. Salomons, *Computational atmospheric acoustics*. Kluwer Academic Publishers, 2001. (Cited on pages 12, 15, 16, 63, 86, 87, 88, 89, 90, 93, 94, 131 and 132.)

[36] S. Oerlemans, M. Fisher, T. Maeder, and K. Kogler, "Reduction of wind turbine noise using optimized airfoils and trailing edge serrations," *AIAA journal*, vol. 47, no. 6, 2009. (Cited on page 13.)

[37] M. Cand and A. Bullmore, eds., *Measurements demonstrating mitigation of far-field AM from wind turbines*, 6th International Meeting on Wind Turbine Noise 2015, 2015. (Cited on page 13.)

[38] M. S. Howe, "A review of the theory of trailing edge noise," *NASA Contractor report 3021l*, 1978. (Cited on page 14.)

[39] J. Casper and F. Farassat, "Broadband trailing edge noise prediction in the time domain," *Journal of Sound and Vibration*, vol. 271, 2004. (Cited on page 14.)

[40] R. Amiet, "Acoustic radiation from an airfoil in a turbulent stream," *Journal of Sound and Vibration*, vol. 41, pp. 407–402, 1975. (Cited on pages 14, 23 and 41.)

[41] R. Amiet, "Noise due to turbulent flow past a trailing edge," *Journal of Sound and Vibration*, vol. 47, pp. 387–393, 1976. (Cited on pages 14, 19, 27, 41 and 60.)

[42] F. Farassat, "Theory of noise generation from moving bodies with an application to helicopter rotors," tech. rep., NASA, 1975. (Cited on page 14.)

[43] F. Farassat, "Linear acoustic formulas for calculation of rotating blade noise," *AIAA*, vol. 19, 1980. (Cited on page 14.)

[44] J. Casper and F. Farassat, "A new time domain formulation for broadband noise predictions," *International Journal of Aeroacoustics*, vol. 1, no. 3, 2002. (Cited on page 14.)

[45] M. Roger and S. Moreau, "Back-scattering correction and further extensions of amiet's trailing-edge noise model. part i: theory," *Journal of Sound and Vibration*, vol. 286, pp. 477–506, 2005. (Cited on pages 14, 20, 22, 23, 26, 27, 127 and 128.)

[46] S. A. L. Glegg, S. M. Baxter, and A. G. Glendinning, "The prediction of broadband noise from wind turbines," *Journal of sound and vibration*, vol. 118, 1987. (Cited on page 14.)

[47] F. Bertagnolio, "Trailing edge noise model applied to wind turbine airfoil," tech. rep., Technical University of Denmark, 2008. (Cited on page 14.)

[48] J. E. F. Williams and L. H. Hall, "Aerodynamic sound generation by turbulent flow in the vicinity of a scattering half plane," *Journal of Fluid Mechanics*, vol. 40, 1970. (Cited on page 15.)

[49] M. R. Fink, "Noise component method for airframe noise," *Journal of aircraft*, vol. 16, 1979. (Cited on page 15.)

[50] O. Marsden, C. Bogey, and C. Bailly, "Direct noise computation of the turbulent flow around a zero-incidence airfoil," *AIAA journal*, vol. 46, no. 4, 2008. (Cited on page 15.)

[51] J. Hardin and D. Pope, "An acoustic/viscous splitting technique for computational aeroacoustics," *Theoretical and computational fluid dynamics*, vol. 6, 1994. (Cited on page 15.)

[52] W. Shen, W. Zhu, and J. N. Sørensen, "Aeroacoustic computations for turbulent airfoil flows," *AIAA journal*, vol. 47, 2009. (Cited on page 15.)

[53] W. Zhu, W. Shen, and J. N. Sørensen, "High-order numerical simulations of flow-induced noise," *International journal for numerical methods in fluids*, vol. 66, 2010. (Cited on page 15.)

[54] J. M. Prospathopoulos and S. G. Voutsinas, "Application of a ray thoery model to the prediction of noise emissions from isolated wind turbines and wind parks," *Wind Energy*, vol. 10, 2006. (Cited on page 16.)

[55] M. West, K. Gilbert, and R. A. Sack, "A tutorial on the parabolic equation (pe) model used for long range sound propagation in the atmosphere," *Applied Acoustics*, vol. 37, 1992. (Cited on page 16.)

[56] B. Cotté and P. Blanc-Benon, "Estimates of the relevant trubulent scales for acoustic propagation in an upward refracting atmosphere," *Acta Acustica united with Acustica*, vol. 93, 2007. (Cited on pages 16 and 125.)

[57] K. Bolin, M. Almgren, E. Ohlsson, and Karasalo, "Long term estimations of low frequency noise levels over water from an off-shore wind farm," *J. Acoust. Soc. Am*, vol. 135, 2014. (Cited on page 16.)

[58] T. V. Renterghem, D. Botteldooren, and L. Dekoninck, "Airborne sound propagation over sea during offshore wind farm piling," *J. Acoust. Soc. Am*, vol. 135, 2014. (Cited on page 16.)

[59] B. Cotté, P. Blanc-Benon, and C. Bogey, "Time-domain impedance boundary conditions for simulations of outdoor sound propagation," *AIAA journal*, vol. 47, no. 10, 2009. (Cited on page 16.)

[60] F. Daude, J. Berland, T. Emmert, P. Lafon, F. Crouzet, and C. Bailly, "A high-order finite-difference algorithm for direct computation of aerodynamic sound," *Computers and Fluids*, vol. 61, 2012. (Cited on pages 16 and 124.)

[61] S. Moreau and M. Roger, "Back-scattering correction and further extensions of amiet's trailing-edge noise model. part ii: Application," *Journal of Sound and Vibration*, vol. 323, pp. 397–425, 2009. (Cited on pages 20, 33 and 60.)

[62] R. H. Schlinker and R. K. Amiet, "Helicopter rotor trailing edge noise," tech. rep., NASA contractor report 3470, 1981. (Cited on pages 26, 54, 58 and 59.)

[63] G. M. Corcos, "Resolution of pressure in turbulence," *Journal of the Acoustical Society of America*, vol. 35, no. 2, pp. 192–199, 1963. (Cited on page 26.)

[64] R. Amiet, "Effect of the incident surface pressure field on noise due to turbulent flow past a trailing edge," *J. Acoust. Soc. Am*, vol. 57, 1978. (Cited on page 27.)

[65] C. Hong and K. K. Shin, "Modeling of wall pressure fluctuations for finite element structural analysis," *Journal of Sound and Vibration*, vol. 329, 2009. (Cited on page 27.)

[66] M. Goody, "Empirical spectral model of surface pressure fluctuations.," *AIAA journal*, vol. 42, no. 9, 2004. (Cited on page 28.)

[67] Y. Rozenberg, G. Robert, and S. Moreau, "Wall-pressure spectral model including the adverse pressure gradient effects," *AIAA Journal*, pp. 2168–2179, 2012. (Cited on pages 28, 29 and 60.)

[68] F. Bertagnolio, A. Fischer, and W. Zhu, "Tuning of turbulent boundary layer anisotropy for improved surface pressure and trailing-edge noise modeling," *Journal of Sound and Vibration*, vol. 333, pp. 991–1010, 2014. (Cited on page 30.)

[69] J. Katz and A. Plotkin, *Low-speed aerodynamics 2nd Edition*. Cambridge university press, 2001. (Cited on page 30.)

[70] F. Bertagnolio, "Boundary layer measurements of the naca0015 and implications for noise modeling," *Riso project*, 2011 Jan. (Cited on page 31.)

[71] T. F. Brooks and T. H. Hodgson, "Trailing edge noise prediction from measured surface pressures," *Journal of Sound and Vibration*, vol. 78, no. 1, 1981. (Cited on pages 35, 41 and 60.)

[72] C. Bailly and G. Comte-Bellot, *Turbulence*. CNRS editions, 2003. (Cited on page 45.)

[73] Y. Rozengerg, *Modelisation analytique du bruit aerodynamique a large bande des machines tournantes: utilisation de calculs moyennes de mecanique des fluides*, 2007. (Cited on pages 45 and 129.)

[74] J. Christophe, *Application of hybrid methods to high frequency aeroacoustics*, 2011. (Cited on pages 45 and 129.)

[75] M. Roger and S. Moreau, "Extensions and limitations of analytical airfoil broadband noise models," *International Journal of Acoustics*, vol. 9, no. 3, pp. 273–305, 2010. (Cited on page 46.)

[76] S. Glegg and W. Devenport, "Panel methods for airfoils in turbulent flow," *Journal of Sound and Vibration*, vol. 329, 2010. (Cited on page 48.)

[77] M. Hansen, *Aerodynamics of wind turbine — 2nd edition*. Earthscan, 2008. (Cited on pages 52, 53 and 54.)

[78] G. Ingram, "Wind turbine blade analysis using the blade element momentum method," October 2011. (Cited on page 52.)

[79] F. Bertagnolio, J. N. Sørensen, and J. Johansen, *Wind turbine airfoil catalogue*, 2001. (Cited on page 56.)

[80] A. Creech, W.-G. Früh, and A. Maguire, "Simulations of an offshore wind farm using large eddy simulation and a torque-controlled actuator disc model," *Surveys in Geophysics*, 2015. (Cited on page 56.)

[81] M. V. Lowson, "The sound field for singularities in motion," *Proceedings of the Royal Society of London. Series A, Mathematical and Physical Sciences*, vol. 286, 1965. (Cited on page 58.)

[82] S. Sinayoko, M. Kingan, and A. Agarwal, "Trailing edge noise theory for rotating blades in uniform flow," *Proc. Roy. Soc. A*, vol. 469, 2013. (Cited on page 59.)

[83] A. Fischer, *Experimental characterization of airfoil boundary layer for improvement of aeroacoustic and aerodynamic modeling*. PhD thesis, Technical University of Denmark, 2011. (Cited on page 60.)

[84] F. Bertagnolio, "Low noise airfoil—final report," *EUDP project*, 2012. (Cited on page 60.)

[85] D. Wilson, "The sound-speed gradient and refraction in the near-ground atmosphere," *J. Acoust. Soc. Am.*, vol. 113, 2003. (Cited on pages 62 and 63.)

[86] T. Foken, "50 years of the monin-obukhov similarity theory," *Boundary-Layer Meteorology*, vol. 119, 2006. (Cited on pages 62 and 63.)

[87] S. Cheinet, "A numerical approach to sound levels in near-surface refractive shadows," *J. Acoust. Soc. Am.*, vol. 131, no. 3, 2012. (Cited on pages 62, 63, 131, 132 and 133.)

[88] V. Ostashev and D. Wilson, "Relative contributions from temperature and wind velocity fluctuations to the statistical moments of a sound field in a turbulent atmosphere," *Acta Acustica united with Acustica*, vol. 86, 2000. (Cited on pages 63 and 132.)

[89] S. Oerlemans, "An explanation for enhanced amplitude modulation of wind turbine noise," in *Wind Turbine Amplitude Modulation: Research to Improve Understanding as to its Cause and Effect*, RenewableUK, 2013. (Cited on pages 70 and 83.)

[90] M. Smith, "Fundamental research into possible causes of amplitude modulation," in *Wind Turbine Amplitude Modulation: Research to Improve Understanding as to its Cause and Effect*, RenewableUK, 2013. (Cited on page 70.)

[91] M. Lowson, *Assessment and prediction of wind turbine noise.* Harwell Laboratory, Energy Technology Support Unit, 1993. (Cited on page 80.)

[92] C. I. Chessell, "Propagation of noise along a finite impedance boundary," *J. Acoust. Soc. Am.*, vol. 62, 1977. (Cited on pages 86 and 87.)

[93] M. E. Delany and E. N. Bazley, "Acoustical properties of fibrous absorbent materials," *Applied Acoustics*, vol. 3, 1970. (Cited on page 87.)

[94] K. Attenborough, "Acoustical impedance models for outdoor round surfaces," *Journal of Sound and Vibration*, vol. 99, 1985. (Cited on page 87.)

[95] J. F. Allard, *Propagation of sound in porous media.* Elsevier Applied Science, 1993. (Cited on page 87.)

[96] M. Baudoin and F. Coulouvrat, "Sound, infrasound, and sonic boom absorption by atmospheric clouds," *J. Acoust. Soc. Am*, vol. 130, 2011. (Cited on page 89.)

[97] M. West, K. Gilbert, and R. A. Sack, "A tutorial on the parabolic equation (pe) model used for long range sound propagation in the atmosphere," *Applied Acoustics*, vol. 37, 1992. (Cited on pages 89 and 90.)

[98] D. Dragna, *Modelisation par une approche temporelle de la propagation acousique en milieu exterieur: traitement de frontieres complexes et validation sur site ferroviaire.* PhD thesis, Ecole centrale de Lyon, 2011. (Cited on pages 90, 91, 92 and 93.)

[99] K. E. Gilbert and M. J. White, "Application of the parabolic equation to sound propagation in a refracting atmosphere," *The Journal of the Acoustic Society of America*, vol. 85, no. 2, 1988. (Cited on pages 91, 92, 93 and 94.)

[100] M. D. Collins, "A split-step pade solution for the parabolic equation method," *J. Acoust. Soc. Am*, vol. 93, 1993. (Cited on page 92.)

[101] F. D. Tappert, "The parabolic approximation method," in *Wave propagation and underwater acoustics* (J. B. Keller and J. S. Papadakis, eds.), Springer Berlin Heidelberg, 1977. (Cited on page 94.)

[102] M. D. Collins and E. K. Westwood, "A higher-order energy-conserving parabolic equation for range-dependent ocean depth, sound speed, and density," *J. Acoust. Soc. Am.*, vol. 89, 1991. (Cited on page 94.)

[103] B. Cotté, Y. Tian, and A. Chaigne, eds., *Effets météorologiques sur le bruit rayonné par les éoliennes*, Congrès Francais d'Acoustique, 2014. (Cited on page 110.)

[104] B. Cotté and Y. Tian, eds., *Prediction of variability in wind turbine noise calculations*, Wind turbine noise, 2015. (Cited on page 125.)

[105] Wikipedia, "Monin - obukhov similarity theory — wikipedia, the free encyclopedia," 2015. [Online; accessed 28-September-2015]. (Cited on page 131.)

[106] B. Gauvreau, D. Ecotiére, H. Lefevre, and B. Bonhomme, "Propagation acoustique en milieu exterieur complexe - caractérisation expérimentale in-situ des conditions micrométéorologiques," tech. rep., Rapport ERLPC, 2009. (Cited on pages 131 and 132.)

[107] D. K. Wilson, "An alternative function for the wind and temperature gradients in unstable surface layers," *Bounayer-layer Meteorol*, vol. 99, 2001. (Cited on page 132.)

[108] D. K. Wilson, "A turbulence spectral model for sound propagation in the atmoshpere that incorporates shear and buoyancy forcings," *J. Acoust. Soc. Am*, vol. 108, 2000. (Cited on page 133.)

[109] D. K. Wilson, "Performance bounds for acoustic direction-of-arrival arrays operating in atmosphere turbulence," *J. Acoust. Soc. Am*, vol. 103, 1998. (Cited on page 134.)

[110] S. Mittal and P. Saxena, "Hysteresis in flow past a naca 0012 airfoil," *Comput. Methods Appl. Mech. Eng*, vol. 191, 2002. (Cited on page 137.)

Titre : Modélisation des sources et de la propagation dans l'atmosphère du bruit des éoliennes

Mots clés : bruit de bord de fuite, bruit d'impact de turbulence, théorie d'Amiet, équation parabolique

Résumé : L'objectif de ce travail est de modéliser les sources et la propagation atmosphérique du bruit généré par les éoliennes afin de mieux comprendre les caractéristiques de ce bruit à grande distance et d'aider les fabricants d'éoliennes et les développeurs de parc à respecter la réglementation. En couplant des modèles physiques de source aéroacoustique et de propagation, nous sommes capables de prédire les spectres de bruit, ainsi que la directivité et les modulations d'amplitude associées, pour différentes conditions atmosphériques. Le modèle analytique d'Amiet est choisi pour prédire le bruit d'impact de turbulence et le bruit de bord de fuite, en considérant plusieurs améliorations par rapport à la théorie initiale. Ces modèles sont validés par comparaison avec des mesures de la littérature en soufflerie avec des profils fixes.

Le modèle d'Amiet est ensuite appliqué à une éolienne complète pour prédire le bruit émis en champ proche. L'effet de la rotation des pales et l'effet Doppler sont pris en compte. On utilise d'abord des profils de vent constant sans turbulence, puis l'effet du cisaillement du vent et de la turbulence atmosphérique sont inclus à l'aide de la théorie de la similitude de Monin-Obukhov. De bons accords sont obtenus avec des mesures sur site éolien lorsque l'on considère à la fois les bruits de bord de fuite et d'impact de turbulence. On propose finalement une méthode pour coupler le modèle de source à un code d'équation parabolique afin de prendre en compte les effets de sol et de réfraction atmosphérique. En fonction de la direction de propagation, les niveaux de bruit varient car l'effet de sol est influencé par les gradients de vent et car une zone d'ombre est présente dans la direction opposée au vent.

Title : Modeling of wind turbine noise sources and propagation in the

Keywords : trailing edge noise, turbulent inflow noise, Amiet theory, parabolic equation

Abstract : The purpose of this work is to model wind turbine noise sources and propagation in the atmosphere in order to better understand the characteristics of wind turbine noise at long range and to help wind turbine manufacturers and wind farm developers meet the noise regulations. By coupling physically-based aeroacoustic source and propagation models, we are able to predict wind turbine noise spectra, directivity and amplitude modulation in various atmospheric conditions. Amiet's analytical model is chosen to predict turbulent inflow noise and trailing edge noise, considering several improvements to the original theory. The two models are validated against several wind tunnel experiments from the literature using fixed airfoils.

Amiet's model is then applied on a full-size wind turbine to predict the noise emission level in the near field. Doppler effect and blade rotation are taken into account. Cases with constant wind profiles and no turbulence are used first, then wind shear and atmospheric turbulence effects obtained from Monin-Obukhov similarity theory are included. Good agreements against field measurements are found when both turbulent inflow noise and trailing edge noise are considered. We finally propose a method to couple the source model to a parabolic equation code to take into account ground and atmospheric refraction effects. Depending on the propagation direction, noise levels vary because the ground effect is influenced by wind shear and a shadow zone is present upwind.